Czech Technical University in Prague
Faculty of Electrical Engineering
Department of Telecommunication Engineering

PHOTONIC CRYSTAL FIBERS: OPTIMIZATION FOR TELECOMMUNICATION PURPOSES

by

RICHARD ZELENÝ

A thesis submitted to
the Faculty of Electrical Engineering, Czech Technical University in Prague,
in partial fulfillment of the requirements for the degree of Doctor.

Prague, December 2015

PhD programme: Electrical Engineering and Information Technology
Branch of study: Telecommunication Engineering

Thesis Supervisor: Dr. Michal Lucki

Thesis Supervisor:
Dr. Michal Lucki
Department of Telecommunication Engineering
Faculty of Electrical Engineering
Czech Technical University in Prague
Technická 2
166 27 Prague 6
Czech Republic

Copyright © 2015 RICHARD ZELENÝ

Abstract

Photonic crystal fibers are optical waveguides based on a periodic air-glass structure offering higher design flexibility compared to that of standard single-mode fibers. On one hand, such fibers allow for extremely tight mode confinement related to increased nonlinearity and better chromatic dispersion controllability. On the other hand, photonic crystal fibers enable light guiding in very large cores keeping the single-mode regime of operation and low loss.

This doctoral thesis deals with scientific problems related to control of light propagation within photonic crystal fibers and it contributes mainly to the areas of optics, photonics, telecommunication and sensing. The objective is to describe main design principles, find their limitations and consequently optimize fiber geometries. Until now, these limitations have not been investigated thoroughly and therefore became the central point for the doctoral thesis.

The goal is not to present fiber structures with novel geometries, but to investigate new limits in designing photonic crystal fibers. One of the presented designs is a photonic crystal fiber with a dispersion parameter as close as possible to zero value. Further effort is applied on a hexagonal fiber structure that is optimized to operate as a dispersion compensator of standard single-mode fibers. The author predicts that the negative dispersion parameter cannot be higher in this structure operating over a bandwidth larger than that considered in this thesis.

Another important part of the thesis aims to control of confinement loss, which is used to design a narrowband fiber filter as well as an effectively single-mode photonic crystal fiber with large effective mode area and chalcogenide background.

Fiber designs were carried out by varying key geometrical parameters such as hole-to-hole spacing, airhole diameters in selected rings and number of rings around the fiber core. The influence of each structural parameter on modal properties is examined and described in detail. Understanding the mechanism governing chromatic dispersion as well as confinement loss is necessary not only for the fiber design, but also to predict the potential manufacturing tolerances.

Last but not least, supercontinuum generation is investigated in the designed chalcogenide fiber using the split-step Fourier method. The modal properties are calculated by the full-vectorial finite difference frequency domain method. The simulation models of presented fibers are verified by convergence testing.

Keywords:

Chromatic dispersion, Confinement loss, Large mode area, Fiber design, Photonic crystal fiber, Supercontinuum generation.

Abstrakt

Fotonická vlákna založená na periodickém uspořádání mikrostruktur v okolí jádra nabízí nové optické vlastnosti v porovnání s klasickými jednovidovými vlákny. Jednou z těchto vlastností je možnost extrémně silného uvěznění vidu v malém jádře, což má za následek zvýšenou nelinearitu a nové možnosti ladění parametru chromatické disperze. Na druhou stranu je také možné pomocí fotonických vláken udržet nízké ztráty při jednovidovém šíření optického pulsu velkými jádry.

Tato práce řeší vědecké problémy týkající se šíření světla fotonickými vlákny a přispívá zejména do oblastí optiky, fotoniky, telekomunikací a senzorů. Dizertační práce popisuje základní principy návrhů fotonických vláken, hledá jejich limity a na tomto základě optimalizuje geometrie vláken. Tyty limity nebyly doposud zkoumány do hloubky a tedy jsou hlavním bodem této práce.

Cílem této práce tedy není ukázat nové vláknové struktury, ale zkoumat limity již existujících struktur. Jedním z prezentovaných návrhů je mikrostrukturní vlákno s disperzním parametrem blížícím se nule, jak jen to je možné. Další návrh se zabývá hexagonálním uspořádáním mikrostruktur v plášti vlákna. Geometrické parametry těchto mikrostruktur jsou optimalizovány pro kompenzaci chromatické disperze standardních jednovidových vláken. Autor práce předpokládá, že disperzní parametr kompenzačního vlákna nemůže být nižší při zachování šířky pásma.

Dalším cílem této práce je zkoumání vlivu geometrických parametrů vlákna na útlumové charakteristiky. Takto získané poznatky jsou využity pro návrh uzkopásmového vláknového filtru. Dále pak pro návrh jednovidového chalkogenidového vlákna s velkou vidovou plochou.

Vlákna jsou navržena laděním klíčových geometrických parametrů, jako je rozteč mikrostruktur, průměry mikrostruktur ve vybraných prstencích a počet prstenců obklopující jádro vlákna. Vliv každého z parametrů je vyhodnocen a následně detailně popsán. Pochopení těchto mechanismů je nezbytné nejen pro návrh vlákna, ale také pro odhad výrobní tolerance.

V neposlední řadě jsou vlastnosti chalkogenidového vlákna s velkou vidovou plochou použity jako vstup pro zkoumání generace superkontinua pomocí split-step Fourierovi metody. Vidové vlastnosti vláken jsou získány pomocí plně vektorové metody konečných diferencí ve frekvenční doméně. U všech simulací vláken je správné nastavení simulace ověřeno konvergenčním testem.

Klíčová slova:

Chromatická disperze, Útlum vláken, Velká vidová plocha, Návrh vláken, Mikrostrukturní optická vlákna, Generace superkontinua.

Acknowledgements

First of all, I would like to express my gratitude to my dissertation thesis supervisor, Dr. Michał Łucki. He has been a constant source of encouragement and insight during my research and helped me with numerous problems and professional advancements.

My sincere thanks go to the staff of the Department of Telecommunication Engineering that maintained flexible environment for my research. Special thanks to the department management for providing most of the funding for my research.

Finally, my greatest thanks go to my family, for their infinite patience and care.

Contents

List of Figures **xi**

List of Tables **xiii**

Abbreviations **xvii**

1 Introduction **1**
1.1 Motivation 1
1.2 Problem Statement 2
1.3 Aims and Contributions of the Thesis 2
1.4 Structure of the Thesis 3

2 State of the Art **5**
2.1 Basic Properties 5
2.2 Related Works 6
2.2.1 Doping the Fiber Core 7
2.2.2 Airholes Close to the Fiber Center 7
2.2.3 Dual Concentric Cores 8
2.2.4 Suspended Core Fibers and Exposed Core Fibers 9
2.2.5 Leakage Channel Fibers 10
2.2.6 Supercontinuum Generation 11

3 Methods and Design Principles **15**
3.1 Methods 15
3.1.1 Finite Difference Frequency Domain Method 15
3.1.1.1 Chromatic Dispersion in a PCF 16
3.1.1.2 Loss and Effective Mode Area in a PCF 18
3.2 Convergence Testing 20
3.3 Design Principles 22
3.3.1 Near Zero and Dispersion Compensating Designs 22
3.3.2 Large Mode Area Designs 23
3.4 Basic Mechanisms of Supercontinuum Generation 24
3.4.1 Pulse Propagation Model 24

3.4.2 Supercontinuum Generation in the Subpicosecond Regime 25

4 Results **27**
4.1 Near Zero Dispersion Fiber 27
4.1.1 Summary 31
4.2 Large Negative Dispersion Fiber 32
4.2.1 Summary 38
4.3 Narrowband Optical Fiber Filter 39
4.3.1 Summary 44
4.4 Large Mode Area Fiber 44
4.4.1 Supercontinuum Generation 49
4.4.2 Summary 56

5 Conclusion **57**

Bibliography **59**

Publications of the Author **71**

A Materials **73**
A.1 Refractive Indices and Material Dispersions 73
A.1.1 Silica Materials 73
A.1.2 Heavy Fluoride Materials 77
A.1.3 Tellurite and Chalcogenide Materials 79

B Simulation Setup and Convergence testing **81**
B.1 Near Zero Dispersion Fiber - Convergence Test 82
B.2 Large Negative Dispersion Fiber - Convergence Test 83
B.3 Narrowband Optical Fiber Filter - Convergence Test 85
B.4 Large Mode Area Fiber - Convergence Test 86

List of Figures

3.1 Flow diagram of the fiber design process 21

4.1 Cross-section and normalized fundamental mode field distribution at 1550 nm. 28
4.2 Nearly zero dispersion with deviations in diameter of airholes in the first (a) and the second ring (b) starting from the fiber center. 29
4.3 Nearly zero dispersion with deviations in diameter of airholes in the third innermost ring (a) and low-index doped regions (b). 30
4.4 Nearly zero ultra-flattened dispersion with different dopants in the fiber cross-section 31
4.5 Designed fiber structure with the fundamental mode distribution for 1550 nm. 33
4.6 Dispersion parameter as a function of wavelength (a) and dispersion slope as a function of wavelength (b) for varied airhole diameter d_1 and $d_{2,3}$. . . . 33
4.7 Relative dispersion slope of NDSF and designed DC-PCF (a) and residual dispersion after the dispersion compensation of NDSF by 1 km long DC-PCF (b). 34
4.8 Modified fiber structure with the fundamental mode distribution for 1550 nm. 36
4.9 Dispersion parameter as a function of wavelength (a) and dispersion slope as a function of wavelength (b) for varied airhole diameter d_1 and $d_{2,3}$. . . . 36
4.10 Relative dispersion slope of NDSF and designed DC-PCF (a) and residual dispersion after the dispersion compensation of NDSF by 1 km long modified DC-PCF (b). 38
4.11 Proposed fiber structure with the normalized mode field distribution at the wavelength of 1 μm (a) and 1.55 μm (b) with strong coupling. 40
4.12 Effective refractive index (dash-dot line) and confinement loss (solid line) wavelength dependence of the designed fiber with stop-band near the wavelength of 1.55 μm. The fiber doped by GeO_2 is considered. 41
4.13 Effective refractive index (dash-dot line) and confinement loss (solid line) wavelength dependence of the designed fiber with stop-band near the wavelength of 1.4 μm. The nondoped fiber is considered. 42

4.14 Confinement loss wavelength dependance, where GeO_2 core size d_r (a) and diameter of the innermost airholes d_1 (b) is an investigated parameter. . . 43
4.15 Confinement loss wavelength dependance, diameter d_2 (a) and diameter d_3 (b) is an investigated parameter. 43
4.16 Fundamental mode field distribution inside the designed fiber with bending radius $r_b = \infty$ (a) and 20 cm (b). The fundamental (c), the second- (d) and the third- (e) order mode field distribution in the straight fiber. 45
4.17 Dispersion parameter of the chromatic and material dispersion (a). Confinement loss as a function of the wavelength for the fundamental, the second- and the third-order mode, respectively (b). In (b), the number of the outer rings with diameter d is considered as a parameter. The solid line is for the 2 outer rings, the dash-dot line for the 1 outer ring and the dashed line for the structure having the only one ring with diameter d_1. 46
4.18 Confinement loss as a function of the wavelength for the fundamental, the second and the third-order mode, respectively. In (a), d_1 is considered as a parameter. The solid line represents the designed fiber with d_1, the dash-dot line is for $d_1 - 10$ % and the dashed line for $d_1 + 10$ %. In (b), d is considered as a parameter. The solid line represents the designed fiber with d, the dash-dot line is for $d - 10$ % and the dashed line for $d + 10$ %. . . . 47
4.19 Confinement loss as a function of bending radius r_b for the fundamental, the second- and the third-order mode, respectively at the wavelengths of 1.5 μm (a), 2 μm (b), 4 μm (c) and 9.5 μm (d). 48
4.20 Supercontinuum generation inside the LMA fiber pumped at 3.5 μm. It should be noticed that 40 dB scale is applied to all density plots. 50
4.21 Supercontinuum generation inside the LMA fiber pumped at 4.5 μm. . . . 51
4.22 Supercontinuum generation inside the LMA fiber pumped at 4.9 μm. . . . 52
4.23 Supercontinuum generation inside the LMA fiber pumped at 6.5 μm. . . . 52
4.24 Supercontinuum generation inside the LMA fiber, the pulse duration of the pump pulse is decreased to 50 fs. 54
4.25 Supercontinuum generation inside the LMA fiber, the pulse duration of the pump pulse is increased to 200 fs. 54
4.26 Supercontinuum generation inside the LMA fiber, the peak power of the pump pulse is reduced to 25 kW. 55
4.27 Supercontinuum generation inside the LMA fiber, the peak power of the pump pulse is raised to 100 kW. 55

A.1 Refractive index wavelength dependence of selected silica materials doped by GeO_2 and P_2O_5. 74
A.2 Material dispersion upon wavelength for selected silica materials doped by GeO_2 and P_2O_5. 74
A.3 Refractive index wavelength dependence of selected silica materials doped by B_2O_3 and F. 75

A.4 Material dispersion upon wavelength for selected silica materials doped by B_2O_3 and F. 75
A.5 Refractive index wavelength dependence of selected fluoride materials. . . . 77
A.6 Material dispersion upon wavelength for selected fluoride materials. 78
A.7 Refractive index wavelength dependence of selected tellurite and chalcogenide materials. 80
A.8 Material dispersion upon wavelength for selected tellurite and chalcogenide materials. 80

B.1 Convergence testing the number of the mesh cells on x axis (a) and the number of the PML layers (b). The near zero dispersion fiber is considered. 82
B.2 Convergence testing the number of the mesh cells on x axis (a) and the number of the PML layers (b). The large negative dispersion DC-PCF is considered. 83
B.3 Convergence testing the number of the mesh cells on x axis (a) and the number of the PML layers (b). The modified large negative dispersion DC-PCF is considered. 84
B.4 Convergence testing the number of the mesh cells on x axis (a) and the number of the PML layers (b). The narrowband optical fiber filter is considered. 85
B.5 Convergence testing the number of the mesh cells on x axis (a) and the number of the PML layers (b). The large mode area fiber is considered. . . 86

List of Tables

A.1 Sellmeier coefficients of selected silica materials doped by GeO_2 and P_2O_5. 76
A.2 Sellmeier coefficients of selected silica materials doped by B_2O_3 and F. . . 76
A.3 Sellmeier coefficients of selected fluorides materials. 77
A.4 Sellmeier coefficients of selected tellurite and chalcogenide materials. 79

Abbreviations

Mathematical Terminology

A	Electric field envelope
A_{eff}	Effective mode area
B	Birefringence
B_j, C_j	Sellmeier coefficients
c	Light velocity
d	Diameter of the outer airholes
d_1	Diameter of the innermost airholes
d_2	Diameter of the airholes in the second ring starting from the fiber center
d_3	Diameter of the airholes in the third ring starting from the fiber center
d_d	Diameter of the low-index doped regions
d_r	Diameter of the doped core by GeO_2
D	Chromatic dispersion parameter
D_{DCF}	Chromatic dispersion parameter of a DCF
D_m	Material dispersion parameter
D_{NDSF}	Chromatic dispersion parameter of a NDSF
D_r	Residual dispersion parameter
D_w	Waveguide dispersion parameter
E_t	Transverse electric field vector
f_r	Fractional contribution of the Raman response
h_r	Delayed Raman contribution
i	Simulation step
I_n	Normalized intensity
k	Order of Taylor expansion
l_D	Dispersion length
l_{fiss}	Soliton fission length
l_N	Nonlinear length
L	Confinement loss
L_s	Splice loss
m	Soliton order
M_{PML}	Number of perfectly match layers
M_x	Number of mesh cells in x direction

n	Linear refractive index
n_2	Nonlinear refractive index
n_{eff}	Effective refractive index
$n_{eff,x}$	Effective refractive index of x polarized mode
$n_{eff,y}$	Effective refractive index of y polarized mode
n_{eq}	Refractive index of an equivalent straight fiber
N	Number of simulation steps
NA	Numerical aperture
P_0	Peak power
r	Core radius
R	Nonlinear Raman response function
r_b	Bending radius
r_{eff}	Effective bending radius
s	Order in which solitons are ejected
S	Dispersion slope
S_{DCF}	Dispersion slope of a DCF
S_{NDSF}	Dispersion slope of a NDSF
t	Time
T	Retarded time
T_0	Pulse Duration
v_f	Phase velocity
v_g	Group velocity
w	Spot size
w_{PCF}	Spot size of a PCF
w_{SMF}	Spot size of a SMF
x, y	Coordinates
z	Distance
z_{sol}	Soliton period
β	Phase constant
β_k	Phase constant coefficient of Taylor expansion
λ	Wavelength
λ_0	Carrier or pump wavelength
Λ	Hole-to-hole spacing
γ	Nonlinear coefficient
Γ	Confinement factor
θ	Divergence angle
σ_i	Result of a simulation at step i
σ_N	Result of a simulation at step N
τ_1	Photon oscillation period
τ_2	Damping time of the vibrating atoms
τ_g	Group delay
ω	Angular frequency
ω_0	Carrier angular frequency

Miscellaneous Abbreviations

Appx	Appendix
Chap	Chapter
DC-PCF	Dispersion Compensating Photonic Crystal Fiber
DCF	Dispersion Compensating Fiber
ECF	Exposed Core Fiber
Eq	Equation
FD-TSC	Fluorine-Doped Three-fold Symmetry Core
FDFD	Finite Difference Frequency Domain
Fig	Figure
FM	Fundamental Mode
FEM	Finite Element Method
FWM	Four Wave Mixing
HM	Higher-Order Mode
IG-PCF	Index-Guiding Photonic Crystal Fiber
LCF	Leakage Channel Fiber
LMA	Large Mode Area
M-TIR	Modified Total Internal Reflection
NDSF	Non-Dispersion Shifted Fiber
PBG	Photonic Bang Gap
PCF	Photonic Crystal Fiber
PML	Perfectly Match Layer
RDS	Relative Dispersion Slope
Ref	Reference
SC	Supercontinuum
SCF	Suspended Core Fiber
Sec	Section
SMA	Small Mode Area
SMF	Single-Mode Fiber
SM	Second-Order Mode
SPM	Self Phase Modulation
Tab	Table
TM	Third-Order Mode
TSC	Three-fold Symmetry Core
ZDW	Zero Dispersion Wavelength

Chapter 1

Introduction

1.1 Motivation

This doctoral thesis summarizes the author's research work undertaken during the time from 2011 to 2015 as part of Grant Agency of the Czech Republic project: GP102/09/P143, and Czech Technical University internal grant projects: SGS10/275/OHK3/3T/13 and SGS13/201/OHK3/3T/13. The projects were aimed at investigating new photonic transmission media for optical networks. Regarding the projects, the author's efforts were to deepen and increase knowledge in the field of fiber optic, to design novel fiber structures, and to find design limitations of current structures not only for telecommunication, but also for high-power laser delivery, supercontinuum generation and compression of optical pulses.

Conventional optical fibers with a core surrounded by lower refractive index dielectric cladding usually operate well in telecommunication, medicine, optical sensing, and interferometry among others. However, they pose significant limitation related to their structure and used materials: minimum attenuation, modal cut-off wavelength, usable bandwidth, polarization and dispersion properties. Future optical systems can have challenges rarely satisfied by using conventional single-mode fibers (SMFs). The demands that will be met on that fibers can be of a nature that lead to difficult implementation, because of their limited number of design freedom.

Photonic crystal fibers (PCFs) also known as holey fibers or microstructured optical fibers are more flexible, due to a better manipulability of their geometry and therefore offer more design tools. A special interest of the thesis is focused on the unique properties of PCFs with small effective mode areas (SMAs) that in general allow designing suitable dispersion and loss properties. On the other hand, large mode area (LMA) fibers for the high-power laser delivery are designed to be effectively single-mode, and, concurrently to be reasonably bendable. Broad supercontinuum (SC) can be generated not only in small, but also in large mode area fibers by enhancing the fiber nonlinearity using the novel highly nonlinear glasses as a fiber background that is investigated in this doctoral thesis.

1.2 Problem Statement

Chromatic dispersion of standard SMFs is one of the major issues in optical networks, it limits transmission of information, which puts dispersion requirements on a transmission medium. In an optical domain of a communication network, there are efforts to design an optical fiber with an opposite dispersion that can be connected to the path in order to nullify accumulated dispersion and finally prevent the transmitted signal temporally. On the other hand, recent studies aim to achieve broadening of optical pulses through a fiber with dispersion close to zero.

Nowadays, development in the field of photonic crystal fibers changes the area of interest from telecommunication to the high-power delivery, sensing, and optical signal processing. One of the challenges is to develop transmission medium with effective mode area as large as possible, keeping the single-mode regime of operation and low bending loss.

Highly desired are fibers that pose concurrently as a sensor as well as a transmission medium. Such a distributed sensor can measure especially stress, strain, temperature, electromagnetic field, and refractive index. The demands that are placed on fiber sensors shifts the investigated area from near to middle and far infrared having the requirements on development of novel glasses and laser light sources that can operate in these spectral regions.

In the field of PCFs, there are still many unsolved and actual milestones that can be labeled as a "hot topic".

1.3 Aims and Contributions of the Thesis

This doctoral thesis deals with scientific problems related to control of light propagation within a photonic crystal fiber and it contributes mainly to the areas of optics, photonics, telecommunication and sensing. The aim of the doctoral thesis is three-fold.

Firstly, it is aimed at acquiring knowledge of basic light control and design principles to provide distinctions among main design methods. Secondly, the design methods are investigated to find their limitations as well as the best possible fiber geometry for a particular purpose. Until now, these limitations have not been investigated thoroughly and therefore became the central point for the doctoral thesis. Thirdly, in the simulation model, highly nonlinear glasses are used as the fiber background to calculate and investigate supercontinuum generation in the designed media.

The principal contributions of the thesis are as follows:

1. **Novel photonic crystal fibers are designed** based on the principles and methods discussed in the state of the art.

2. **Design limitations of photonic structures are investigated** to find optimal geometries.

3. **Optimization steps are described in details** giving the reference baseline for a reader and a potential designer.

4. **The simulation model is verified** by convergence testing to provide results sufficiently correct while keeping the time effective calculations.

5. **The fabrication tolerances of designed fibers are estimated** by dispersion- or loss-based sensitivity analysis.

1.4 Structure of the Thesis

Firstly, the core research problem is stated and then the fibers are designed based on the methods discussed. The research itself is described in chapters 2 to 4. Some parts of the doctoral thesis are based on two author's impact factor papers and conference articles. These parts are properly cited.

Basic mathematics in the thesis body is presented. The rest of the used mathematical apparatus can be found in the references.

The thesis is organized into five chapters as follows:

1. *Introduction*: describes the motivation and author's efforts together with the goals. Description of contribution of the doctoral thesis is included.

2. *State of the Art*: introduces the reader to the brief theoretical background and surveys a current state of the art and related works.

3. *Method*: presents the used numerical methods, by which the key modal properties of the investigated transverse fiber structures are solved. The steps to verify the correct setting of a simulation model are outlined. Basic design principles are described in details in this chapter.

4. *Results*: the main results are presented and discussed in this chapter. The chapter is dived into the sections, where selected fibers are designed employing the described principles. In first two sections, the fiber designs based on tuning the dispersion characteristics are proposed and the other two sections aim to the designs with optimized loss characteristics.

5. *Conclusion*: an overall summary of the thesis and suggestions of possible topics for further investigation concludes the thesis.

6. *Appendices*: in Appx. A, the material refractive indices are specified. In Appx. B, the convergence tests are presented.

Chapter 2

State of the Art

2.1 Basic Properties

Photonic crystal fibers typically consist of an array of micro-sized airholes embedded within a pure silica background. Optical pulses are propagated through a PCF by the defect in the array caused either by missing airhole in the central region in the case of modified total internal reflection (M-TIR) [1] or by increasing diameter of the central airhole in the case of a photonic band gap (PBG) [1, 2]. This doctoral thesis aims to control of modal properties in an index-guiding PCF (IG-PCF) that rely on the M-TIR.

IG-PCFs are easier to fabricate than PBG fibers, because of the guidance mechanism that does not require a near perfect periodicity of the fiber geometry. [3] The IG-PCFs are also more suitable for chromatic dispersion tailoring for their variability in the solid core having a significant effect on material dispersion. It should be noticed that PBG fibers can guide light through a solid core, but having the core refractive index lower than that of cladding oppositely to the the M-TIR. [4] However, to ensure the PBG guidance, the core is usually much larger compared to IG-PCF, which limits the dispersion controllability.

An IG-PCF is characterized by airhole diameter d, hole-to-hole spacing Λ, the airhole geometry, the number of airholes typically represented as the number of rings around the fiber core and last but not least by used background material.

In general, the solid core can be doped by an appropriate material typically by germanium dioxide to increase refractive index or by fluorine for refractive index decreasing. Further, using advanced chemical compounds as the background material can be more advantageous than using silica especially at the wavelengths longer than 2 μm. [A.1].

Middle-infrared ($\sim$ 2–8 μm) light beam delivery in conventional silica fibers is practically impossible due to the vibration frequency of the atomic bonds, of which significant interaction with electromagnetic waves beyond the wavelength about 1.8 μm makes the glass nontransparent.

Heavy metal fluoride glasses were firstly discovered in 1974 [5] and some of them are transparent up to 9.5 μm [6]. Moreover, their theoretical losses were predicted to be of 10^{-2} dB·km^{-1} at 2.5 μm [7]. So far, it still seems to be a challenge in practice; nowa-

days, their attenuation is higher than attenuation of silica fibers. Although, ZBLAN glass (53 $ZrF_4 - 20\ BaF_2 - 4\ LaF_3 - 3\ AlF_3 - 20\ NaF$) is transparent only up to 6.9 μm [8], it is the most favored glass for its stable composition suitable for fiber drawing. It is also an excellent host for doping by rare earth ions that is broadly applied in fiber lasers and amplifiers [9]. Complete investigation of the heavy metal fluoride glass can be found in Ref. 10.

The soft glasses transparent up to 5 μm [3] with the melting point less than 1000 °C offer new possibilities of the dispersion control in PCFs. Many types of the soft glasses can be combined both in the core and the cladding, due to the similar value of the melting point and viscosity. However, today's fabrication technologies of the soft glasses fibers are not at the same stage as for the silica fibers. Therefore, the soft glasses fibers exhibit losses about a few $dB{\cdot}m^{-1}$ [3]. Although, the fiber length should not exceed a few meters to keep low loss, combination of good dispersion controllabitily and the higher nonlinearity compared to that of silica promises soft glasses fibers to be suitable for supercontinuum generation [11]. [A.1]

Chalcogenide and tellurite glasses are sufficiently transparent over the middle-infrared spectral window [12, 13], chemically stable [14], and their fiber drawing technology is well matured [15]. Chalcogenide glasses are usually based on one or more chalcogen elements of the periodic table group 16: sulfur, selenium, tellurium with the combination of other elements such as arsenic, germanium, antimony, gallium [13, 16]. Contrary, tellurite glasses contain TeO_2 as the main component. Both glasses pose high nonlinear refractive index and as well they suffer high material loss. Nevertheless, they are suitable to generate near-, middle- and far-infrared supercontinuum in a short nonlinear fiber segment [A.4]

2.2 Related Works

Over the years, one of the most investigated fiber designs is a PCF that can be either a chromatic dispersion compensator or an optical transmission medium with nearly zero dispersion.

Manufacturing technologies, as well as simulation tools, allow achieving an exact zero dispersion even at a broad spectrum of wavelengths. However, zero dispersion is undesirable in terms of nonlinear effects, as in four wave mixing (FWM) that can occur, since zero dispersion results in phase-matching of signals [17]. For that reason, research rather focuses on flat and nearly zero dispersion evolution, where dispersion value does not result in significant pulse broadening and concurrently nonlinear effects are negligible. Similarly, it is highly recommended to remain small dispersion after using a dispersion compensating fiber.

One of the first concepts of dispersion control was proposed by R. Dyott et al. in Ref. 18. In the concept, the waveguide dispersion is controlled changing the difference in core and cladding indices and by choosing an operating point according to the higher-order mode cut-off. The higher-order mode cut-off is strongly dependent on the core dimension. In this way, the waveguide dispersion can counteract the effect of material dispersion and

achieve total zero dispersion in the restricted wavelength range.

The mechanisms of dispersion control are similar for both PCF designs: near zero dispersion fibers and dispersion compensating fibers. Nevertheless, a PCF with a dual core, where the greater core is created by removing or reducing the airhole diameter in selected rings, is primarily used to achieve a large negative dispersion parameter. It is therefore the modes of both cores matches at a specific wavelength that results in high dispersion that can be used for the compensation. [A.3]

2.2.1 Doping the Fiber Core

The inclusion of a small doped region to a PCF core causes the index contrast between pure silica and the doped region that increases mode confinement. Since waveguide dispersion is strongly dependent on mode confinement and because the effective core is so small that its diameter is of the range of the propagating wave, the inclusion can decrease the waveguide dispersion.

On the other hand, doped regions affect material dispersion that can balance waveguide dispersion. Y. Hoo et al. in their study [19] showed that by proper controlling the size of the core with concentration of 3% GeO_2 dopant, the material dispersion is well balanced by the waveguide dispersion and the chromatic dispersion can be less than 0.06 $\mathrm{ps{\cdot}nm^{-1}{\cdot}km^{-1}}$ [19].

The technique of inserting a high-index rod in the PCF core has been proposed by V. Rodriguez-Esquerre et al. [20] to achieve a near-flat dispersion parameter about -200 $\mathrm{ps{\cdot}nm^{-1}{\cdot}km^{-1}}$ in the spectral range of 1390 to 1700 nm. It allows for dispersion compensation in one transmission channel making it being unsuitable for current transmission systems using wavelength-division multiplexing.

The high-index doped rod can be surrounded by three low-index doped regions with three airholes [A.7]. The presence of different dopants in the fiber core provides new possibilities to control light. The PCF exhibits flat and negative dispersion parameter lower than -430 $\mathrm{ps{\cdot}nm^{-1}{\cdot}km^{-1}}$ from 1300 to 1700 nm. Moreover, the use of fluoride compounds in the selected regions as well as in the background is studied in the doctoral thesis. Such a fiber structure was originally developed by K. Hansen to fabricate highly nonlinear fiber with near zero dispersion [21]. [A.2]

2.2.2 Airholes Close to the Fiber Center

A fundamental mode can be confined within the core by the index contrast between pure silica and airholes located close to the fiber center, resulting in effective mode diameter small enough to control dispersion in the desired way. A nine-ring fiber design [22] with an effective mode area of 4.24 $\mu\mathrm{m}^2$ can be one of the solutions. The minimum of dispersion parameter, -435 $\mathrm{ps{\cdot}nm^{-1}{\cdot}km^{-1}}$ is numerically obtained as well as the residual dispersion ± 64 $\mathrm{ps{\cdot}nm^{-1}}$ from 1460 to 1630 nm.

A conventional hexagonal PCF with a small effective mode area about 1.6 $\mu\mathrm{m}^2$ was designed and investigated in another paper [23]. The PCF has the same airhole diameter

in all airhole rings of the structure and only two parameters: airhole diameter and hole-to-hole spacing are optimized in order to find the best achievable match of dispersion slopes between the designed fiber and NDSF. The designed fiber has a suitable dispersion slope in the 236-nm broad range as well as a normal chromatic dispersion of -474.4 ps·nm^{-1}·km^{-1} at the wavelength of 1550 nm.

Tighter mode confinement than in hexagonal lattice, and thereby the possibility to control dispersion more can be achieved by a PCF based on octagonal, decagonal or circular (i.e. having holes located at the concentric circles) structure for its lower refractive index around the core that is caused by the presence of higher amount of airholes in the fiber cladding. It has been shown by M. Habib et al. through the simulation results that an octagonal PCF design [24] can exhibit the negative dispersion parameter about -418 to -775 ps·nm^{-1}·km^{-1} over the S-, C-, and L-bands and an RDS close to that of the NDSF.

An alternative way to control the mode confinement is to introduce a defect into the fiber center [25]. The central defect is usually obtained by an airhole spreading the mode toward the cladding, where it is strongly confined, and thus the effective mode area is smaller. The negative and flat chromatic dispersion parameter about -230 ps·nm^{-1}·km^{-1} has been numerically achieved in Ref. [25] due to the small effective mode area of 5 μm^2 controlled by an elliptical airhole in the fiber center. Moreover, the asymmetry can maintain single polarization of radiation. The fiber can be used for dispersion compensation eliminating polarization mode coupling and polarization mode dispersion. [A.2]

2.2.3 Dual Concentric Cores

The negative chromatic dispersion parameter can be achieved in PCFs with dual concentric cores. The both cores act as parallel waveguides with different effective indices. Coupling between both modes occurs and is maximal at a phase matching wavelength, where the difference between effective indices is minimal. For the wavelengths shorter than the phase matching wavelength, the field is confined mainly in the inner core. The phase and loss matching conditions around the phase matching wavelength are satisfied and the field of one mode transfer to the other mode. The field at the wavelengths longer than the phase matching wavelength spreads to the outer core, where the outer defect mode is propagated. The couple mode theory is described in detail in Ref. 26.

The phase matching is dependent on a fiber geometry and yields high dispersion [27]. As far as dispersion achievable by this technique is concerned, the value of $-39,500$ ps·nm^{-1}·km^{-1} is presented in Ref. 28, where one of the cores is created by filling the airholes in one ring with hydrogen dioxide. However, the high negative dispersion parameter is achieved in the narrowband of wavelengths of 7.4 nm, not sufficient for broadband dispersion compensation.

Over the last few years, designers aim to extend the operating bandwidth of dual-core fibers. It is worth to notice one in Ref. 29, where a dual-core PCF with two cladding layers [29] having different hole-to-hole spacing and airhole diameter is designed. Although the fiber chromatic dispersion parameter is not less than -100 ps·nm^{-1}·km^{-1}, the fiber can compensate dispersion of the NDSF over all the telecommunication bands. The PCF is

designed to match dispersion slope of the NDSF at 1550 nm and, concurrently, to achieve the same zero dispersion wavelength as the NDSF. Moreover, the phase matching is set beyond 1650 nm to decrease the influence of the outer defect mode which yields a large positive dispersion parameter.

Integration of amplification into a DCF would be advantageous. It can be done by rare-earth doping the fiber and by adding the appropriate laser pump. Recently, the possibility of erbium doping in a dual-core PCF has been considered [27].

A particularly important property of a dual-core PCF as identified by S. K. Varshney et al. is its ability to form the outer core sufficiently leaky and design a photonic crystal fiber filter [30]. Since the outer core is responsible for the leaky defect mode at longer wavelengths (stop-band), the inner core is doped by fluorine to obtain the other stop-band concurrently at short wavelengths. The fluorine doped core is responsible for the strong energy transfer between the inner and outer core at the short wavelengths. It is therefore, the doping decreases the effective refractive index and its value is similar to that of cladding region. The achieved pass-band can be wide: from a few nanometers to about 500 nm in the wavelength band from 1250 to 1750 nm. [A.2, A.11]

2.2.4 Suspended Core Fibers and Exposed Core Fibers

An innovative type of a PCF for evanescent field sensing dates back to 2001, when M. Monro et al. proposed so-called "suspended core fiber (SCF)" [31]. The typical SCF cladding consists essentially of air and the core is suspended via few tin silica struts. The high air-filling fraction, (the fiber cladding is almost air), lets to design SCFs with small cores and high numerical apertures (NAs) that are difficult to make in conventional PCFs. Moreover their fiber drawing technology is matured, one of the novel fabrication techniques for SCFs was developed by A. Webb et al. [32].

In the technique, the airholes are predefined by mechanical drilling of the fiber preform, and further they are manipulated during the fiber draw. The technique is much quicker and more straightforward compared to the conventional stack-and-draw technique [33], in which the glass rods must be stacked together to create the preform. On one hand, an SCF offers ease of fabrication comparable to that of a PCF. [34] On the other hand, designs are limited by much simpler geometry with the following design parameters: core size, number and width of the solid struts. This is enough to design the SCF with one or two zero dispersion wavelengths (ZDWs) [35]. However, it can be a challenge to design an SCF with the flattened dispersion property or for the dispersion compensation.

Since the SCFs can be designed with sub-wavelength core sizes (< 1 μm), the propagated light is no longer primarily confined to the core and spreads out to the surroundings medium (usually represented by liquid or gas). The strong light interaction with that medium allows achieving high modal sensitivity and this approach is of a particular interest for applications in biological and chemical sensing [36, 37]. The SCF filling process by gas species has been theoretically studied in Ref. 38 for different fiber length and airhole size. The study was experimentally validated filling the SCF samples with low-pressure acetylene gas. Once the fiber is filled, the transmission spectrum can be analyzed.

The gas filling process can be complicated in real-time sensing, due to the necessity of the gas refiling process of which duration can be longer than the measurement period. The time needed to fill SCFs can be as long as 7 hours for gas diffusion or $\sim$ 100 minutes for water, depending on interaction length and size of the holes. [39]. Research continued in order to overcome this problem.

The first exposed core fiber (ECF) was proposed by Y. Hoo et al. for high sensitivity gas detection. [40] The fabrication of the ECFs allows only minimal deviation from the conventional drawing process; the only additional step is lateral holes drilling into the preform to expose the core before the drawing [41]. Some details of other fabrication processes for the ECFs are outlined in Ref. 42.

2.2.5 Leakage Channel Fibers

One of glass properties is nonlinearity [13, 43] associated with significant nonlinear effects as stimulated Raman and Brillouin scattering that occurs in a fiber. The generally accepted view is that the scattering can reduce the quality of the delivered beam and decreases the maximum allowable input power [44, 45]. Limiting nonlinear effects are usually reduced by increasing fiber effective mode area [44]. However, the maximal size of the effective mode area in a step index fiber has two fundamental limitations.

Firstly, to keep the high beam quality, the LMA fibers should be single-mode guided. To maintain the single-mode operation for specific core radius r, the required fiber numerical aperture is given from Eq. (2.1):

$$NA < \frac{2.405 \cdot \lambda}{2 \cdot \pi \cdot r}. \tag{2.1}$$

Owing to the limited fabrication technology it is usually difficult to obtain the NA lower than 0.05 in an optical fiber [46]. It is obvious that the core radius cannot be lower than about 11.5 μm for the fiber to be single-mode at the wavelength of 1.5 μm.

Since PCFs exhibit higher design flexibility than conventional single-mode fibers, the presence of airholes or doped rods in the PCF structures allows for fabricating single-mode PCFs with the greater cores [47, 48]. The effective mode area can be as large as $75,000\ \mu\text{m}^2$ in the chalcogenide PCF, where the single-mode condition is confirmed in an equivalent step index fiber by approximating the PCF [47]. The single-mode operation can be further comprehended owing to the differential leakage loss induced between the fundamental mode (FM) and higher-order modes (HMs) [48]. In this context, the fiber structure is tailored to make all the propagation modes effectively leaky, but not the fundamental one that is confined enough in the core. Such a fiber is known as a leakage channel fiber (LCF) and typically consists of a small amount of large airholes or doped rods ensuring that the leakage loss of the FM is usually lower than 0.1 $\text{dB}\cdot\text{m}^{-1}$, whereas the HMs suffer the losses from few to tens of $\text{dB}\cdot\text{m}^{-1}$ depending on a design and application [44, 49, 50, 51].

Secondly, a reduction of the NA causes that the modes become leakier, if a fiber is bent [45, 52]. Further, an attention must be paid owing to the HMs that can be confined more than the FM inside the core, when the fiber is bent. For example, a single-mode

tellurite fiber with effective mode area of 3000 μm^2 should be kept straight for generating supercontinuum from 0.9 to 2.5 μm as reported in Ref. 53. Fiber bend is usually described as increased attenuation, however, as summarized in Ref. 54, bending a fiber can yield the negative dispersion parameter as high as $-185,420$ ps·nm^{-1}·km^{-1}.

Over the last few years various attempts have been made to reduce loss of bent LMA fibers. The moderate bending radii are usually acceptable for LCFs and the much lower radii are possible at modified LCFs with an asymmetric refractive index distribution [49, 50, 51, 55]. Such a fiber has recently been presented by M. Chen et al., the fiber comprises of two regions with different airhole diameter on the opposite sides of the fiber cross-section [49]. If the fiber is bent in the proper plane, the FM is confined enough by larger airholes, whereas the HMs are effectively leaky. Instead of larger airholes M. Napierala et al designed and fabricated a LCF with larger amount of airholes on one side of the fiber, the fiber allow bending around 10 cm radius and have effective mode area over 1000 μm^2 at 1.064 μm [50]. Due to the asymmetry, the fiber bend should be oriented only in the specific range of angles that requires microscope control and fixation, for example on a precise fiber rotator [51].

However, the nonlinearity of chalcogenide [56] and tellurite [57] glasses is two or three orders of silica glass that cannot be suppressed enough by larger mode area [58, 59]. Chalcogenide glasses has a larger refractive index in comparison with tellurite glasses and a higher nonlinear index. The larger refractive index leads to a greater modal confinement and a higher nonlinearity. In general, their nonlinearity is key for supercontinuum generation [60]. LMA of chalcogenide fibers is rather suitable to enhance limit for the optical power induced damage [61], due to the low melting point of the chalcogenide and tellurite glasses. The low melting point about 310 and 850 °C, respectively causes that the high pump power required to generate SC can damage chalcogenide or tellurite fibers especially for the picosecond and longer pump pulses [62, 63, 64]. On one hand, nonlinearity is decreasing with large effective mode area, but, on the other hand, the limit for power induced damage is significantly increased.

2.2.6 Supercontinuum Generation

A supercontinuum is coherent light that expands from a pump laser source through a nonlinear medium to a broad wavelength spectrum. Supercontinuum sources found their way in many applications including telecommunication [65], optical coherence tomography [66], fluorescence microscopy [67] and spectroscopy [68] among others.

SC was firstly observed in borosilicate glass sample as proposed by R. Alfano et al. in 1970 [69] and later in a conventional single-mode fiber by P. Baldec et al. [70]. Since the pioneering work of J. Ranka et al. [71], there has been considerable interest in supercontinuum generation in photonic crystal fibers, because of their good tunability especially of the zero dispersion wavelength. Spectral position of a ZDW is one of the key parameters for SC generation. ZDW should not be far from the pump wavelength, otherwise only a low amount of the pump power leaks from normal to anomalous dispersion regime. A large mismatch of group velocities decreases SC bandwidth. In conventional SMFs it is

too challenging to shift the ZDW bellow their material zero dispersion wavelengths and to generate strong SC in the visible region. Pumping the silica photonic crystal fiber in the anomalous dispersion regime at 820 nm as reported by J. Price et al. in Ref. 72, the supercontinuum can extend from 1600 up to 300 nm in the ultraviolet.

SC was experimentally demonstrated for pumping a silica PCF in both normal [73] and anomalous [74] dispersion regimes. It should be noticed that if power level of the SC reaches infrared loss edge of the material, the bandwidth becomes independent on the ZDW [75].

Since the transparent spectrum of silica is strongly limited, suitable host materials have been used to extend the edge beyond the limit. Several materials have been proposed in this context as fluoride [76], tellurite [77] and chalcogenide [62] glasses. On one hand, the nonlinearity of fluoride glasses is comparable to that of silica, but, on the other hand, zero material dispersion wavelength of the most fluoride glasses is in the C and L-bands [76], where most of commercially available lasers operate. G. Quin et al. demonstrated wide SC generation up to 6.28 μm in the 2-cm fluoride fiber pumped by a 1450 nm femtosecond laser [8]. They predicted that a fluoride fiber can be a promising candidate to generate wide SC up to 8 μm.

Contrary to silica and fluoride glasses, the material dispersion of tellurite and chalcogenide glasses is zero at much longer wavelengths, as shown in Appx A and at these wavelengths it can be difficult to find a proper laser pump. Therefore, significant efforts are placed on a fiber optimization to shift the ZDW onto the C-band.

For this reason, the small effective mode area is required to increase the waveguide dispersion in the desired spectral region. Moreover, the SMA promises higher nonlinear effect that are key for SC generation. Concerning the fabrication efforts of SMA fibers, suspended core fibers are preferred over conventional PCFs [32]. Varying the core size and the width of the solid struts in an SCF, the ZDW can be shifted toward the injected pump wavelength. Moreover, if the mode area is small enough, it is possible to obtain two ZDWs. This approach was adopted in Ref. [78]. ZDWs experience a shift towards each other increasing the width of the solid strut and decreasing the core size, which can lead to near zero dispersion in 1-μm wide wavelength range. However, attention should be paid, when the core size is decreasing, due to the confinement loss that can be too high at longer wavelengths [79]. A number of experiments were performed in order to investigate SC generation by pumping near the ZDWs. One of them was carried out by simultaneous dual-wavelength nanosecond pumping near both ZDWs of a PCF [80]. Recently, the broadest SC ever reported from 1.4 to 13.3 μm was presented by Ch. Petersen et al. in Ref. 81. The SC is generated by pumping an 85-mm long step index chalcogenide fiber by 100 fs pulses with a repetition rate of 1 kHz and peak power more than 7 MW.

Supercontinuum can also be generated in LMA fibers especially if the highly nonlinear glass is used as the fiber background. As identified by X. Feng et al. in Ref. 53, the SC can be generated in the fiber with effective mode area about 3000 μm^2 that is one of the largest. The SC is as broad as 1.6 μm if 12 fs laser at 15.2 mW is being pumped inside a 9-cm long piece of the tellurite fiber. SC can also be observed in silica LMA fibers as observed by R. Cherif et al. They used a PCF with effective mode area of 180 μm^2 to generate

SC extending from 600 to 1700 nm [82]. Pumping the PCF by Ti:Sapphire amplifying system, the spectral flatness variation less than 12 dB is obtained over the bandwidth. SC generation in a highly nonlinear PCF is one of the parts of this doctoral thesis presented in Sec. 4.4.1.

Chapter 3

Methods and Design Principles

3.1 Methods

Since there is no analytical tool to predict the key properties of optical waveguides, e.g. chromatic dispersion, confinement loss and effective mode area, numerical tools are required to investigate high design flexibility of photonic crystal fibers. In general, the mainly used numerical methods are the modal expansion method [83], multipole method [84], finite element [85], and finite difference method [86]. The methods also perform well for PCF designs. Each of the methods has its pros and cons as summarized in Ref. 87.

3.1.1 Finite Difference Frequency Domain Method

In this doctoral thesis, the modal properties of designed fibers are numerically calculated using a commercially available software. Full-vectorial finite difference frequency domain (FDFD) method implemented in the software is similar to that described by Z. Zhu and T. Brown [83]. FDFD method is widely used for electromagnetic computations for its verified validity and effectiveness that was demonstrated in standard fibers as well as in PCFs [83].

In the simulation environment, the computing domain is dived by uniform mesh and covers the investigated area. The mesh size is set to be small enough to obtain reasonably accurate results, while ensuring good time efficiency. Perfectly matched layers (PMLs) are used at the edge of the domain as a boundary condition in order to accurately account for the confinement loss. The layers absorb the incident radiation without any reflections back to the computing domain. Thus, it is considered that the fiber edges are far enough from the fiber center and the back reflection is negligible.

In the computing domain, the Maxwell's equations are discretized into the matrices of linear equations that are solved using the sparse matrix technique with the unknowns being the electromagnetic field values on the mesh. With the PMLs, the system matrix becomes complex valued. Effective refractive index n_{eff} is obtained through this technique as well as the modal fields of the investigated waveguide at each mesh point.

The finite difference method employed in the solver uses Yee's mesh algorithm [88] to form Maxwell's equations as the matrix of eigenvalue problems. The equations near interfaces between a background material and airholes are described by Lumerical's conformal mesh method, which is an extension of a method described by Yu and Mittra [89]. [A.2, A.11]

3.1.1.1 Chromatic Dispersion in a PCF

An optical pulse with mean carrier angular frequency ω_0 and with electric field envelope $A(t)$ that represents a slowly varying function of time as compared to e^{jw_0t} propagates through a single-mode fiber under absence of loss, nonlinearity and birefringence according to Eq. (3.1):

$$E(z,t) = A(t) \cdot e^{j\omega_0 t} \cdot e^{-j\omega\beta(\omega)z}, \tag{3.1}$$

where $E(z,t)$ is electric field intensity as a function of time t and spatial position z, ω is angular wave frequency and β is phase constant.

An effect of chromatic dispersion is illustrated in Eq. (3.1) as a nonlinear relation between phase constant and angular frequency that can be defined as in Eq. (3.2) via Taylor expansion around ω_0 if the envelope changes are slow enough.

$$\beta(\omega) = \beta_0(\omega_0) + \frac{\partial\beta_0}{\partial\omega}(\omega-\omega_0) + \frac{1}{2!}\frac{\partial^2\beta_0}{\partial^2\omega}(\omega-\omega_0)^2 + \frac{1}{3!}\frac{\partial^3\beta_0}{\partial^3\omega}(\omega-\omega_0)^3 + ..., \tag{3.2}$$

where the first term, β_0, does not cause any effect on the pulse envelope, it describes a certain phase shift. Phase velocity v_f of the optical carrier at angular frequency ω_0 is established by β_0 as in Eq. (3.3):

$$v_f = \frac{\omega_0}{\beta_0} = \frac{c}{n_{eff}}, \tag{3.3}$$

where c is light velocity in vacuum. The second term leads to overall time delay, group delay τ_g of the envelope per unit length, but without modifying the envelope. The phase velocity is not unique along the spectral width. The carrier at angular frequency ω_0 propagates with velocity associated with the β_0, while the envelope propagates with velocity of all spectral components called group velocity v_g. The inverse group velocity is given in Eq. (3.4):

$$\frac{\partial\beta_0}{\partial\omega} = \beta_1 = \frac{1}{v_g}. \tag{3.4}$$

The group delay cen be defined as in Eq. (3.5):

$$\tau_g = \frac{z}{v_g}. \tag{3.5}$$

The third term (quadratic) represented as β_2 known as chromatic group velocity dispersion is responsible for spreading the envelope and amplitude reduction. The pulse form is modified, while the energy is constant. In optical waveguides, the chromatic dispersion is

usually presented by chromatic dispersion parameter D in Eq. (3.6). It directly refers to the pulse spreading per unit of wavelength per unit of waveguide length.

$$D = -\frac{2\pi c}{\lambda^2} \cdot \frac{\partial^2 \beta_0}{\partial {\omega_0}^2} = -\frac{2\pi c}{\lambda^2} \cdot \beta_2 \tag{3.6}$$

that can be rewritten as in Eq. (3.7)

$$D = -\frac{\lambda}{c} \cdot \frac{\partial^2 \Re[n_{eff}]}{\partial \lambda^2}, \tag{3.7}$$

where λ is wavelength and n_{eff} is obtained by the FDFD. The fourth and higher terms are responsible for higher-order dispersion. The third-order dispersion is related to the dispersion slope.

Chromatic dispersion parameter D, Eq. (3.7), is the sum of waveguide dispersion parameter D_w and material dispersion parameter D_m, Eq. (3.8):

$$D(\lambda) = D_w(\lambda) + \Gamma(\lambda) \cdot D_m(\lambda), \tag{3.8}$$

where Γ is confinement factor that for silica is close to unity.

The waveguide dispersion can be obtained by Eq. (3.7), where n_{eff} is calculated through FDFD for constant refractive index of the used background material n. The waveguide dispersion is related to the used fiber profile, which has a significant effect on the group velocity. In general, contradictory to the material dispersion, the waveguide dispersion cannot be predicted by any analytical approach and the only way to determine its dependence on the wavelength is by numerical calculation through the one of the methods. However, the mode properties can be evaluated for simple PCFs that is designed only by hole-to-hole spacing Λ and airhole diameter d omitting the numerical methods as presented by K. Saitoh et al. in Ref. 90. They provide empirical relations based on the parameters for normalized frequency and transverse attenuation constant of which knowledge enables straightforward calculation of n_{eff}.

The material dispersion occurs due to the interaction between an electromagnetic wave and the bound electrons of a material resulting in a frequency dependent refractive index. The material dispersion is obtained straightforward by substituting n_{eff} in Eq. (3.7) by refractive index n. Refractive index of a given glass is widely expressed in an analytical form by Sellmeier [91], Eq. (3.9), or by another approximating formula for example by Cauchy formula. [92] that is valid in the visible region, but it significantly deviates outside this region.

$$n(\lambda) = \sqrt{1 + \sum_j \frac{B_j \cdot \lambda^2}{\lambda^2 - C_j}}, \tag{3.9}$$

where B_j (-) and C_j (μm^2) are Sellmeier coefficients quoted for wavelength in micrometers.

For doped silica by boron trioxide B_2O_3 and fluorine F for refractive index decreasing, or by germanium dioxide GeO_2 and phosphorus pentoxide P_2O_5 for its increasing; empiric

formulas [93], Eqs. (3.10), (3.11), (3.12), and (3.13), respectively, offer good agreement with the measured values of the refractive indices from 0.9 to 1.7 μm.

$$n_{B_2O_3}(\lambda) = n_{Si}(\lambda) + 3.7640 \cdot 10^{-4} \cdot d_{B_2O_3}, \tag{3.10}$$

$$n_F(\lambda) = n_{Si}(\lambda) + 4.665 \cdot 10^{-3} \cdot d_F, \tag{3.11}$$

$$n_{GeO_2}(\lambda) = n_{Si}(\lambda) + 1.4145 \cdot 10^{-3} \cdot d_{GeO_2}, \tag{3.12}$$

$$n_{P_2O_5}(\lambda) = n_{Si}(\lambda) + 1.652 \cdot 10^{-3} \cdot d_{P_2O_5}, \tag{3.13}$$

where $n_{P_2O_5}$, n_F, n_{GeO_2}, and $n_{B_2O_3}$ are refractive indices of P_2O_5, F, GeO_2, and B_2O_3, respectively; $d_{P_2O_5}$, d_F, d_{GeO_2}, and $d_{B_2O_3}$ are their dopant concentrations in Mol.%.

Appx. A provides Sellmeier coefficients for the materials used in this doctoral thesis. Based on the coefficients, the refractive index wavelength dependence as well as the material dispersion is figured in Appx. A.

3.1.1.2 Loss and Effective Mode Area in a PCF

Loss in a PCF occurs similarly as for the conventional single-mode fibers and the minimum attenuation in a PCF is of a similar value around 0.2 dB·km^{-1} at 1550 nm [94]. Total loss comprises the structural imperfection loss, Rayleigh scattering, hydroxyl and infrared absorption, among others.

On the contrary to conventional SMFs, PCFs have leaky cladding. In theory, no leakage or so-called confinement loss L occurs in a PCF with ideal cladding of an infinite number of airholes. In a real fiber, the guided modes are leaky due to core refractive index being the same as the refractive index of cladding beyond airholes. The confinement loss is wavelength dependent and can be controlled by fiber geometry. Generally speaking, increasing a number of airhole rings surrounding the core exponentially reduces confinement loss. Similarly, the modes are more confined for larger diameters of airholes. On the other hand, a designed fiber should have the minimum number of airholes to ease potential fabrication. Moreover, it is not possible to fabricate a fiber with diameters of similar sizes as hole-to-hole spacings. Thus, a tradeoff should be found. Generally accepted view is that confinement loss should be kept below the Rayley scattering.

Since large air-filling fraction d/Λ is usually required to remain low confinement loss, the single-mode condition, Eq. (3.14), is not satisfied in a PCF and not only the fundamental mode can propagate in [95].

$$d/\Lambda < 0.406, \tag{3.14}$$

The confinement loss can be calculated from the imaginary part of the effective index, according to Eq. (3.15):

$$L = \frac{20}{\ln 10} \cdot \frac{2\pi}{\lambda} \cdot \Im[n_{eff}], \tag{3.15}$$

Effective mode area A_{eff} is key for calculating nonlinear coefficient γ, Eq. (3.16), splicing loss L_s, Eq. (3.17), and numerical aperture, Eq. (3.18).

$$\gamma = \frac{2\pi n_2}{\lambda \cdot A_{eff}}, \tag{3.16}$$

$$L_s = -20 \cdot \log \frac{2 \cdot w_{SMF} \cdot w_{PCF}}{w_{SMF}^2 + w_{PCF}^2}, \tag{3.17}$$

$$NA = \sin\theta, \tag{3.18}$$

where n_2 is nonlinear refractive index, w_{SMF} and w_{PCF} is spot size of the single-mode and photonic crystal fiber, respectively. Spot size w and half divergence angle θ are derived as in Eq. (3.19) and in Eq. (3.20), respectively:

$$w = \sqrt{\frac{A_{eff}}{\pi}}, \tag{3.19}$$

$$\theta \simeq \arctan \frac{\lambda}{\pi \cdot w} \tag{3.20}$$

The effective mode area is obtained from the mode field distribution as in Eq. (3.21).

$$A_{eff} = \frac{(\iint |E_t|^2 \, dxdy)^2}{\iint |E_t|^4 \, dxdy}, \tag{3.21}$$

where E_t is transverse electric field vector and the integrals are over the simulation region whose coordinates are x and y. The effective mode area is wavelength dependent and is increasing for waves with longer wavelengths. The mode area is reduced increasing the airhole diameter especially in the innermost rings or by decreasing the hole-to-hole spacings. Contradictory, the mode area is almost independent of the number of airhole rings.

Modes in fibers with large effective mode area are usually leaky too much with bending. In this case, the confinement loss for the bent fibers should be evaluated. It can be done by conformal mapping [96] in which the straight fiber coordinates of refractive index profile $n(x, y)$ are mapped to its equivalent straight fiber $n_{eq}(x, y)$ as in Eq. (3.22):

$$n_{eq}(x, y) = n(x, y) \cdot (1 + \frac{x}{r_{eff}}), \tag{3.22}$$

where the fiber is bent in x direction and r_{eff} is effective bending radius taking into account elasto-optic effect [96] that occurs due to an additional change in the refractive index with bending.

3.2 Convergence Testing

The FDFD method as well as other numerical methods that solve light modes cannot give exact answer; they always exhibit numerical errors. The numerical errors should be reduced to an acceptable level, of course, considering the simulation time and memory requirements. The accuracy of the FDFD is affected by many parameters of the simulation model, for example, by the mesh size, number of perfectly match layers (PMLs), their reflections, and the size of the computational cell. [A.2]

In general, Z. Zhu et al. verified that results fairly accurate can be get by keeping the mesh size at $\sim \lambda/15$ [86]. However, a fiber design with extremely small mode area usually require more accurate setting mainly due to the small hole regions near the fiber center. On the other hand, in most cases of LMA fiber modeling, the mesh size can be larger than to that recommended by Z. Zhu et al. Convergence testing of all the simulation parameters can find the optimal set of environment in which the simulation model is created. Z. Zhu et al. verified the proper grid size by comparing the modal characteristics using different mode solvers together with convergence of modal birefringence of the fundamental modes. It is clear from the numerical study by Steel et al. [97] that in symmetric waveguide structures, the two-fold degenerate fundamental modes are presented. Birefringence of the fundamental modes is as in Eq. (3.23):

$$B = |n_{eff,x} - n_{eff,y}| \,, \tag{3.23}$$

where $n_{eff,x}$, and $n_{eff,y}$ are the effective indices of the x and y polarized modes, respectively. The simulation model is verified because of the dependent birefringence of the symmetric waveguides to the model discretization. A fiber perfectly symmetrical eliminates birefringence and for ideal simulation set-up the calculated birefringence of two modes should be zero.

In a convergence test presented in this doctoral thesis, one of the parameters is varied in N simulation steps, for example, the size of mesh cell dx can be considered as a parameter. Result σ_i of each simulation step i is observed and saved. A finer mesh result can be σ_i that is then compared with result σ_{i-1} of the previous step $i-1$. If the results' difference $\Delta\sigma$ is nearly zero, it means that results stop changing, then the mesh size of $i-1$ simulation test is probably suitable for the design. The results' difference $\Delta\sigma$ is defined in the following equation (3.24):

$$\Delta\sigma(i) = \sqrt{\frac{\int (\sigma_i - \sigma_{i-1})^2 d\lambda}{\int (\sigma_i)^2 d\lambda}}. \tag{3.24}$$

In the absence of an exact solution, the error estimation of a simulation parameter at the step i is given by Eq. (3.25), taking into account that the result at step N is much closer to the exact solution than the result at step i:

$$\Delta\sigma_N(i) = \sqrt{\frac{\int (\sigma_i - \sigma_N)^2 d\lambda}{\int (\sigma_i)^2 d\lambda}}. \tag{3.25}$$

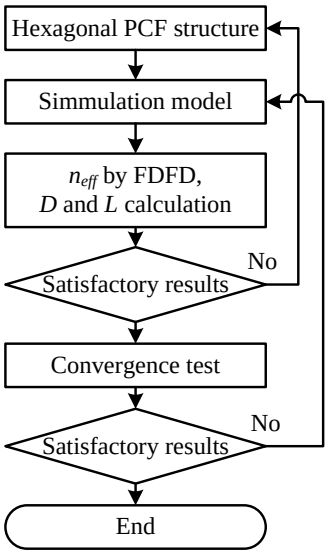

Figure 3.1: Flow diagram of the fiber design process

The best estimation of the error is for $i << N$.

The convergence test is used as the important part of the proposed fiber design process; the flow diagram is show in Fig. 3.1. In the first simulation run of the design process, the simulation model of a PCF is set for the fast calculation of n_{eff}. Then the results are examined and geometrical parameters optimized. Optimization process is discussed thoroughly in Sec. 3.3. In the optimization, the diameters of the innermost rings are usually varied as first; pitch is kept fixed in this step. It is therefore, the mode properties depend on d/Λ and it is not suitable to tune both parameters concurrently. Once the best possible properties with the specific pitch are found, the pitch is varied and the airhole diameters are optimized in a similar way. Results are compared and the best solution is selected and used for the convergence test of the simulation model of which error is examined.

On this basis, the simulation model is updated to minimize numerical errors. Especially the mesh size dx is usually reduced during this step.

Since the convergence is tested after the geometrical optimization, the simulation can run as fast as possible and the total design time is effectively shortened. Usually final optimization do not require major geometrical changes. At the end of the design process it is necessary to verify that simulation model is correct by convergence testing and, if it is appropriate, adapt the simulation model and the geometry of the fiber. In some cases the mesh size is not fine enough or the computing region can be too small for optimized geometry. [A.2]

A similar concept of convergence testing can be found in Lumerical simulation guidelines [98]. Convergence tests of the designed fibers in this doctoral thesis are presented in Appx. B.

3.3 Design Principles

3.3.1 Near Zero and Dispersion Compensating Designs

Let the author consider a conventional PCF with hexagonal cladding and a finite number of airholes. The main and sole background material of the PCF is silica whose refractive index is specified by using Sellmeier formula with the coefficients defined in Ref. 99, Appx. A. Using silica as the background can be still labeled as best for transmission of optical pulses in terms of transparency, attenuation, fabrication technology, price, and compatibility among others. [A.2]

The material dispersion of silica can be tuned by doping. However, the dispersion control possibilities are limited, the maximal concentration of dopants is of about $\simeq$ 20 Mol.% [93] and especially only small changes of the dispersion slope occurs with doping. The material dispersion of silica with different dopants is shown in Appx. A. The dispersion curves have nearly same shapes and they are shifted according to the dopant concentration.

The design power is stored in the waveguide dispersion and it is higher if the effective mode area is smaller. To obtain a small effective mode area, the spacing between airholes should be set to be similar size as the considered wavelength. In the proposed PCFs the chromatic dispersion is controlled mainly by structural parameters, such as airhole diameter and the spacing between airholes. The airholes of the three innermost rings have the main contribution to the dispersion control, whereas the airholes of the outer rings ensure low confinement loss. [A.2]

Generally, the waves at shorter lengths are predominantly confined in the core and longer waves extend more to the cladding. As a result, the waveguide dispersion decreases with tighter confinement of the fundamental mode, which is more significant at longer waves. Since the mode confinement and the effective mode area are mainly controlled by the dimension of the innermost ring, the desired slope of chromatic dispersion can be obtained by adjusting the first ring airhole diameter. In the small effective mode area PCF, the waveguide dispersion strongly depends on refractive index profile, and, as it has been observed in Ref. 100, the larger airholes in all the other rings increase the waveguide dispersion. This property is key in the fiber design process.

The influence of more distant airholes from the fiber center is limited. Since the airhole variation in the second innermost ring is responsible for the opposite effect on the dispersion slope than the variation in the third ring starting from the fiber center, one can concurrently tune both the second and the third ring, making the dispersion parameter higher or lower at all wavelengths. The second ring is closer to the core than the third one. It affects the properties of the propagated mode more, which is expected, therefore, the concurrent tuning is responsible for the slight changes in the dispersion slope. [A.2]

In near zero dispersion designs, the chromatic dispersion should be properly set to avoid nonlinear effects considering mainly the channel spacing, the fiber nonlinear coefficient and the input power. The effective mode area small enough is usually required to have the sufficiently strong waveguide dispersion in order to balance material dispersion of the

fiber.

As discussed in Sec. 3.4.1 the smaller mode area implies higher fiber nonlinearity and stronger nonlinear effects that can be undesirable for telecommunication links; however, the higher nonlinearity is key for the supercontinuum generation.

To balance chromatic dispersion penalty in a telecommunication line, a dispersion compensating fiber (DCF) should be designed to have a negative dispersion parameter as large as possible and, concurrently, to match its relative dispersion slope (RDS) to that of non-dispersion shifted fiber (NDSF) with the chromatic dispersion being typically 17 ps·nm^{-1}·km^{-1} and RDS of about 0.0034 nm^{-1} at the wavelength of 1550 nm [101]. However, the full dispersion compensation of NDSFs can be undesirable, if the channel spacing causes nonlinear effects that are limiting factors of transmission capacity. This issue is similar as for near zero dispersion fibers. In particular, systems using wavelength division multiplexing must have small residual dispersion D_r, represented as:

$$D_r = D_{NDSF} \cdot l_{NDSF} + D_{DCF} \cdot l_{DCF}, \tag{3.26}$$

where l_{NDSF} and l_{DCF} is length of the NDSF and the DCF, respectively. Further, D_{NDSF} and D_{DCF} are the dispersion parameters of NDSF and DCF, respectively. To utilize large bandwidth of the optical link, the dispersion slope of the single-mode fiber S_{NDSF} must be compensated by the dispersion slope of the compensating fiber S_{DCF}, while considering the residual dispersion. The absolute value of relative dispersion slope (RDS) for both: the single-mode fiber and DCF is equal:

$$RDS = \left|\frac{D_{NDSF}}{S_{NDSF}}\right| = \left|\frac{D_{DCF}}{S_{DCF}}\right|. \tag{3.27}$$

The aim is to optimize the geometry to have a proper relative dispersion slope around the central wavelength of the compensated spectral region and also to have zero dispersion of the dispersion compensating photonic crystal fiber (DC-PCF) near the zero dispersion of NDSF to obtain a usable spectrum as broad as possible. [29] It can be done by tuning the diameters of the three innermost rings, as described in Sec. 4.2.

The chromatic dispersion wavelength dependence for NDSF has been derived by the study by Nielsen et al. [101]. For designed fibers, chromatic dispersion parameter D and confinement loss L can be calculated from n_{eff} by Eqs. (3.7) and (3.15), respectively.

A fiber with the near zero and large negative dispersion is designed and investigated in Sec. 4.1 and 4.2, respectively.

3.3.2 Large Mode Area Designs

PCFs with effective mode areas larger than of about 50 μm^2 have limited possibilities to control chromatic dispersion by changing the structure of the investigated fiber; the waveguide dispersion is lower with larger core sizes and becomes negligible [53]. The goal for a LMA fiber design is being single-mode guided and bendable with low confinement loss.

It is too challenging to design a LCF with LMA that is reasonable bendable satisfying single-mode condition in Eq. (3.14). Therefore, the single-mode operation in the fiber is obtained by differential confinement loss for the fundamental and higher-order modes. Since the fiber length usually used in practical applications is around 3–10 m, the maximum loss value for the FM and the minimum loss value for the HMs is generally taken as 1 dB·m^{-1} and 10 dB·m^{-1}, respectively [51]. It should be noticed that these conditions should be satisfied also for the bent fiber up to at least 10 cm radius.

A typical LMA leakage channel fiber uses six airholes around the fiber center to confine the fundamental mode [44]. Increase in the airhole diameter reduces confinement loss of the modes for the both: straight and bent fiber. Applying this, not only the fundamental mode reduces its confinement loss, but also the higher-order modes, which may be undesirable. Instead of increasing the airhole diameter, it is rather suitable to add one or more airhole rings, thereby the loss difference between the fundamental and higher-order modes can be increased. However, to eliminate HMs, the airhole diameter of the additional rings is needed to be small. In such an improved structure, the first ring starting from the fiber center ensures low loss for the fundamental mode in the bent fiber, whereas the remaining rings make higher-order modes extremely leaky and concurrently confine sufficiently the fundamental mode as presented in details in Sec 4.2.

The proper setting of the airholes in a LCF structure is one of the particular interests of the doctoral thesis.

3.4 Basic Mechanisms of Supercontinuum Generation

3.4.1 Pulse Propagation Model

The supercontinuum generation in Sec. 4.4.1 is modeled by using the generalized nonlinear Schrödinger equation [60] that is expressed in Eq. (3.28). The equation describes both: linear and nonlinear pulse propagation.

$$\frac{\partial A(z,T)}{\partial z} = -(\sum_{k\geq 2} \frac{i^{k+1}}{k!}\beta_k \frac{\partial^k A}{T^k} + \frac{\alpha}{2})A(z,T) + i\gamma(1+\frac{i}{\omega_0}\frac{\partial}{\partial T})(A(z,T)\int_{-\infty}^{+\infty} R(t')\left|A(z,T-t')\right|^2 dt'), \tag{3.28}$$

where $A(z,t)$ is the slowly varying pump light electric field envelope in time $T = t - \beta_1 z$ of co-moving frame at group velocity β_1^{-1}, β_k are dispersion coefficients expanded by the Taylor series at carrier angular frequency ω_0 as in Eq. (3.2), γ is nonlinear coefficient, Eq. (3.16), and α represents the waveguide loss. Nonlinear Raman response function $R(t)$, Eq. (3.29), includes both instantaneous electronic and delayed Raman contributions.

$$R(t) = (1 - f_R)\delta(t) + f_R h_R(t), \tag{3.29}$$

where f_R is fractional contribution of the Raman response and delayed Raman contribution $h_R(t)$ is as in Eq. (3.30):

$$h_R(t) = \frac{\tau_1^2 + \tau_2^2}{\tau_1 \tau_2^2} e^{-\frac{t}{\tau_2}} \cdot sin(\frac{t}{\tau_1}), \tag{3.30}$$

where τ_1 defines the photon oscillation frequency and τ_2 is related to the characteristic damping time of the vibrating atoms. A reader can obtain further information about the pulse modeling via the generalized nonlinear Schrödinger equation in Refs. 60, 102, 103, 104,

In most cases, Eq. (3.28) is numerically solved by split-step Fourier method that solves the pulse propagation via nonlinear dispersive media. It offers an approximate solution that takes into account that dispersive and nonlinear effects can be solved independently for optical pulses propagating over the small steps from segment to segment along distance z with a small numerical error.

Firstly, in the initial segment the nonlinear effects of the propagating pulse are evaluated, while the dispersive effects are equal to zero. This is done at the step midpoint in the time domain. Next, the nonlinear effects are equal to zero and the dispersion and fiber loss are calculated over the step distance in the frequency domain. This is due to the reduction of the computational time, because the derivative in the time domain is transformed to the multiplication in the frequency domain. The field solution of the one step is calculated involving the dispersive and nonlinear effects, now both in the frequency domain and after that the solution is transformed back to the time domain. The resultant pulse shape is then used as the input for the next waveguide segment. Thus, the iterations are repeated for the entire fiber length to obtain final solution. The split-step Fourier method is described in details in Refs. 60, 103, 104, 105.

A solver used in the doctoral thesis for supercontinuum generation is based on the Matlab code presented in Ref. 60. The code provides a starting point practical enough for investigating basic principles of SC generation inside photonic crystal fibers.

3.4.2 Supercontinuum Generation in the Subpicosecond Regime

In Sec. 4.4.1, supercontinuum generation is investigated for the fiber pumped by subpisecond ($\leq$ 100 fs) soliton laser pulses (hyperbolic secant) with an envelope given from Eq. (3.31):

$$A(0,T) = \sqrt{P_0} \cdot \mathrm{sech}(\frac{T}{T_0}), \tag{3.31}$$

The subpicosend pumping is chosen, because many effects related to soliton dynamics can dominate and generate broader SC spectrum contrary to the picosecond or longer pulse pumping [106], where Raman scattering and four-wave mixing are considered as main effects.

In the normal dispersion pumping regime ($D < 0$), the pulse spectrum initially broaden symmetrically due to self-phase modulation. On the other hand, in the anomalous dispersion regime ($D > 0$), a soliton of order m is excited if the input parameters satisfy the condition in Eq. (3.32):

$$m = \sqrt{\frac{l_D}{l_{NL}}}, \tag{3.32}$$

where l_D and l_{NL} is characteristic dispersion and nonlinear length, expressed in Eq. (3.33)

and Eq. (3.34), respectively:

$$l_D = \frac{T_0^2}{|\beta_2|}, \tag{3.33}$$

$$l_{NL} = \frac{1}{\gamma \cdot P_0}, \tag{3.34}$$

where P_0 is peak power and T_0 is pulse duration.

Neglecting the high-order dispersion and Raman scattering, an ideal higher-order soliton periodically varies its temporal and spectral shape and recovers its initial state after distance $z_{sol} = \frac{\pi}{2} \cdot L_D$ [60]. However, considering these effects and subpicosecond pumping, the periodic pulse evolution is broken up through the soliton fission [102] at distance l_{fiss}, Eq. (3.35), where attains its maximum bandwidth.

$$l_{fiss} \sim \frac{l_D}{m} = \sqrt{\frac{T_0^2}{\beta_2 \cdot \gamma \cdot P_0}}. \tag{3.35}$$

At the fission length, the pulse is split into the m solitons, where each of them experience a shift to longer wavelengths, due to Raman amplification (soliton self-frequency shift) [107]. Peak powers P_s of m solitons are as in Eq. (3.36):

$$P_s = P_0 \cdot \frac{(2 \cdot m - 2 \cdot s + 1)}{m}, \tag{3.36}$$

where s represents an order in which the solitons are split from the higher-order soliton [60].

The most powerful of the solitons is the first one that mostly experience soliton self-frequency shift and emits nonsolitonic dispersive waves in the normal dispersion region, (another wavelengths components also stated as Cherenkov radiation [108]). The energy from the soliton is transferred, due to the presence of higher-order dispersion to a narrow-band resonance in the normal dispersion regime. Therefore, the higher-order dispersion affects evolution of the propagating solitons and reduces the magnitude of the self-frequency shift. The position of the resonance can be determined based on the phase matching condition [60]. Another significant effect of higher-order dispersion is that conserve the number of propagating solitons through the fiber [60]. As described in Ref. 109, the pulses in anomalous and normal dispersion regime can interact via cross-phase modulation and broaden the SC bandwidth.

A reader can found more information about subpicosecond SC generation in Refs. 60, 102, 103, 104, and 109.

Chapter 4

Results

4.1 Near Zero Dispersion Fiber

Fibers with near zero dispersion cover two fundamental applications. Firstly, they can substitute the combination of standard single-mode fibers with dispersion compensating fibers in telecommunication links. Secondly, the zero dispersion and close to zero dispersion are desirable for supercontinuum generation.

The efforts are made to design a fiber with chromatic dispersion as close as possible to zero at broad spectral range and to remain confinement loss well below Rayleigh scattering. It should be noticed that for practical applications in telecommunication, a fiber design should be performed with chromatic dispersion increased at all wavelengths by the nearly similar value to reduce nonlinear effects and to keep the flatness of the curve. In order to set the minimal value of the chromatic dispersion properly, the knowledge on transmission rate, channel spacing, modulation, power level and length of the fiber is required. (This investigation is not a part of this doctoral thesis).

To design the near zero chromatic dispersion, the three-fold symmetry [21] is improved by avoiding GeO_2 additives in the fiber core. Such a hexagonal PCF structure with fluorine-doped three-fold symmetry core (FD-TSC) is depicted in Fig. 4.1. The low-index doped regions enlarge the mode area and enhance dispersion properties. Contrary to other near zero dispersion designs presented mainly in Chap. 2, there is one parameter more (the doped regions) around the core that can control the chromatic dispersion; the chromatic dispersion can be controlled more precisely.

In the structure, only the fundamental mode is evaluated, since the higher-order modes suffer from high confinement loss exceeding few dB·m^{-1}. The core consists of a nondoped silica area surrounded by three fluorine-doped regions and three airholes. Further, the remaining six rings of airholes and silica core ensure very low confinement loss not exceeding $2.2 \cdot 10^{-3}$ dB·km^{-1} that is even more than adequate for the application. The pure silica with refractive index $n_{Si} = 1.4439$ at the wavelength of 1550 nm is used. The low-index regions with $n_F = 1.4351$ at 1550 nm are obtained by doping silica with 6.1 mol.% of the fluorine dopant. The Sellmeier coefficients can be found in Appx. A. The low-index

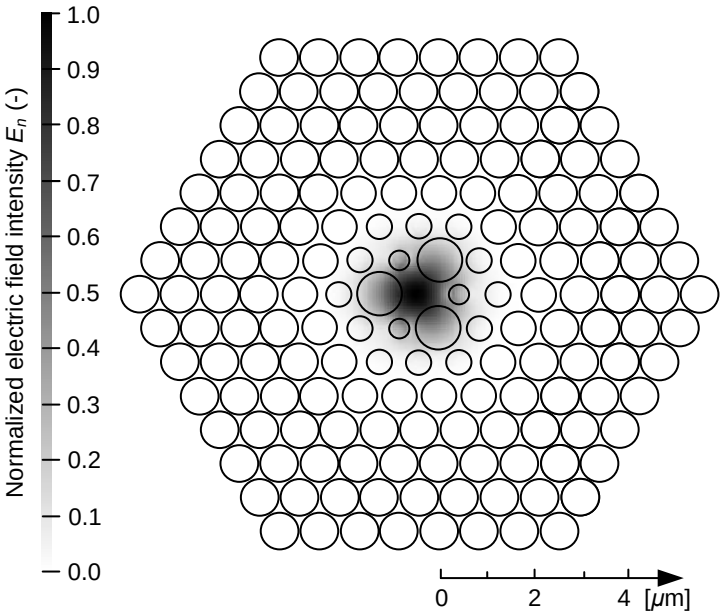

Figure 4.1: Cross-section and normalized fundamental mode field distribution at 1550 nm.

doped regions guide light as shown in Fig. 4.1, and therefore the effective mode area is larger in comparison to the same pitch designs, where the airholes of the innermost rings are reduced, similarly, but omitting the doped regions near the core. Furthermore, the same pitch designs suffer much larger confinement loss, because of the fundamental mode that cannot be confined in the core with such a low hole-to-hole spacing. In general, lower hole-to-hole spacing is desirable for better dispersion control.

The ultra-flattened nearly zero dispersion is obtained by fine tuning the diameter of the low-index regions, as well as the diameters of the three innermost rings. The airholes belonging to other rings are larger to ensure very low leakage loss. The variations in dispersion for each of the mentioned parameters are shown in Fig. 4.2 . The optimum fiber design exhibits dispersion varied between $\langle -0.12; 0.44\rangle$ ps·nm^{-1}·km^{-1} over the considered wavelength range $\langle 1250; 1700\rangle$ nm. Parameters for the optimal fiber design are: diameter of doped region $d_d = 0.91$ μm, diameter of the innermost airholes $d_1 = 0.384$ μm, second ring airhole diameter starting from the fiber center $d_2 = 0.511$ μm, third ring airhole diameter $d_3 = 0.74$ μm, diameter of outer airholes $d = 0.75$ μm and hole-to-hole spacing $\Lambda = 0.85$ μm.

Ultra-flattened dispersion curves are not restricted by the specific hole-to-hole spacing. Nevertheless, it has been verified throughout numerical simulations that the best results are achieved with the hole-to-hole spacing $\Lambda = 0.85$ μm. The larger values of Λ reduces the chromatic dispersion design options and smaller values of Λ increases the confinement loss.

The simulation model has been verified by the convergence testing to find a tradeoff between the simulation time and accuracy. The convergence tests of the mesh size and the

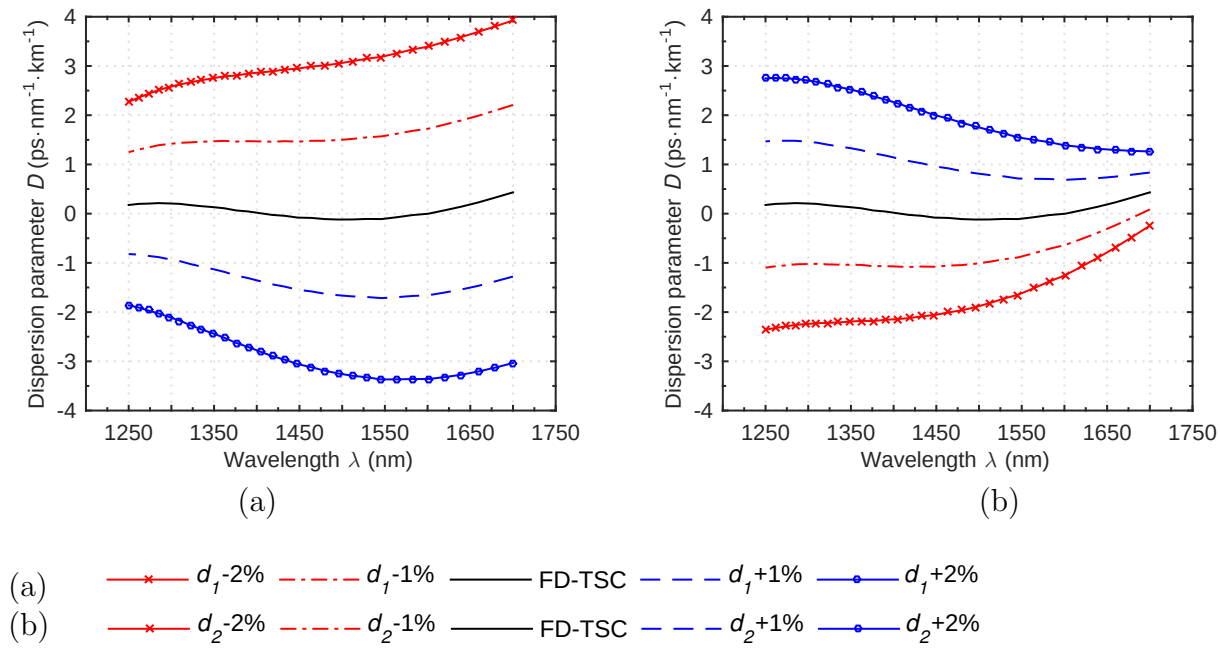

Figure 4.2: Nearly zero dispersion with deviations in diameter of airholes in the first (a) and the second ring (b) starting from the fiber center.

number of the perfectly match layers are shown in Fig. B.1, Appx. B.

Fig. 4.2 illustrates the wavelength dependence of the chromatic dispersion parameter for the nearly zero PCF, where diameter of airholes in the first and second rings starting from the fiber center is a studied parameter. The increase in d_1 or d_d causes the value of the dispersion parameter to decrease, which is contrary to the dispersion evolution observed for the adjustments of all the remaining rings. In such a case, the light is more confined in the core, if the innermost airholes and the low-index doped regions are made larger. In other words, more light is reflected back to the core and the effective mode area is smaller. The waveguide dispersion is increasing with the smaller innermost airholes, especially at longer wavelengths. This shift can be used to avoid nonlinear effects with small normal or anomalous-flattened dispersion over a wide range of wavelengths.

On the other hand, the dispersion parameter is increased with larger airholes in the remaining rings, as depicted in Fig. 4.2(b) and 4.3. In this case, the effective mode area becomes smaller, but the effective index of cladding is modified significantly and acts against the contribution of the decreased effective mode area to the waveguide dispersion. Nevertheless, the contribution of airholes in the third ring to the effective mode area is very low, and therefore the shifts of the waveguide dispersion are larger at longer wavelengths. The nearly opposite effect on the dispersion is found for airholes in the second ring.

The changes caused by the variation of airhole diameter in the third ring exhibit an opposite curve evolution found for the second ring, as shown in Fig. 4.3. Therefore, by

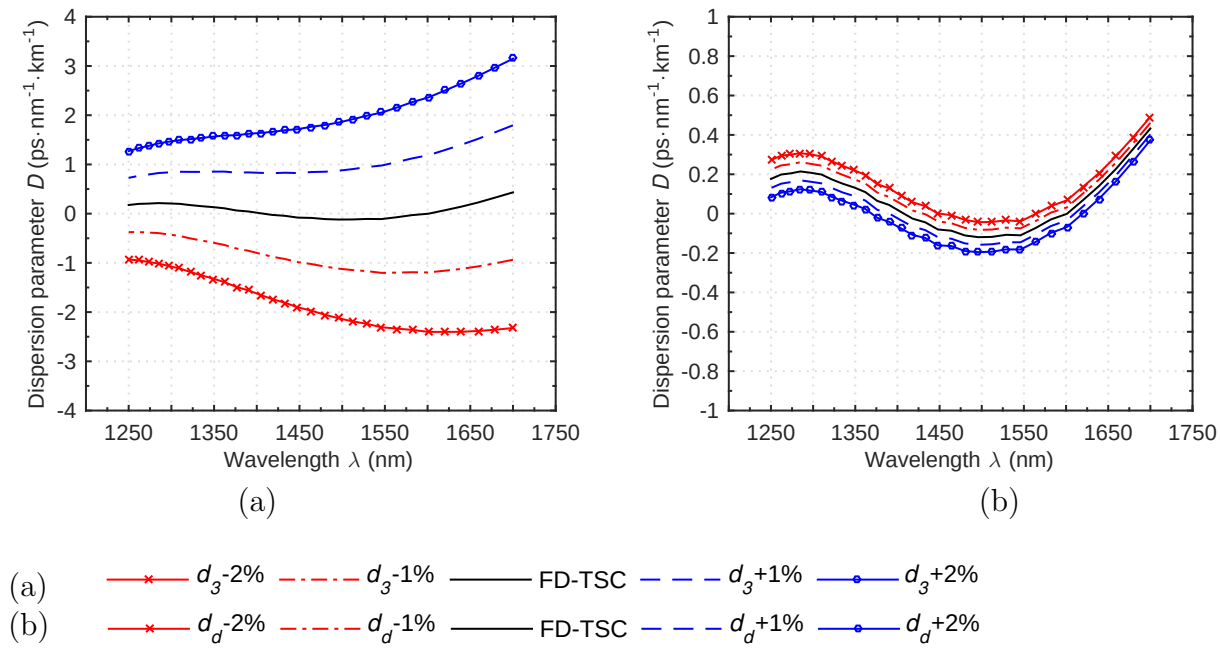

Figure 4.3: Nearly zero dispersion with deviations in diameter of airholes in the third innermost ring (a) and low-index doped regions (b).

properly combining the variation of airhole diameter in the second and third ring, the flattened regime of operation can be achieved.

The amount of light reflected from the low-index doped region to the core is low compared to the airholes belonging to the first ring. This is due to the smaller refractive index contrast. Furthermore, the fundamental mode is spread in the low-index doped regions, and therefore enlarging the low-index regions shifts the material dispersion curve towards shorter wavelengths.

An optimal evolution of the dispersion curve can be set by varying the airhole diameter in the low-index doped region, as shown in Fig. 4.3(b). In addition, attention should be paid to the fabrication process, especially to the diameter of airholes of the innermost rings. Here, the position of the dispersion curve is shifted by more than 1 ps·nm^{-1}·km^{-1}, since deviation is larger than 1 % for the hole diameter. Simultaneously, the curve character is changed, as well.

The diameter of airholes in the fourth to the seventh ring has little impact on the final dispersion curve. These airholes, enlarged by 2 %, cause the increase in chromatic dispersion parameter about 0.1 ps·nm^{-1}·km^{-1}, thus they are not dispersion tuning parameters and ensure low confinement loss. The change in hole-to-hole spacing is mainly responsible for the shift of the optimal curve. In other words, the shift about 1 ps·nm^{-1}·km^{-1} is caused by a +2% enlarging pitch. Finally, the fiber dispersion with different dopants around the core is modeled in Fig. 4.4. The waves with shorter lengths are more sensitive to the dopant

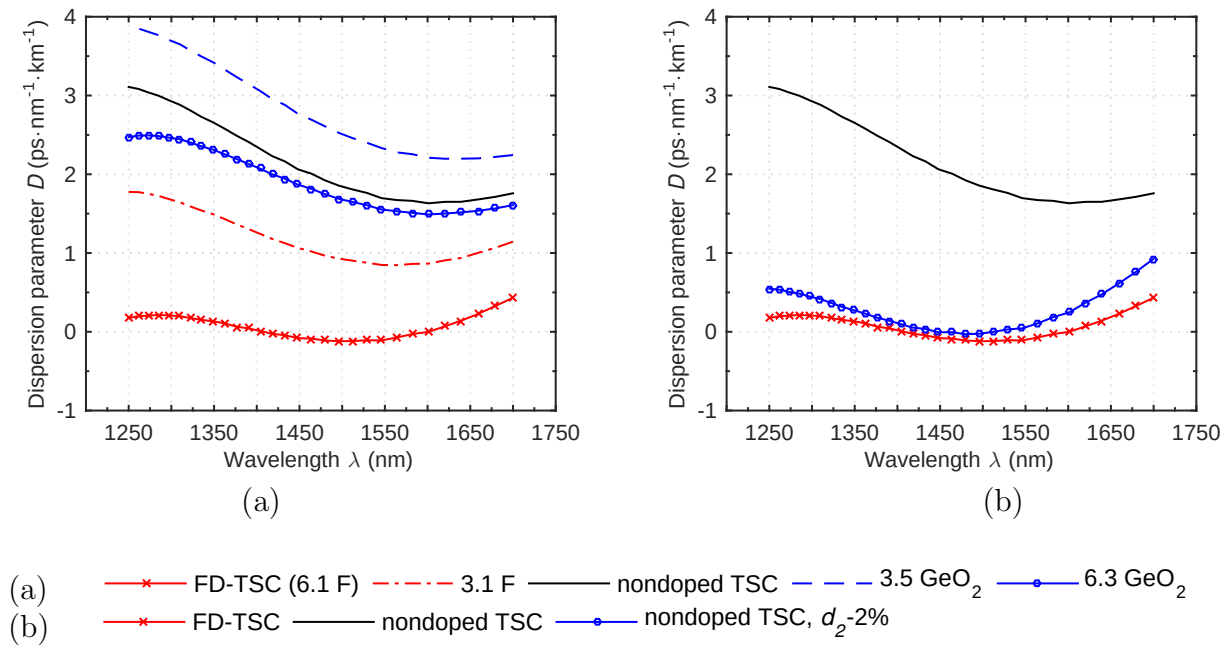

Figure 4.4: Nearly zero ultra-flattened dispersion with different dopants in the fiber cross-section

change. Therefore, the ratio between the refractive indices of silica and doped region is lower at the shorter wavelengths, which results in weaker light confinement. Further, the dopant change affects the material dispersion. Due to the possibility of controlling the waveguide dispersion of the three-fold symmetry core (TSC) structure, the nearly zero dispersion can be achieved with the both: refractive index decreasing or refractive index increasing dopant.

The satisfactory results can be obtained although doping is avoided, which imply fewer requirements on the fiber fabrication. Fig. 4.4 shows that the nearly zero dispersion can be achieved without doping by decreasing diameter of airholes of the second ring by 2 %. However, doping the regions allow more precisely tuning the dispersion. The optimal results are achieved by doping the silica with the 6.1.% mol of fluorine dopant. [A.1, A.3]

4.1.1 Summary

The nearly zero ultra-flattened PCF is investigated and designed. The presented fiber comprises the improved three-fold symmetry core doped by fluorine. It has been shown that the nearly zero dispersion can be achieved without high-index doping the fiber core. Required dispersion is achieved for larger operating bandwidth. The effective mode area is enlarged compared to existing studies. The designed fiber is not immune to deviations in geometry. The 1% change in diameter of the innermost rings causes the dispersion shift by more than 1 ps·nm^{-1}·km^{-1}. The slope and inflexion points of the initial curve are affected,

too.

This investigation demonstrates that the three-fold symmetry core can be composed without a high-index doped core, and thus doping can be significantly reduced. It is expected that doping the fiber core can be reduced in other structures aiming at dispersion optimization, too. [A.3]

4.2 Large Negative Dispersion Fiber

In this section, a PCF is designed by placing the airholes close to the fiber center without the inclusion of a doped region, which makes the fabrication easier. The goal is not to present a PCF structure with a novel geometry, but to investigate new limits in designing a hexagonal PCF as a dispersion compensator for NDSFs. A suitable design technique is chosen to find the largest negative dispersion parameter in a dispersion compensating photonic crystal fiber with hexagonal geometry, while keeping a wide operating bandwidth as well as a low confinement loss.

The designed structural parameters for the proposed DC-PCF to be used for dispersion compensation as broad as possible are found as: airhole diameter of the innermost ring $d_1 = 0.66$ μm, of the second and the third rings $d_{2,3} = 0.84$ μm, of the remaining rings $d = 2.3$ μm, and hole-to-hole spacing $\Lambda = 1$ μm between d_1 and $d_{2,3}$. The cross-section of the PCF is shown in Fig. 4.5.

To obtain almost negligible confinement loss and to minimize the number of airholes for easier fabrication, two rings with airhole diameter d and with hole-to-hole spacing $2 \cdot \Lambda$ are used instead of four additional rings with airhole diameter $d_{2,3}$. Since large air-filling fraction d/Λ is required to remain confinement loss below the Rayley scattering, the single-mode condition, $d/\Lambda <\sim 0.4$, is not satisfied in the PCF and not only the fundamental mode can propagate [95]. In particular, the use of small airholes surrounded by larger airholes is responsible for the multi-mode guidance in the small-hole region. Since the considered fiber length is about hundreds of meters, the higher-order modes may not be further investigated owing to their confinement loss higher than 2 db$\cdot$m^{-1}, and therefore the proposed fiber is effectively single-mode.

The simulation model that is used to fix these geometrical parameters has been verified by the convergence test. The reasonably accurate results can be obtained for the proposed DC-PCF by the simulation model presented in Appx. B. Two of the convergence tests applied, the test of the mesh size and the test of the number of PLM layers, are shown in Fig. B.2, Appx. B.

It can be seen in Fig. B.2 that for $M_x = 400$, which is equivalent to the mesh size $dx = 0.05$ μm, the results difference $\Delta\sigma$ is less than $1 \cdot 10^{-5}$ and the estimated error $\Delta\sigma_N$ is extremely low. For this and finer mesh, the results difference becomes flat and only slightly differs from the zero value.

Although it is sufficient to control three geometrical parameters to obtain the desired chromatic dispersion. The requirements are to minimize the number of the design parameters; it facilitates the design process. The achieved chromatic dispersion parameter for the

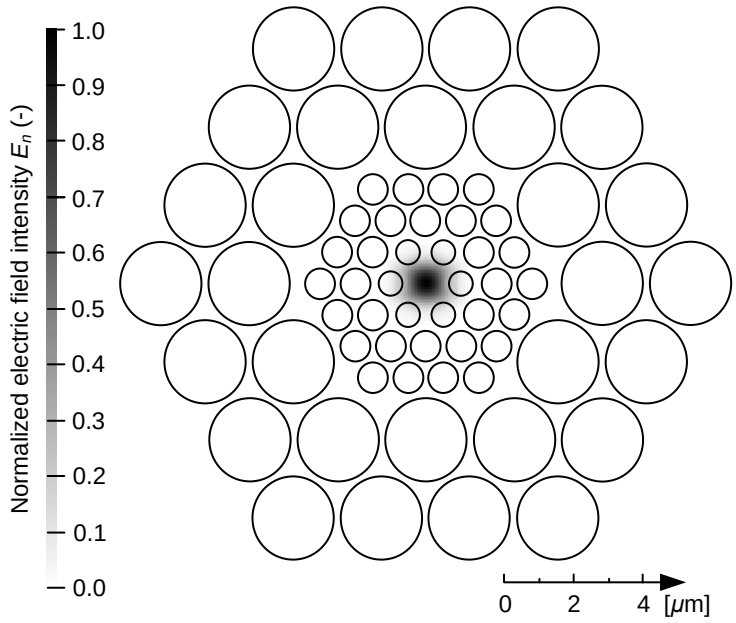

Figure 4.5: Designed fiber structure with the fundamental mode distribution for 1550 nm.

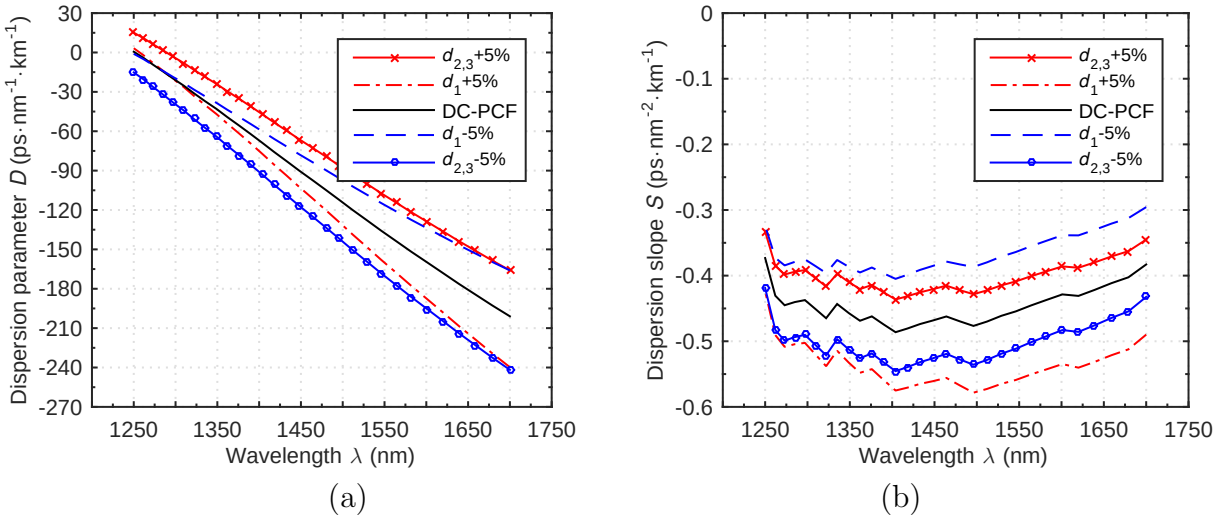

Figure 4.6: Dispersion parameter as a function of wavelength (a) and dispersion slope as a function of wavelength (b) for varied airhole diameter d_1 and $d_{2,3}$.

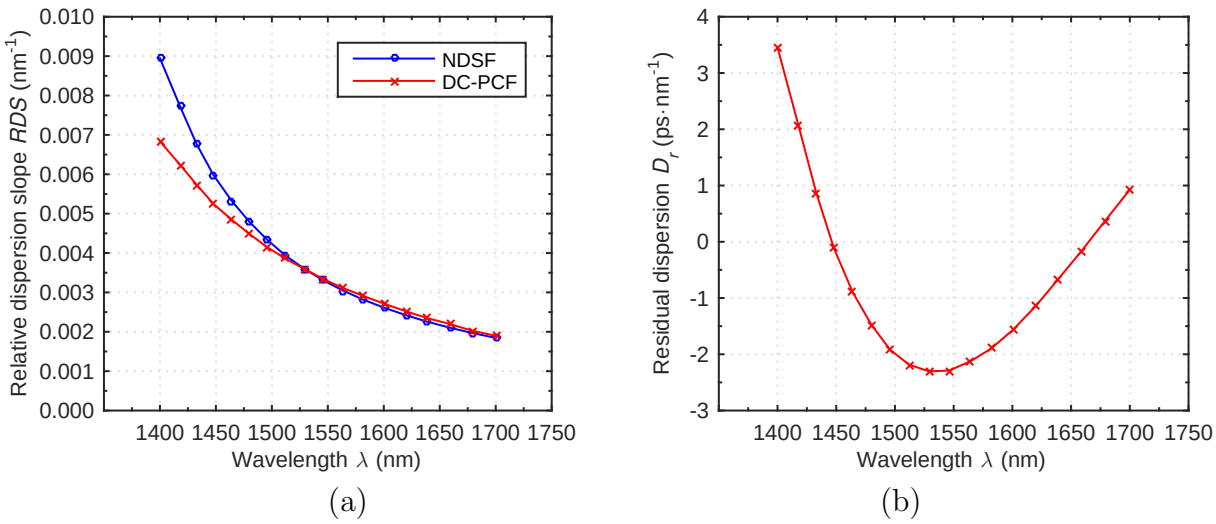

Figure 4.7: Relative dispersion slope of NDSF and designed DC-PCF (a) and residual dispersion after the dispersion compensation of NDSF by 1 km long DC-PCF (b).

fundamental mode is negative from the wavelength of 1273 nm as depicted in Fig. 4.6(a), and the relative dispersion slope is in an agreement with that of NDSF over the spectral range of 1470 to 1700 nm. The range is one of the broadest ever reported and much higher than in Refs.: 20, 22, 23, 24, 25, 26, 27, 28, 46, A.7. In Ref. 29 four design parameters are used to design a PCF with the suitable dispersion slope in the spectral range broader than 300 nm. In addition, the chromatic dispersion is about two times less than the one that is exhibited for the fiber with the structure depicted in Fig. 4.5.

The wavelength dependence of the RDS for both: NDSF and DC-PCF is shown in Fig. 4.7(a). The negative chromatic dispersion parameter in 1 km long DC-PCF allows to compensate dispersion in a 7.8 km long NDSF with the residual dispersion varying from -2.3 to 3.5 ps·nm^{-1} over the range of 1410 to 1700 nm, as shown in Fig. 4.7(b). By proper setting d_1 and $d_{2,3}$ parameters it is possible to match the relative dispersion slope of NDSF in other wavelength bands, while keeping the bandwidth broader than 200 nm. The author focuses on finding the results for the central wavelength of 1550 nm, broadly used in telecommunications.

In order to show how chromatic dispersion is affected by the structural parameters, the chromatic dispersion and the dispersion slope wavelength dependence is depicted in Fig. 4.6(a) and Fig. 4.6(b), respectively, where d_1 and $d_{2,3}$ are varied and Λ fixed. From Fig. 4.6(b) it can be written that the dispersion slope is affected mainly by the airhole diameter of the innermost ring. Airhole diameter $d_{2,3}$ has also the influence on dispersion slope, as depicted in Fig. 4.6(b). The desired slope around 1550 nm is found by proper setting both d_1 and $d_{2,3}$. The influence of each structural parameter on chromatic dispersion is described in more details in Chap. 3. Scaling the structure down decreases the dispersion

parameter to be lower at all the wavelengths. In a fiber drawing process, it is difficult to achieve diameters precisely and some deviation usually occurs. Since the chromatic dispersion is the most sensitive to deviation of the three innermost rings, the effect of 1%, 2% and 5% variation of d_1 and $d_{2,3}$ is investigated on the fiber performance.

If d_1 and $d_{2,3}$ is changed by ± 1 % (it is the estimated deviation to occur during the potential fabrication), the residual dispersion is numerically found to be between -12 and 18 ps·nm^{-1} by using the 1 km long DC-PCF within the considered range. The chromatic dispersion can remain unbalanced from -26 to 34 ps·nm^{-1} for 2% variation of the parameters and from -63 to 90 ps·nm^{-1} for 5%. The dispersion deviation caused by imperfection during the fabrication ought to be larger at longer wavelengths, due to the differences in mode confinement for different wavelengths.

In spite of the fact that the relative dispersion slope is in agreement over the large range of operating wavelengths with the relative dispersion slope of standard SMFs, the negative dispersion parameter is not higher than that in commercially available dispersion compensating fibers. Therefore the structural parameters are optimized to increase the confinement of the fundamental mode in the core, which, in fact, leads to smaller effective mode area and lower chromatic dispersion. However, if the effective mode area is extremely small and the mode is not confined enough in the core by cladding airholes, electric and magnetic fields extend outside the core into the cladding and modes become too leaky. Since the waveguide dispersion is dependent on the mode confinement, the minimal value of the chromatic dispersion parameter is limited by the allowable area of the effective mode.

The airholes are proposed to be closer to the fiber center by changing hole-to-hole spacing Λ from 1 μm to 0.85 μm and the innermost airholes are enlarged to the maximum value $d_1 = 0.83$ μm. The diameter cannot be enlarged more because of the confinement loss, which significantly grows if the innermost airholes are made larger. The confinement loss is about 10 times higher if d_1 is enlarged by 5%. In fact, the core diameter is comparable to length of the wave and the mode cannot be confined enough in the core and extends outside to the cladding resulting in the outer defect mode, which propagates through the airholes with diameter $d_{2,3} = 0.7$ μm, but with high confinement loss. It can be observed especially at longer wavelengths, where the confinement loss wavelength function is exponential. Coupling between the fundamental and the defected mode occurs if and only if the phase and loss matching conditions are met concurrently. Near the phase matching wavelength, the propagation characteristics of the one mode transfer to the other mode and the minimal value of the chromatic dispersion parameter is found at this wavelength. The phase matching wavelength can be set by adjusting d_1 and $d_{2,3}$ parameters. In the fiber design, it has been found through the numerical simulations that by changing $d_{2,3}$ the desired dispersion slope around 1550 nm can be set, whereas d_1 should be fixed for obtaining the minimal value of the chromatic dispersion parameter. Thus, fixing d_1 (minimal value of the chromatic dispersion is obtained) and varying $d_{2,3}$ parameter, the suitable dispersion slope can be set. It should be noticed that Λ is the same as for the near zero design presented in Sec. 4.1, but the modified DC-PCF exhibits much higher confinement loss. This is because of larger airhole diameters of the innermost ring and furthermore the doped region, in which the FM can propagate, is missing.

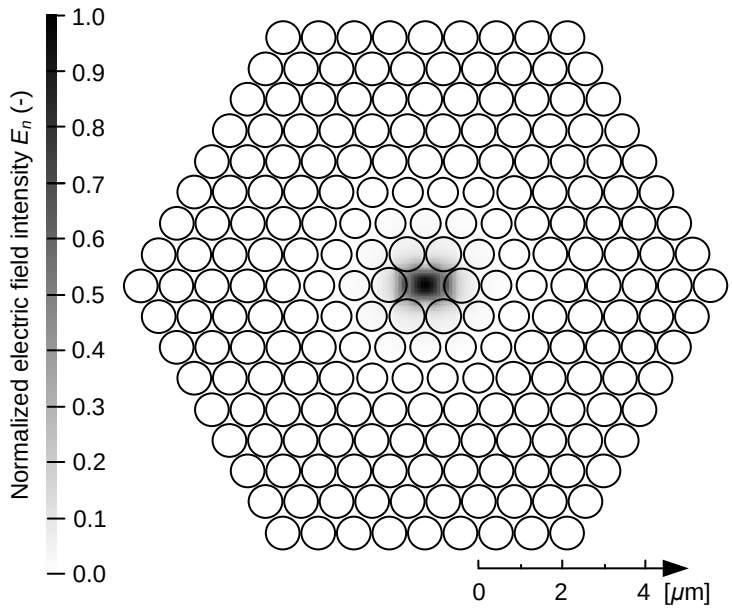

Figure 4.8: Modified fiber structure with the fundamental mode distribution for 1550 nm.

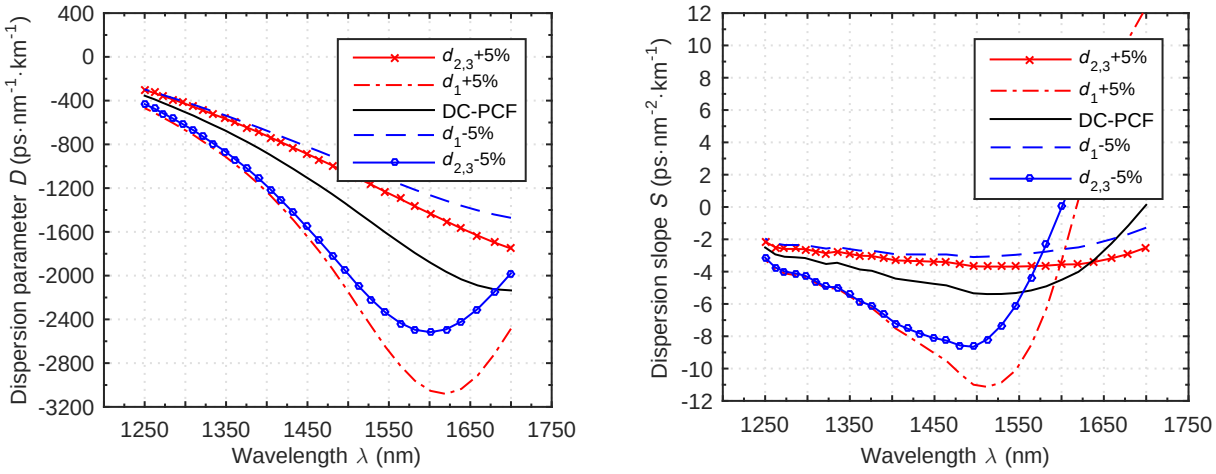

(a) (b)

Figure 4.9: Dispersion parameter as a function of wavelength (a) and dispersion slope as a function of wavelength (b) for varied airhole diameter d_1 and $d_{2,3}$.

Since using two outer rings of airholes in Fig. 4.5 is not sufficient to keep confinement loss below 1 dB·m^{-1} at 1550 nm, the modified structure has five outer airhole rings with diameter $d = 0.8$ μm. Also the higher-order modes exhibit lower confinement loss than the fundamental mode in this case. The modified structure of the designed DC-PCF is shown in Fig. 4.8. Since the airholes are close to the fiber center as well as due to the outer defect mode, which is propagated through the airholes with diameter $d_{2,3}$, the large negative dispersion parameter is more less -1600 ps·nm^{-1}·km^{-1} at the wavelength of 1550 nm in the modified DC-PCF. This is the limit value of the design. The author predicts that the negative dispersion parameter cannot be further minimized in the small effective mode area photonic crystal fibers, while keeping the operating bandwidth larger than 120 nm and low confinement loss. It should be noticed that it is redundant to tune the diameters on three or more decimal places to achieve lower dispersion parameter, because the effect is comparable to the small numerical error that the simulation model exhibits.

The simulation model has been updated based on the structure in Fig. 4.8. The size of the computing cell in x and y direction, respectively, and the mesh size dx are the updated parameters. The convergence tests are shown in Appx. B in Fig. B.3.

The lower diameter $d_{2,3}$ facilitates the outer mode enlargement and the both modes are matched at shorter wavelengths. The wavelength dependence of chromatic dispersion for the variation of its structural parameters is shown in Fig. 4.9(a). The change in diameter, which allows extending the mode to the outer core (increasing d_1, decreasing $d_{2,3}$) causes more significant dispersion changes. In modified DC-PCF it is undesirable to achieve phase matching wavelength close to the 1550 nm for the high confinement loss. The dispersion parameter grows upon the phase matching wavelength due to the more energy, which is in the outer defect mode than in the fundamental mode. The light waves upon the phase matching wavelength are unsuitable for dispersion compensation owing to the opposite dispersion slope and high confinement loss exceeding few dB·cm^{-1}. The calculated confinement loss of the modified structure is about 0.05 dB·km^{-1} and 128.6 dB·km^{-1} at 1550 nm and 1700 nm, respectively.

The length of the modified fiber can be more than ten times shorter than in the case of the fiber with the structure shown in Fig. 4.5. On the other hand, the relative dispersion slope matches the RDS of NDSF in approximately three times shorter wavelength range. The RDS for the modified fiber structure is shown in Fig. 4.10(a).

The residual dispersion is about ± 6 ps·nm^{-1} from 1496 to 1615 nm, if the dispersion in 90.8 km NDSF is compensated by the 1-km long modified DC-PCF, as depicted in Fig. 4.10(b). Thus, the length of the modified fiber can be more than ten times shorter, while the residual dispersion is doubled in contrast to the fiber, of which cross-section is shown in Fig. 4.5. However, for broader range of wavelengths the residual dispersion is much higher, for example at 1700 nm, the residual dispersion is about -200 ps·nm^{-1}. The modified DC-PCF is the most vulnerable if d_1 is made larger and $d_{2,3}$ smaller leading to the shorter wavelength of the phase matching that results in the higher influence of the outer defect mode.

The modified fiber is less immune to deviations originated during the potential fabrication process. The 2% deviation in diameter d_1 and $d_{2,3}$ increases the residual chromatic

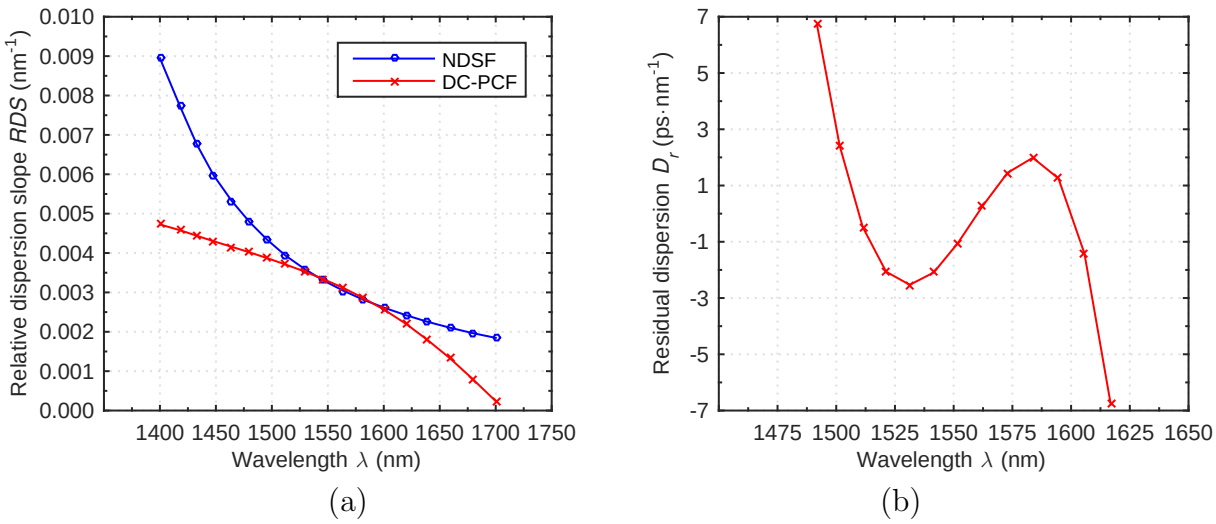

Figure 4.10: Relative dispersion slope of NDSF and designed DC-PCF (a) and residual dispersion after the dispersion compensation of NDSF by 1 km long modified DC-PCF (b).

dispersion up to 105 ps·nm^{-1} considering 1 km long compensating fiber and the assumed bandwidth.

Both DC-PCFs have similar small effective mode area being 1.92 μm^2 and 1.87 μm^2, respectively (at 1550 nm). It is therefore, the modified fiber has the outer core, where the outer defect mode is propagated. It is worth mentioning that the difference between the mode areas of the NDSF and the compensating fibers is high and the splice loss is significant. The splice loss of the both proposed fibers is 15.3 ± 0.5 dB over the considered range and increases as wavelength decreases, due to the mode area, which is smaller at the waves with longer wavelengths. The splice losses are not considered in the fiber designs, because there are technology processes that allow their reduction to the negligible level. The splice loss can be significantly reduced for example by tapering and fattening [110]. Such small mode area fibers are also highly nonlinear, therefore an attention should be paid to telecommunication links, where channel spacing, power of lasers, and residual chromatic dispersion should be set to reduce nonlinear effects. This doctoral thesis is focused on the fiber design and the influence of such a high nonlinearity on the telecommunication link is not investigated. The designed fibers have much smaller effective mode areas than photonic crystal fibers introduced in Chap. 2 except one in Ref. 23. On the other hand, the designed fibers have unique dispersion properties, not achievable in the previously published papers. [A.2]

4.2.1 Summary

In this section, the fiber structural parameters have been verified from the perspective of the dispersion limitations in the design of the small effective mode area photonic crystal

fiber.

The main contribution of the section is the proposed fiber with one of the best matching of the relative dispersion slope as the referred to the standard fiber to be compensated. Beyond this, the fiber has been modified to find the tradeoff between the minimal value of the chromatic dispersion parameter and the operating bandwidth. It has been confirmed through the numerical simulations that the chromatic dispersion parameter cannot be further reduced, below -1600 ps·nm^{-1}·km^{-1} at 1550 nm, while keeping the high operating bandwidth, and low confinement loss. The structure contains small amount of airholes compared to other designs. Further, three different design parameters are used, which can ease a potential fabrication. The achieved results cannot be found in similar paper on this topic.

The designed fibers are sensitive to deviations caused during the potential fabrication and diameters of the innermost airholes should be maintained within the 1% tolerance. The mechanisms of the control of chromatic dispersion in the proposed fibers are described in details. In a similar way, the desired chromatic dispersion wavelength dependence can be obtained to compensate dispersion in other single-mode fibers broadly used in telecommunication, among others. [A.2]

4.3 Narrowband Optical Fiber Filter

This section presents a novel design of a narrowband photonic crystal fiber filter based on the phase matching between the inner fundamental mode and leaky outer defect mode. The proposed dual-core PCF-based filter with the germanium dioxide doped region is designed by investigating the influences of the fiber geometry on filtering characteristics.

A structure under investigation is a conventional photonic crystal fiber with silica background, doped core and hexagonal cladding. PCFs have usually exponential leakage loss wavelength dependence, and their filtering possibilities are limited.

In the structure, germanium dioxide is preferred for doping, because, to the best of the author's knowledge, no efforts have been made to design a dual-core PCF filter with a doped core by GeO_2, although it is very promising in terms of transparency and manufacturability.

The fundamental mode within a pass-band is confined enough in the core by the innermost ring of airholes with large airhole diameter d_1. The significant coupling between the fundamental and outer defect mode can occur, if the inner core is similar size as the wavelength. The larger core fibers have usually high effective index difference between the inner and outer mode and the outer core feel negligible effect from the inner core. Generally speaking, the airholes should be close to the core and hole-to-hole spacing Λ should be lower than 2 μm taking into account 2 μm as the maximal wavelength that can be used in silica fibers, due to the absorption loss.

The outer core, where the defect mode is guided, can be formed by removing the airholes of selected rings or by reducing their diameters. The reduced diameters are more suitable, because these airholes confine the fundamental mode and keep the low loss within the pass-band with the minimal number of airhole rings. On the other hand, the airholes

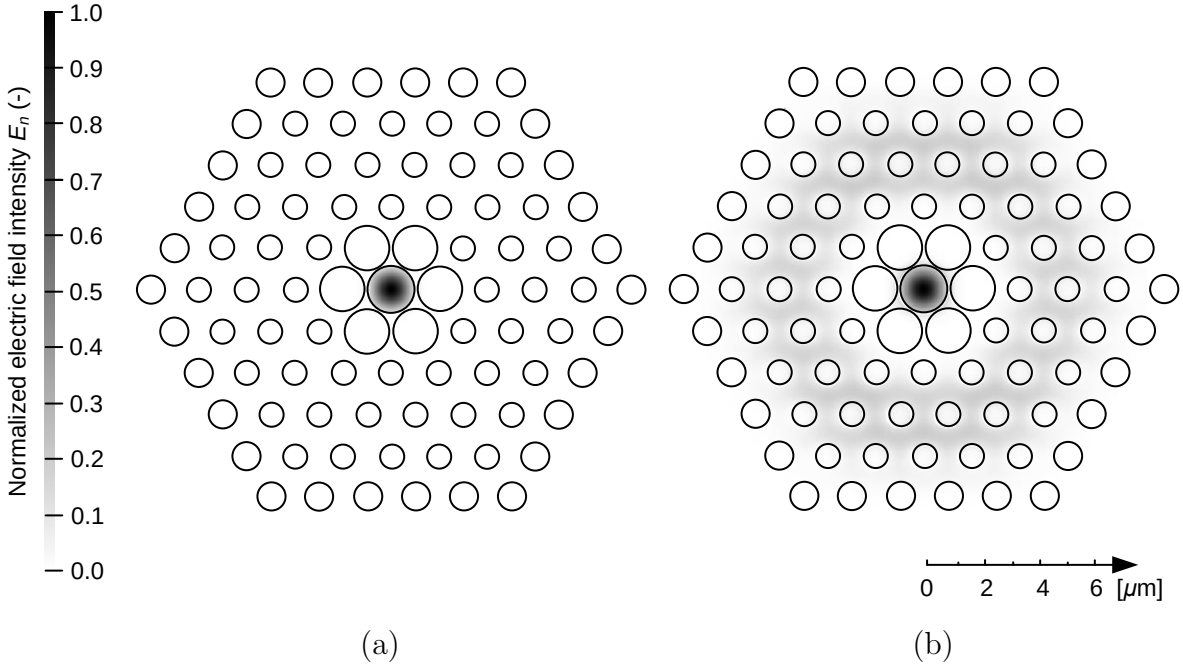

Figure 4.11: Proposed fiber structure with the normalized mode field distribution at the wavelength of 1 μm (a) and 1.55 μm (b) with strong coupling.

should be small enough to allow guidance of the outer defect mode.

Dual-core fibers for dispersion compensation contain frequently more additional airhole rings with proper size of airhole diameter to have adequate confinement of the both modes. However, to filter wavelengths, the outer defect mode remains leaky.

The designed fiber yields high chromatic dispersion at the wavelengths, where strong coupling occurs. In dual-core fibers the value of chromatic dispersion is of the order of thousands of ps·nm^{-1}·km^{-1}. Since the fiber length necessary for the wavelength filtering is one meter, maximal, the chromatic dispersion may not be calculated especially for its low value around the filter cut-offs. The wavelengths that suffer the most on high dispersion, are filtered.

The filter properties are investigated on the optimized fiber with the stop-band from 1.54 to 1.56 μm. In optimization, the hole-to-hole spacing has been verified to be $\Lambda = 1.75$ μm as the most suitable. The spacing is large enough to allow a fabrication, and concurrently, the sufficiently high coupling between the both modes occurs.

The suitable fiber structure that can be used as the filter has been predicted and its cross-section is shown in Fig. 4.11. To cover the large part of the core area by higher refractive index material, the diameter of the doped region d_r is fixed as $d_r = \Lambda = 1.75$ μm. Through the simulations, it has been confirmed that the minimal number of airhole rings should be $N = 5$. The obtained stop-band can be achieved by diameter of the innermost airholes $d_1 = 1.53$ μm, of the cladding airholes $d_2 = 0.9$ μm, and of the outermost airholes

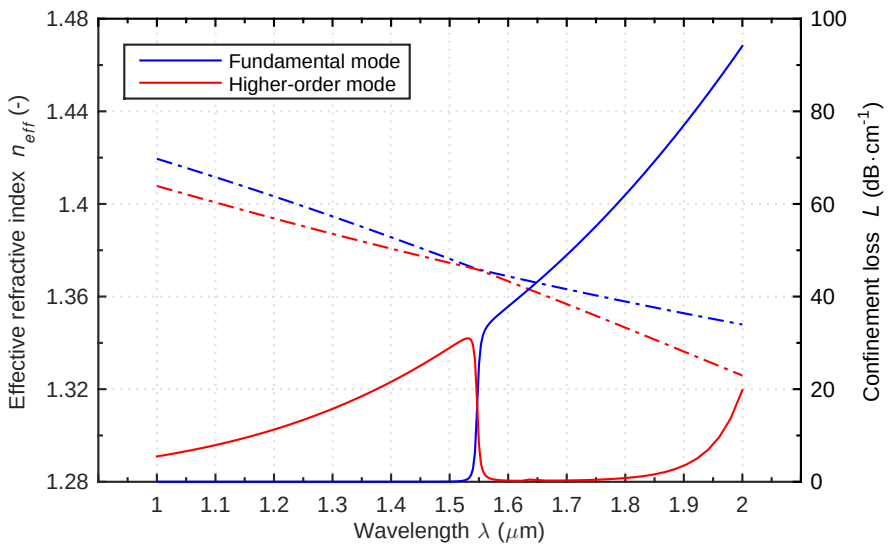

Figure 4.12: Effective refractive index (dash-dot line) and confinement loss (solid line) wavelength dependence of the designed fiber with stop-band near the wavelength of 1.55 μm. The fiber doped by GeO_2 is considered.

$d_3 = 1.05$ μm. The one of the contributions of this structure is that the geometrical parameters are as large as possible. Only one parameter, cladding airholes diameter d_2, is less than 1 μm. This makes fabrication as simple as possible. For example, most of the photonic crystal fibers presented in the state of the art have airhole diameters much smaller. The final simulation parameters are summarized and their correct setting is verified in Appx. B.

As for the designed filter, the fundamental mode is guided in the outer core upon the phase matching wavelength, but the sufficiently large amount of energy remains in the inner core, where the higher-order mode is guided. This mechanism is on the contrary to the mechanisms of the conventional dual-core PCF; the field of the inner mode transfers to the outer core, where is confined and guided. The leakage loss of the designed fiber for the inner core mode are not higher than 0.1 dB·cm^{-1} up to the wavelength of 1.75 μm.

The loss of the inner core mode upon the phase matching wavelength is much higher than for the same mode below this wavelength. It is due to the energy transfer to the outer core. However, the remaining optical field is still high enough and the loss are much lower than for the fundamental mode guided in the outer core. This is the main idea of this paper that it is possible to keep sufficiently low loss upon the phase matching wavelength. The 10 cm long fiber can work as a stop-band filter with 1 dB maximal leakage loss in the longer wavelength pass-band.

The mode coupling within the narrow spectrum occurs due to the high mode confinement by the innermost airhole ring and by the doped core, concurrently. The high-index doped core significantly changes the effective index and strongly confines the inner mode

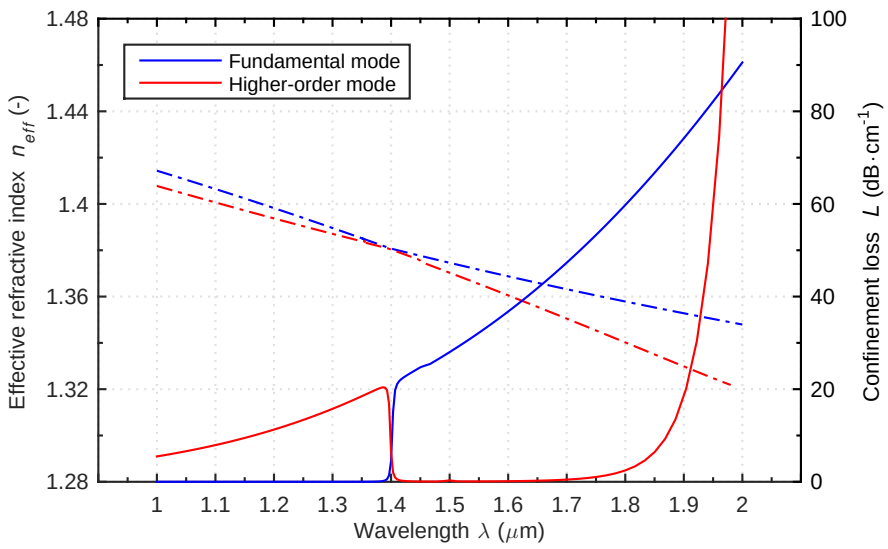

Figure 4.13: Effective refractive index (dash-dot line) and confinement loss (solid line) wavelength dependence of the designed fiber with stop-band near the wavelength of 1.4 μm. The nondoped fiber is considered.

in the core. The main difference between the designed dual-core PCF doped by germanium and the nondoped dual-core PCF can be observed comparing Fig. 4.12 and Fig. 4.13, respectively. If the designed fiber is doped, the refractive index of the inner core increases. The effective index difference is much higher for the shorter wavelengths than for the nondoped fiber, where the phase matching occurs at 1.4 μm and vice versa. It can be seen that the modes guided through the nondoped outer cores of the both fibers have nearly similar effective index. The inner core doping has the negligible effect on the effective index of the outer core.

The influence of size of GeO_2 doped region is depicted in Fig. 4.14(a). The fiber has low sensitivity on the GeO_2 core size. It can used to tune the desirable position of the stop-band, precisely. The 10% increasing of the size shifts the phase matching wavelength by 0.01 μm to the longer wavelengths. The filter full width at half maximum remains similar for the different sizes of the doped region. The larger doped region confines more the mode in the core, and therefore the confinement loss are lower at the pass-band. On the other hand, the negligible effect on the outer core mode can be observed.

Similarly, the outer core mode is affected by increasing or decreasing the innermost airholes, as depicted in Fig. 4.14(b). The larger innermost airholes shift the phase matching to the shorter wavelengths. It facilities the energy transfer from the inner to outer core for shorter wavelengths. The effective index difference is nearly zero at a narrower band of wavelengths which decreases the full width at half maximum. The fiber sensitivity on the size of the innermost airholes is high, their enlargement of 2.5 % changes the phase matching wavelength by 0.1 μm.

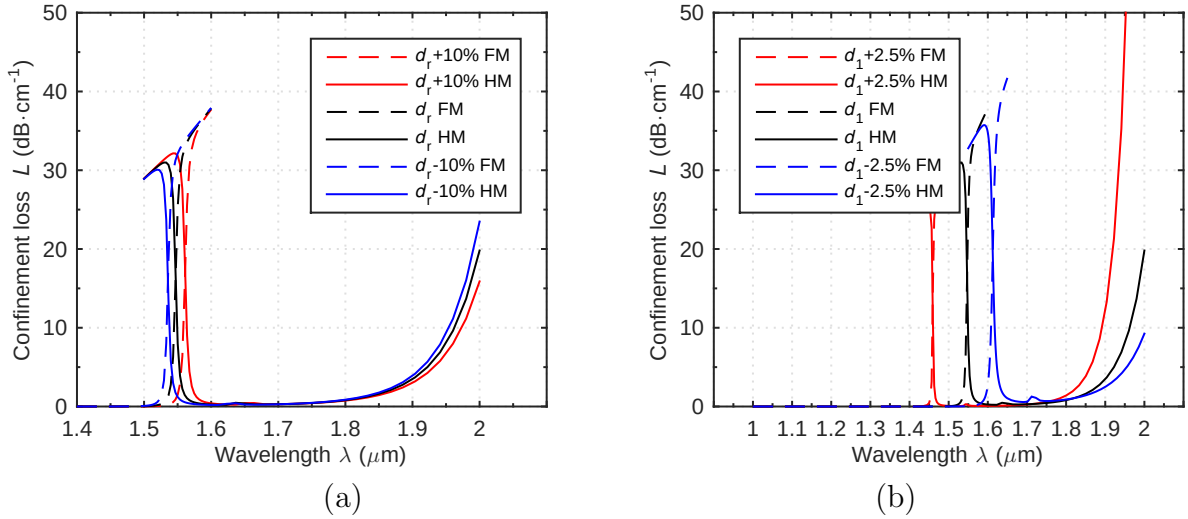

Figure 4.14: Confinement loss wavelength dependance, where GeO_2 core size d_r (a) and diameter of the innermost airholes d_1 (b) is an investigated parameter.

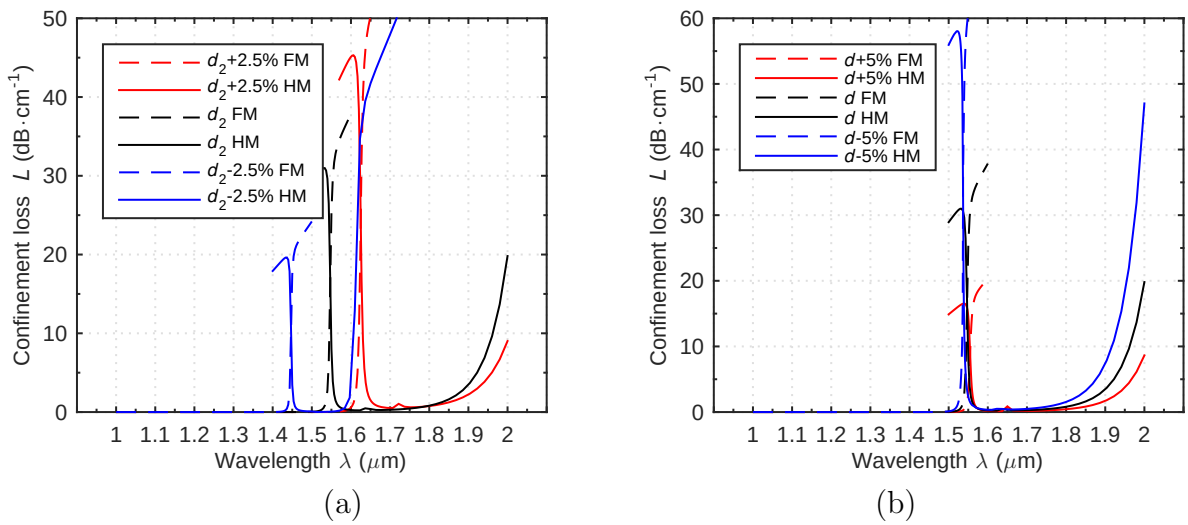

Figure 4.15: Confinement loss wavelength dependance, diameter d_2 (a) and diameter d_3 (b) is an investigated parameter.

The opposite shift of the phase matching wavelength is found for the 2.5% enlargement of cladding airhole diameter d_2, as shown in Fig. 4.15(a). The larger airholes confines the inner core mode more and the phase matching is observed for the longer wavelengths. However, the outer core mode is guided with higher confinement loss. The outer core mode cannot be propagated through the airholes and higher amount of the energy is reflected from them and leaks out.

The larger outermost airholes with diameter d_3 decrease confinement loss for the investigated spectrum. Therefore, if d_3 is properly set, sufficiently low loss for the pass-bands is ensured. Varying d_3 by 5 % has negligible effect on phase matching, as can be observed in Fig. 4.15(b), but the confinement loss is significantly affected.

The designed fiber has small effective mode area of the inner mode about 2.5 μm within the investigated spectrum. Conventional optical fibers have usually mode areas about 70 μm^2. The high difference between the mode areas can cause high splice loss, if for example the tapering and fattening is not employed. On the other hand, the designed filter can eliminate coupling problems of small effective mode area fibers, where one need to filter narrow spectrum of wavelengths. [A.11]

4.3.1 Summary

The proposed dual-core photonic crystal fiber-based filter with the germanium dioxide doped region is designed by investigating the influences of the fiber geometry on filtering characteristics. It has been found that the sufficiently high transparency of the pass-bands is set by the outermost airhole ring. On the other hand, by increasing the airhole diameter of the innermost ring, the phase matching wavelength experiences a shift to shorter wavelengths. The phase matching is similarly affected by the larger airhole diameter of the remaining airholes. These diameters are the most responsible for the confinement loss of the investigated spectrum.

Understanding the mechanisms, the fiber parameters have been optimized to obtain the stop-band from 1.54 to 1.56 μm with the confinement loss higher than 20 dB·cm^{-1}. On the other hand, the loss in the pass-band are kept well below 1 dB for the 10 cm long fiber. The coupling between the inner and outer core has been found in the narrowband of wavelengths. Such a property is due to the strong mode confinement caused by the sufficiently large diameter of the innermost airholes and by the presence of the doped region, concurrently.

The position of the stop-band is very sensitive to any geometrical deviations. The author predicts that the high sensitivity can be used to design a distributed fiber sensor. [A.11]

4.4 Large Mode Area Fiber

A symmetric large mode area leakage channel fiber reported in this section is designed to be reasonably bendable and to guide effectively single-mode from 2 to 9.5 μm. For this

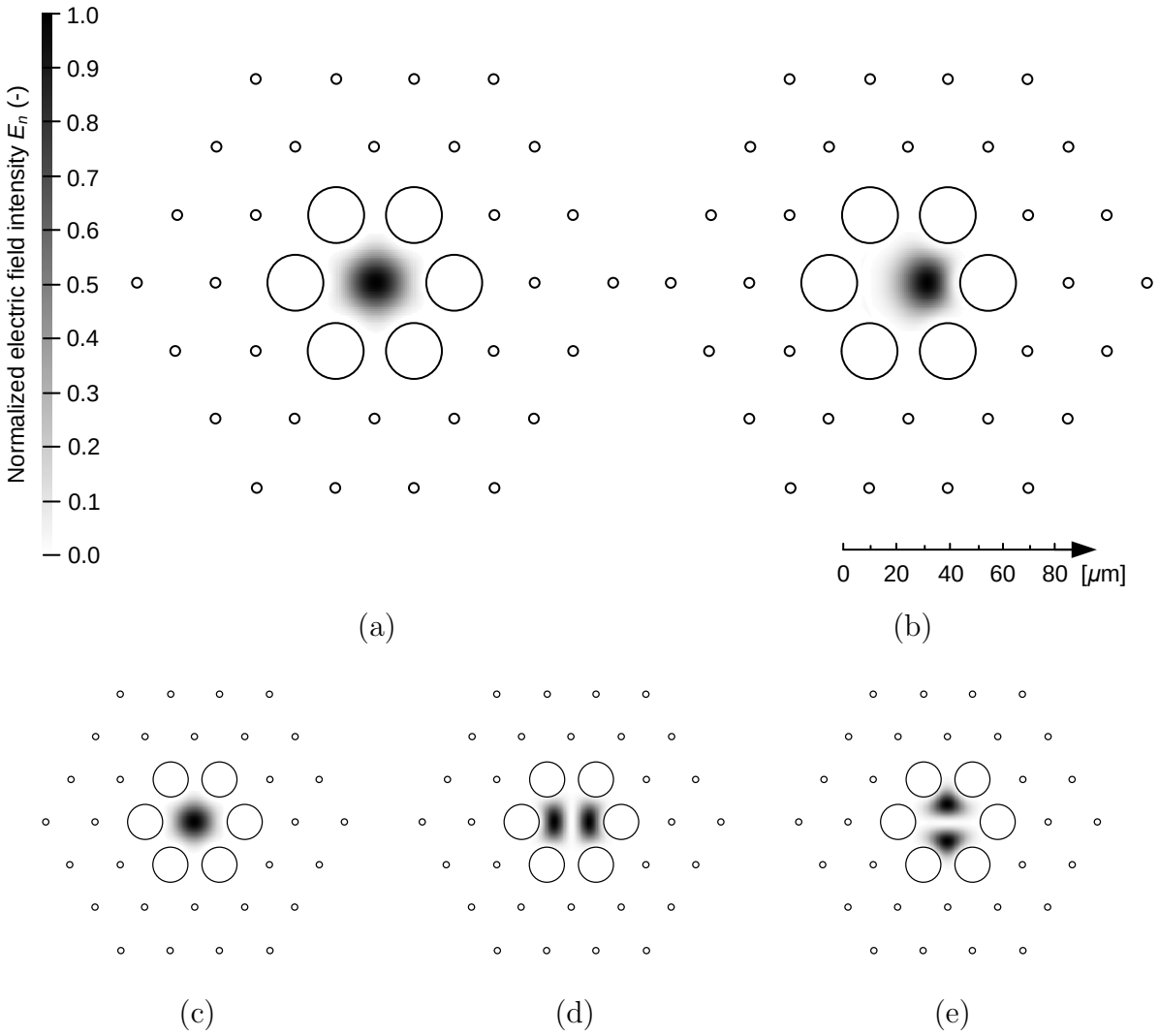

Figure 4.16: Fundamental mode field distribution inside the designed fiber with bending radius $r_b = \infty$ (a) and 20 cm (b). The fundamental (c), the second- (d) and the third- (e) order mode field distribution in the straight fiber.

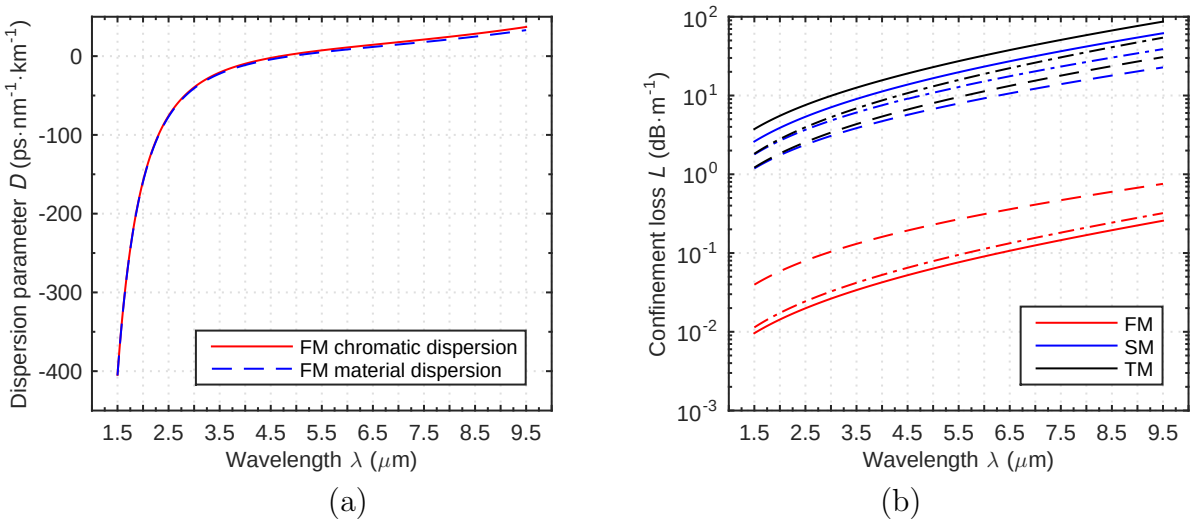

Figure 4.17: Dispersion parameter of the chromatic and material dispersion (a). Confinement loss as a function of the wavelength for the fundamental, the second- and the third-order mode, respectively (b). In (b), the number of the outer rings with diameter d is considered as a parameter. The solid line is for the 2 outer rings, the dash-dot line for the 1 outer ring and the dashed line for the structure having the only one ring with diameter d_1.

purpose, As_2S_3 chalcogenide glass transparent from 0.57 to 11.8 μm is used as the fiber background for its transparency and high nonlinearity. The mode properties obtained via the FDFD are used as an input for a numerical investigation of supercontinuum generation inside the designed fiber. The simulation is carried out with the parameters described and verified in Appx. B.

Let the author consider a conventional leakage channel fiber as an initial structure as the one presented in the study by L. Dong et al. [44]. The fiber consists of 6 airholes surrounding the fiber core. The fiber is effectively single-mode and bendable with negligible confinement loss that are kept for bending radius up to $r_b = 10$ cm.

Although the fiber operates well, a design goal is to improve the fiber modal properties. The author confirmed through the numerical simulations that the confinement for the straight and bent fiber can be significantly improved by adding two airholes rings with sufficiently small airhole diameter. Such a modified fiber structure is shown in Fig. 4.16, where hole-to-hole spacing $\Lambda = 35$ μm, airhole diameter of the inner ring $d_1 = 20.5$ μm and of the outer rings $d_2 = 4$ μm. Due to the large hole-to-hole spacing, the fiber effective mode area is as large as $A_{eff} \simeq 683$ μm^2 at the wavelength of 2 μm and increases for longer wavelengths. At the maximal wavelength of the considered band (9.5 μm) is A_{eff} equal to 741 μm^2. The material properties such as linear and nonlinear refractive index of As_2S_3 chalcogenide glass are taken from Ref. 111.

The waveguide dispersion is nearly zero and the material dispersion is roughly equal to

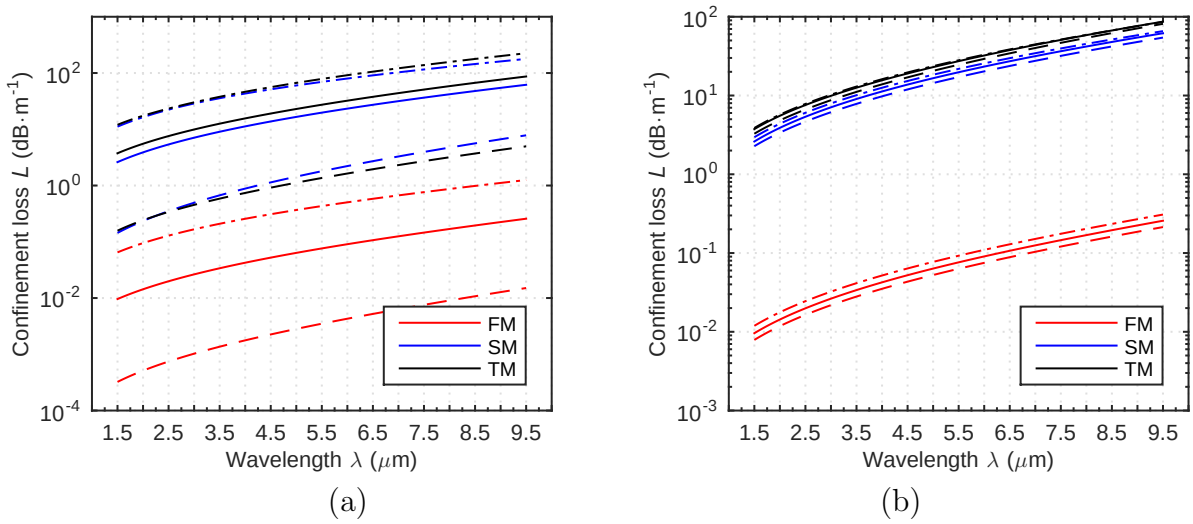

Figure 4.18: Confinement loss as a function of the wavelength for the fundamental, the second and the third-order mode, respectively. In (a), d_1 is considered as a parameter. The solid line represents the designed fiber with d_1, the dash-dot line is for $d_1 - 10$ % and the dashed line for $d_1 + 10$ %. In (b), d is considered as a parameter. The solid line represents the designed fiber with d, the dash-dot line is for $d - 10$ % and the dashed line for $d + 10$ %.

the chromatic dispersion, as depicted in Fig. 4.17(a). The zero dispersion wavelength of the fiber is about 4.7 μm and it can be tuned only within the narrow wavelength spectrum, while keeping the LMA and avoiding doping.

It can be seen in Fig. 4.17(b), the confinement loss of the FM decreases, if one or more rings with diameter d are placed around the fiber center, and moreover as an advantage, the confinement loss of the HMs increases. The effective single-modeness is improved. Since the loss difference between the structures with one and two rings with diameter d is not so significant, it is redundant to add another airhole ring and it can be stated that the number of the airhole rings is optimized.

Contrary to this mechanism, increased diameter d_1 reduces the confinement loss for both the FM and HMs, moreover the large difference is kept between the loss of the FM and HMs, Fig. 4.18(a). The aim is to set the loss of the FM by d_1 bellow the given level within the considered spectrum. Similarly, as expected, the confinement loss are reduced if diameter d is larger, Fig. 4.18(b). This works perfectly, the confinement losses decreases with the larger diameters. However, an attention should be paid, if the fiber is bent. In this case, diameter d should be sufficiently small in order to make the HMs leaky as much as possible.

Since the larger airhole dimensions allow for better control of the airholes during the fabrication process, it is a particular advantage of large mode area fibers, the airhole diameters are kept during the optimization to be at least 4 μm in diameter. Thus, in the first step, d is fixed to be 4 μm and after that d_1 is found by increasing or decreasing

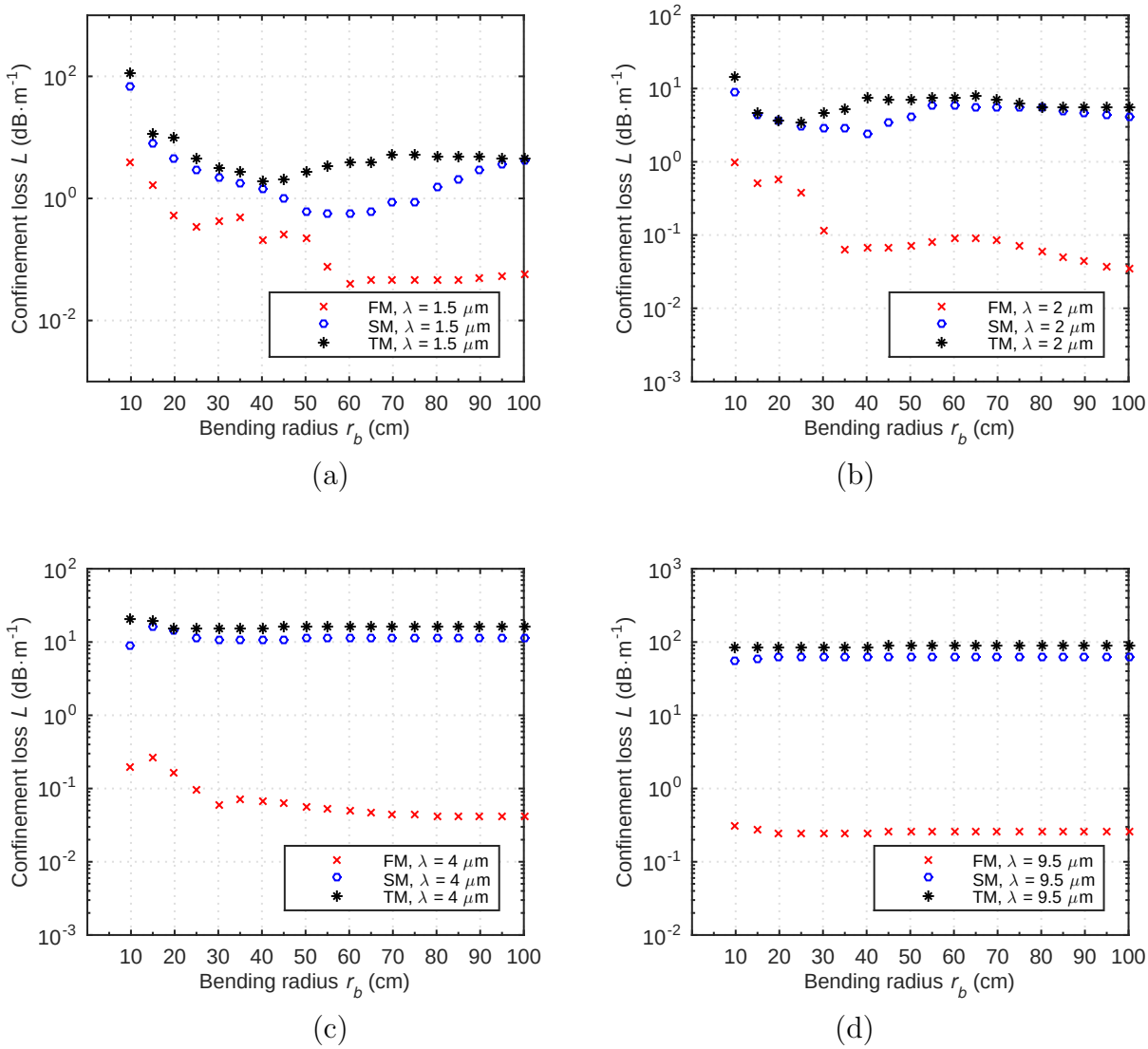

Figure 4.19: Confinement loss as a function of bending radius r_b for the fundamental, the second- and the third-order mode, respectively at the wavelengths of 1.5 μm (a), 2 μm (b), 4 μm (c) and 9.5 μm (d).

its diameter with regards to the confinement losses of the modes for the straight and bent fiber. However, a designer can found that is limited. In some cases there is no possibility of obtaining the desired losses by tuning d_1. This occurs if and only if the hole-to-hole spacing is too high causing that the HMs are strong especially for the bent fiber. Generally accepted view is that higher-order modes are always stronger for the larger cores. In particular, this occurs for shorter wavelengths. To optimize the fiber, the goal is to find maximal Λ for which the desired loss for the FM and HMs can be set by tuning d_1. For the considered fiber, the maximal hole-to-hole spacing is equal to 35 μm.

The effective mode area can be further enlarged, if d is decreased below this value. It allows increasing the hole-to-hole spacing and first airhole diameter that is desirable, because of the HMs being leaky enough, while the FM is well confined. However, the benefit of the larger mode area is strongly compensated by increased fabrication efforts.

The fiber is effectively single-mode in the spectral region from 1.5 to 9.5 μm, as shown in Fig. 4.17(b). The wavelength of 9.5 μm is the maximal that can be used, because of the limit given by confinement loss of the fundamental mode that is higher than 0.25 dB·m^{-1} at longer wavelengths. The maximal considered length of the designed fiber is 3 m. In such a case, the confinement loss is lower than 1 dB and lower than 1.5 dB for the bent fiber at $r_b = 10$ cm considering the wavelength of 9.5 μm It should be noticed that the material loss of chalcogenide fibers are usually higher than 1 dB·m^{-1} [56].

As shown in Fig. 4.19(a), the designed fiber is not effectively single-mode at the wavelength of 1.5 μm for the bending radius lower than 60 cm. The loss ratio between fundamental and second- or third-order mode is not high enough. For the wavelengths longer than 2 μm, the confinement loss of SM and TM are higher than 5 dB·m^{-1} for all the bending radius up to $r_b = 10$ cm, as can be seen in Fig. 4.19(b), (c), and (d). It can be stated that the loss value 5 dB·m^{-1} is high enough to guide light effectively single-mode.

4.4.1 Supercontinuum Generation

Supercontinuum generation is numerically investigated inside the designed fiber using the generalized nonlinear Schrodinger equation solved by split step Fourier method that is described in Sec. 3.4.1 considering the first $k = 1$–10 Taylor series coefficients β_k of phase constant $\beta(\omega)$. As shown in Fig. 4.17(a), the fiber chromatic dispersion is nearly similar to the material dispersion, especially at short wavelengths. Since the material dispersion can be obtained analytically by the second derivative of the Sellmeier equation, Appx. A, there is a possibility of varying the Sellmeier coefficients to find the Sellmeier equation for the effective refractive index associated with the chromatic dispersion.

In principle, this can be considered as an advantage, because $\frac{\partial^k \beta_0}{\partial \omega^k}$ is calculated as a derivative of the function and not as a derivative of the discrete-value vector, which is obtained through the FDFD. Thus, the discrete-value vector is approximated by the Sellmeier equation to reduce the noise during the calculation of the higher-order derivatives.

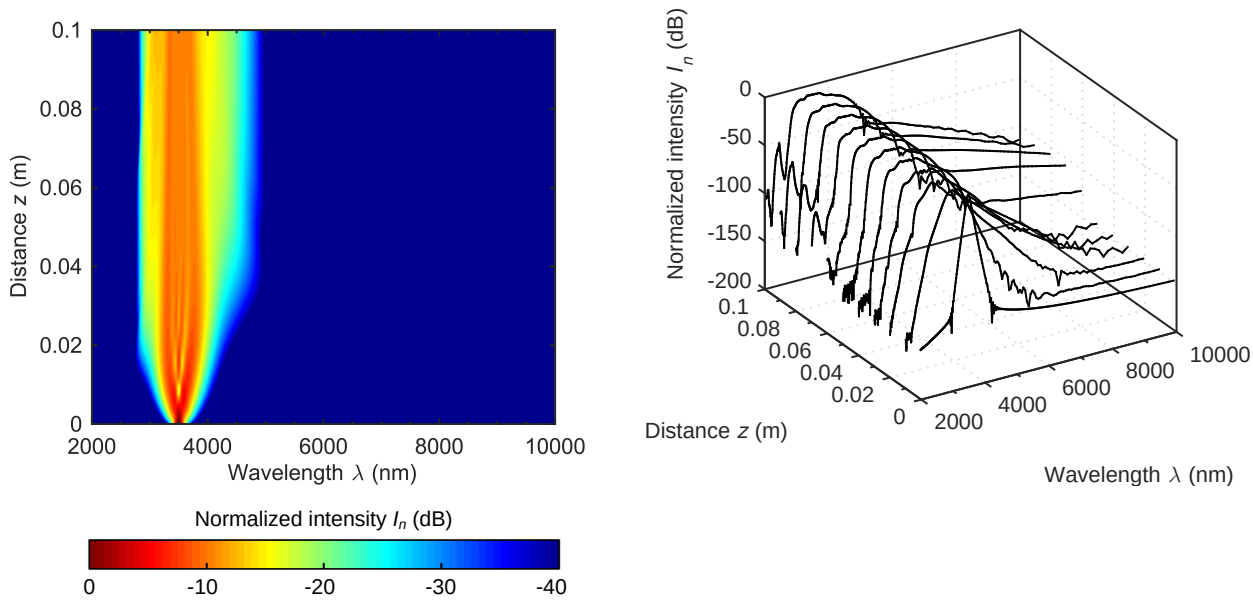

(a) (b)

Figure 4.20: Supercontinuum generation inside the LMA fiber pumped at 3.5 μm. It should be noticed that 40 dB scale is applied to all density plots.

The effective refractive index is approximated by Eq. (4.1):

$$n_{eff}^2(\lambda) = 1 + \frac{1.898368 \cdot \lambda^2}{\lambda^2 - 0.0225} + \frac{1.922298 \cdot \lambda^2}{\lambda^2 - 0.0625} + \frac{0.8765138 \cdot \lambda^2}{\lambda^2 - 0.1225} + \frac{0.118808 \cdot \lambda^2}{\lambda^2 - 0.1764} + \frac{0.977798 \cdot \lambda^2}{\lambda^2 - 641.6342}. \tag{4.1}$$

It should be noticed that Eq. (4.1) is valid only for the designed fiber with the structure presented in Fig. 4.16.

Nonlinear coefficient $\gamma = 0.0088$ W^{-1}·m^{-1} is obtained from Eq. (3.16), where nonlinear refractive index n_2 is $4.8 \cdot 10^{-18}$ W^2·m^{-1} and effective mode area A_{eff} is $697 \cdot 10^{-12}$ m^2 for pump wavelength λ_0 of $4.9 \cdot 10^{-6}$ m. As_2S_3 glass coefficients of the Raman response function, Eq. (3.29), are $f_R = 0.0031$, $\tau_1 = 15.2$ fs, and $\tau_2 = 230.5$ fs. The nonlinear coefficient can be further enhanced by decreasing the effective mode area or by using another background material with the higher nonlinear refractive index. For example n_2 of As_2Se_3 chalcogenide glass is about 7 times higher than that of As_2S_3 used in the fiber design.

The numerical model of the fiber is not related to the specific fiber manufacturer. Therefore, the fiber loss is not considered exactly in the SC simulation; it is considered to be 1 dB·m^{-1} at all wavelengths of the range. The value is equal to the minimal loss value, which can be achieved by the chalcogenide material. As compared with this value the confinement loss are negligible. Manufacturers use various technologies, materials and before the fabrication, the fiber loss should be modeled more precisely.

To generate supercontinuum, the soliton laser pulse with an envelope given from

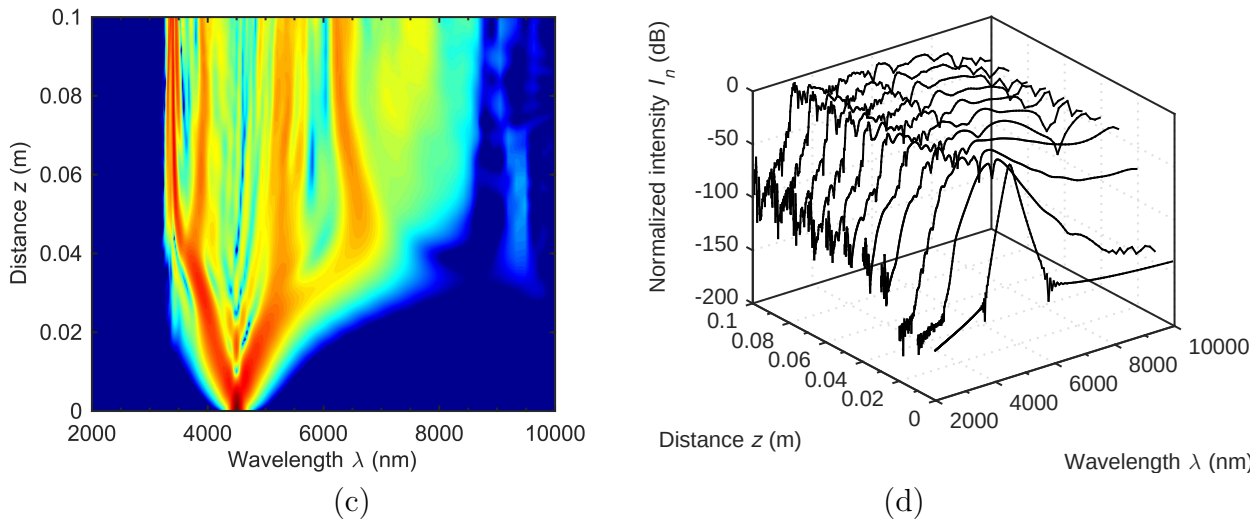

Figure 4.21: Supercontinuum generation inside the LMA fiber pumped at 4.5 μm.

Eq. (3.31) of width $T_0 = 100$ fs and peak power $P_0 = 50$ kW is considered to be injected inside the 10 cm long designed fiber segment. It should be noticed that these parameters are fixed throughout simulations in the both dispersion regimes. The variation of SC is investigated for different pump wavelengths in Figs. 4.20, 4.21, 4.22, and 4.23.

In Fig. 4.20, the supercontinuum is depicted for the normal dispersion pumping regime at the wavelength of 3.5 μm, which is far from the ZDW. The SC generation as narrow as 1.923 μm (from 2.824 to 4.747 μm) is dominated by self-phase modulation that can be observed as nearly symmetrical pulse broadening.

Increasing pump wavelength λ_0 to 4.5 μm close to the ZDW, but still lying in the normal dispersion pumping regime, the SC generation in Fig. 4.21 is initiated by SPM. With further propagation, the light passes the ZDW into the anomalous dispersion regime, where initiates soliton dynamics and consequently the soliton fission. Combining with Raman amplification, increased spectral broadening in the long wavelength side is resulted. The generated SC spans from 3.272 to 8.658 μm that is about 2.8 times broader than for pumping the fiber far from the ZDW in the normal dispersion regime.

As shown in Fig. 4.22, pumping the fiber in the anomalous dispersion regime at the wavelength of 4.9 μm near the ZDW, SPM initiates the pulse broadening, before the fission of the higher-order soliton occurs at $l_{fiss} \simeq 0.026$ m. Although the soliton of order $m \simeq 11.5$ is broken up through the fission, the only one soliton (red shifted by Raman amplification) is apparent in the spectrum. Remaining solitons are concentrated around the pump wavelength creating a relatively uniform spectrum. Generally speaking, the local value of β_2 is low near the ZDW, so distance ($\sim 5 \cdot l_D \simeq 1.5$ m) at which the solitons begin to separate is much longer with respect to the fiber length [60].

Dispersive wave generation and cross-phase modulation are expected to occur between the solitons and normal dispersion wavelength components, but they are difficult to isolate

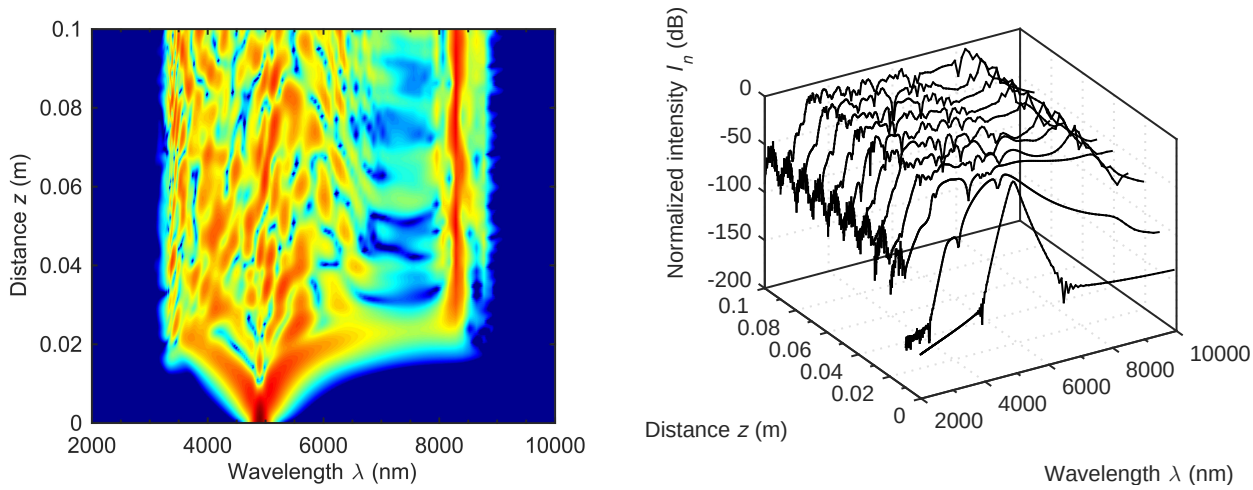

(a) (b)

Figure 4.22: Supercontinuum generation inside the LMA fiber pumped at 4.9 μm.

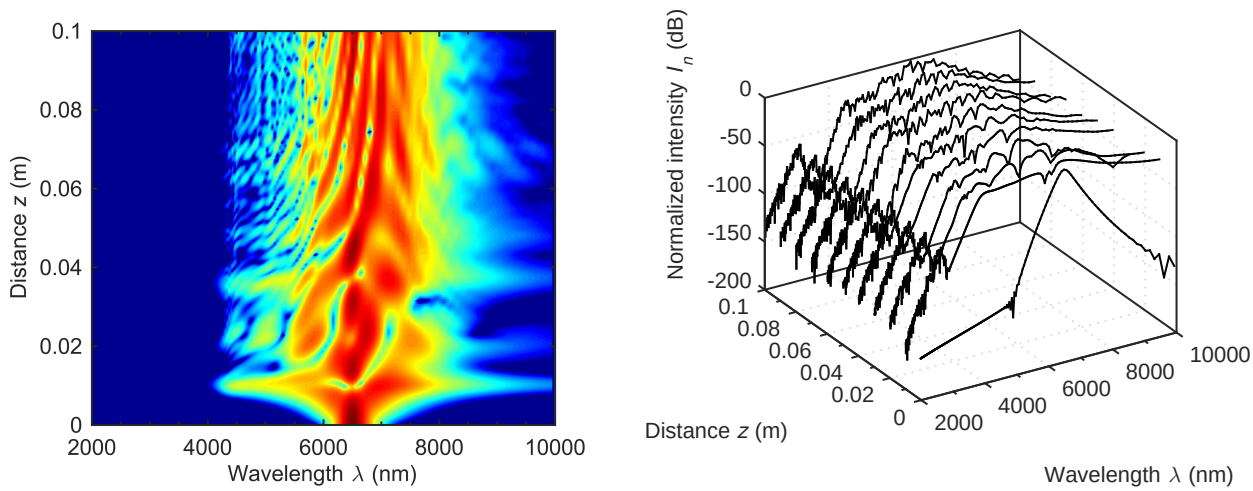

(a) (b)

Figure 4.23: Supercontinuum generation inside the LMA fiber pumped at 6.5 μm.

in the spectrum. However, a low power dispersive wave at the wavelength of 2.26 μm can be observed in Fig. 4.22(b). At the end of the fiber segment, the generated supercontinuum yields -20 dB bandwidth within the spectral range from 3.270 to 8.9 μm.

Spectral evolution of the SC is illustrated in Fig. 4.23 by pumping the fiber at 6.5 μm in the anomalous dispersion regime located far from the ZDW. The SC evolution is governed by soliton dynamics, in which propagating soliton of order $m \simeq 3.043$ is temporally compressed and spectrally broadened. At fission length $l_{fiss} \simeq 0.0091$ m, the soliton is perturbed into the 3 fundamental solitons responsible for the spectral broadening. Since local value of $\beta_2 \simeq -359.4$ ps$^2 \cdot$ km^{-1} is high, soliton separation distance ($\sim 5 \cdot l_D \simeq 0.139$ m) is of a similar size as the investigated fiber segment and all ejected solitons through the fission that experience a shift to the long-wavelength side can be observed in the spectrum.

A dispersive wave is generated at the wavelength of 3.087 μm, but its peak power is extremely low. The supercontinuum spectrum spans from 5.539 to 8.3 μm if the -20 dB bandwidth is considered.

In the next set of simulations with varying pulse duration T_0, the pump wavelength and peak power are kept fixed at $\lambda_0 = 4.9$ μm and $P_0 = 50$ kW, respectively. The shorter pulse duration is associated with lower soliton order m, shorter fission length l_{fiss} and quadratically shorter soliton separation length ($\sim 5 \cdot l_D$). The differences in the soliton order and fission length are apparent interpreting the results for the pumping by pulses with duration $T_0 = 50$ fs and $T_0 = 200$ fs shown in Figs. 4.24 and 4.25, respectively. More specifically, 50 fs pulse pumping is related to: $m \simeq 5.747$, $l_{fiss} \simeq 0.013$ m and $\sim 5 \cdot l_D \simeq 0.374$ m, whereas for 200 fs pulses to: $m \simeq 22.989$, $l_{fiss} \simeq 0.0521$ m and $\sim 5 \cdot l_D \simeq 5.985$ m.

One of the key differences between the Fig. 4.24 and Fig. 4.25 is the initial spectral propagation, where for 200 fs pumping the spectral broadening is significantly reduced and governed by different dynamics. In this case, not only SPM is responsible for the initial soliton evolution of 200 fs pulse, but also FWM and modulation instability [60]. These effects causes the fast modulation of the pulse envelope responsible for the soliton break up rather than soliton fission process, as can be seen in Fig. 4.25, where the soliton is broken up into the train of pulses earlier than at fission length $l_{fiss} \simeq 0.0521$ m. However, the soliton self-frequency shift and dispersive wave generation occurs also for the modulation instability induced break up as observed in Fig. 4.25. Thus, the dynamics for 50 fs, 100 fs, and 200 fs pulse pumping is similar as well as the achieved spectral bandwidth.

In the final set of simulations different pump peak powers are applied on the SC generation, whereas all other pulse parameters are fixed. The SC evolution for the pump pulse with peak power P_0 of 25 kW yields the soliton of order 8.128 that is broken up through the fission at 0.0368 m, as shown in Fig. 4.26. In Fig. 4.27, with the peak power increasing to 100 kW order m of the soliton increases to 16.256 and soliton fission length l_{fiss} decreases to 0.0184 m. Soliton separation length $\sim 5 \cdot l_D$ is independent on the peak power. As expected, the higher pulse peak power broaden the spectral evolution. For the 100 kW pulse peak pumping the SC is as broad as 5.955 μm from 3.217 to 9.172 μm. As well as for other simulations with pulse duration $T_0 \leq 100$ fs, the pulse broadening is initiated by self-phase modulation followed by soliton-related dynamics.

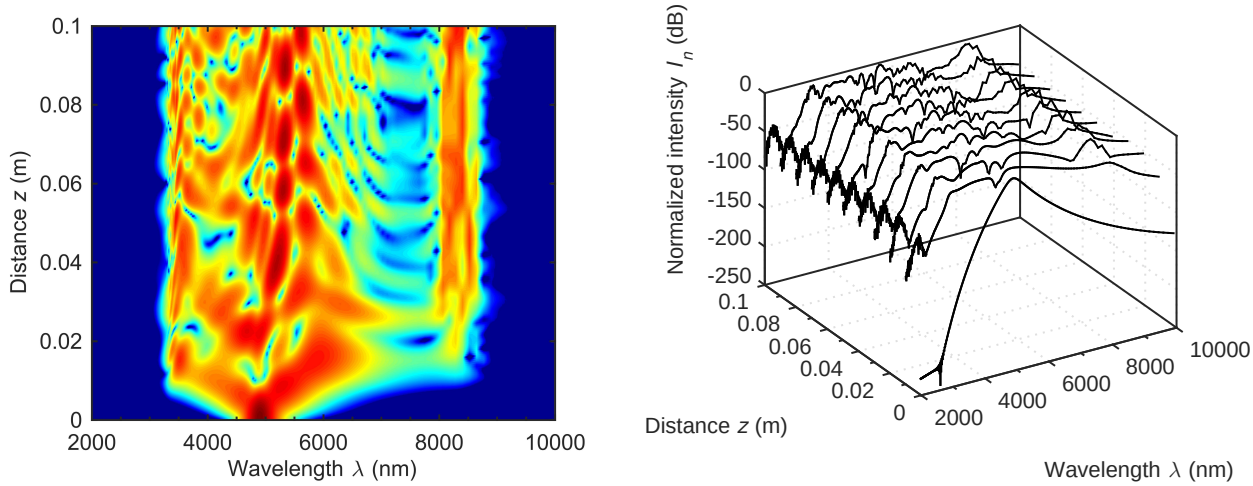

(a) (b)

Figure 4.24: Supercontinuum generation inside the LMA fiber, the pulse duration of the pump pulse is decreased to 50 fs.

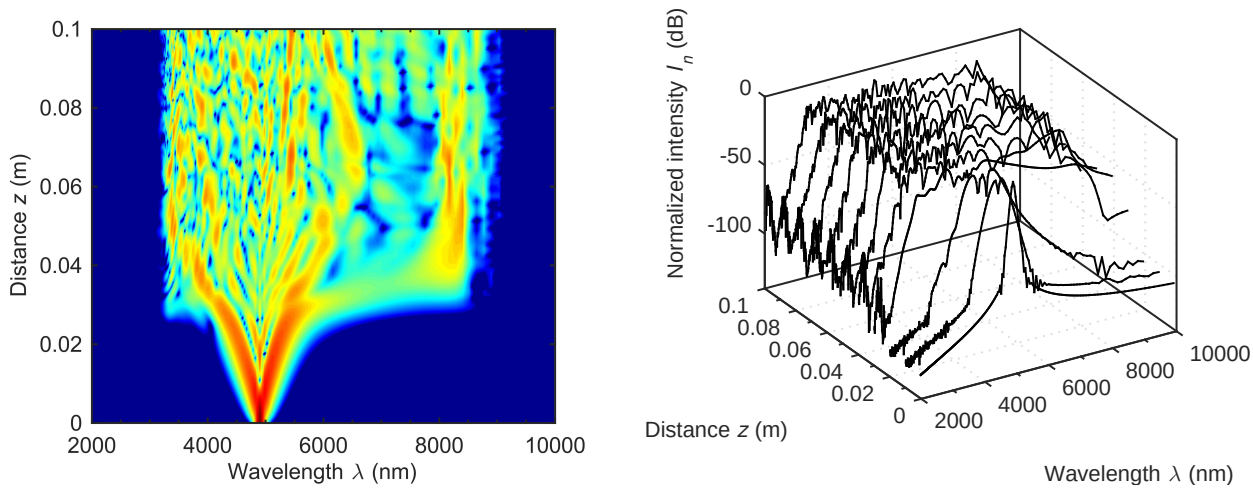

(a) (b)

Figure 4.25: Supercontinuum generation inside the LMA fiber, the pulse duration of the pump pulse is increased to 200 fs.

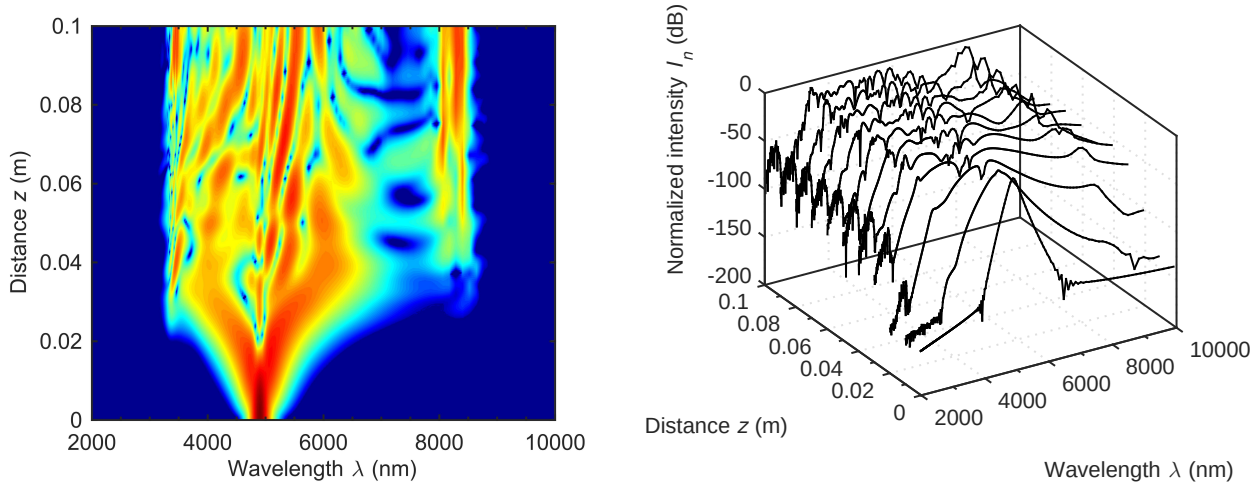

(a) (b)

Figure 4.26: Supercontinuum generation inside the LMA fiber, the peak power of the pump pulse is reduced to 25 kW.

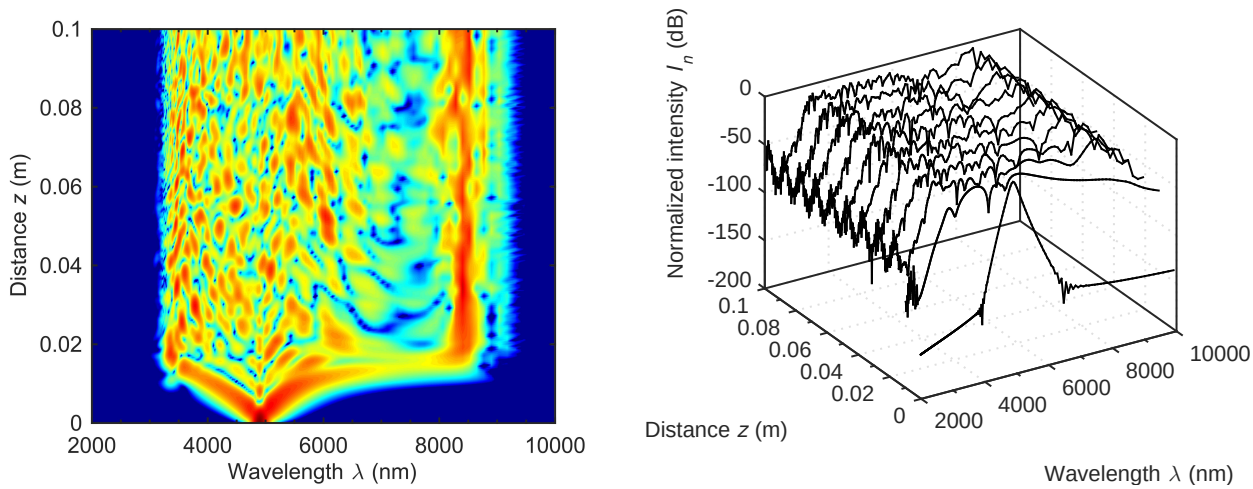

(a) (b)

Figure 4.27: Supercontinuum generation inside the LMA fiber, the peak power of the pump pulse is raised to 100 kW.

4.4.2 Summary

The large mode area fiber is designed to improve modal properties of the typical leakage channel fiber by adding two rings of sufficiently small airholes. This allows enlarging of modal area keeping the single-mode regime of operation, because the additional rings decreases confinement loss of the fundamental mode and concurrently increases confinement loss of the higher-order modes.

Supercontinuum is numerically obtained in the designed highly nonlinear chalcogenide fiber with large effective mode area. The fiber can be bent up to 10 cm radius and it is effectively single-mode over the investigated spectral region. The generated supercontinuum spans from about 3.217 to 9.172 μm, if the fiber is pumped at the wavelength of 4.9 μm by 100 fs pulses with peak power of 100 kW. The fiber should be pumped near the ZDW to involve soliton-related dynamics and consequently to generate supercontinuum as broad as possible.

Although bending is not necessary for the short fiber segment considered in the supercontinuum simulations, the fiber is designed to be pumped by much higher energies (higher peak powers and pulse durations) allowing using the longer fiber segment that can be bent.

The author recommends the designed fiber length from 5 cm to 5 m, because of the material and confinement loss that decreases output power of generated supercontinuum for longer fibers.

Chapter 5

Conclusion

Design methods described in this doctoral thesis are used as a tool to find limitations of photonic crystal fibers and consequently to optimize their geometries for telecommunication and other purposes.

On this basis the near zero dispersion photonic crystal fiber is designed to demonstrate that the three-fold symmetry can be composed without a high-index doped core, and thus doping can be significantly reduced. The author expects that doping the fiber core can be omitted in other structures aiming at dispersion optimization, too.

One of the main contributions of the doctoral thesis is the fiber design with one of the best matching of the relative dispersion slope as the referred to the standard fiber to be compensated. The author predicts that using the hexagonal fiber structure, the negative dispersion cannot be higher over the considered bandwidth.

The dual-core photonic crystal fiber is designed to operate as an optical filter. The author found that doping the inner core by germanium dioxide shifts the phase matching wavelength to C-band, where a narrow spectrum of wavelengths can be filtered.

Modal properties of a conventional leakage channel fiber are improved by adding two airholes rings with sufficiently small airhole diameter. The fiber can be bent around 10 cm radius keeping the single-mode regime of operation.

Numerical simulations carried out for femtosecond pulse propagation in the designed leakage channel fiber show that the generated supercontinuum generation is one of the broadest achieved in a large mode area fiber.

The doctoral thesis can be used as a guide for a potential designer of photonic crystal fibers. The mechanisms of the control of chromatic dispersion and confinement loss are described in details. In a similar way, different optical properties can be obtained in photonic crystal fibers to operate in telecommunication, high-power delivery and sensing.

In the field of photonic crystal fibers, there are still many unsolved and actual milestones. One of them is electric field or temperature sensing by holey fibers with high spatial resolution. Another one is to improve fabrication process of photonic crystal fibers for the middle- and far-infrared in order to reduce material loss. Supercontinuum generation in deep-ultraviolet also still seems to be a challenge.

Bibliography

[1] J. Joannopoulos, S. Johnson, J. Winn, and R. Meade, *Photonic Crystals: Molding the Flow of Light (Second Edition)*, Princeton University Press (2011).

[2] M. Lucki and L. Bohac, "Band gap structure as the photonic crystal fiber guidance mechanism," in *Proc. SPIE*, **5950**, 59501F–59501F–8 (2005). [doi:10.1117/12.622595].

[3] R. Buczynski, I. Kujawa, R. Kasztelanic, D. Pysz, K. Borzycki, F. Berghmans, H. Thienpont, and R. Stepien, "Supercontinuum generation in all-solid photonic crystal fiber with low index core," *Laser Physics* **22**(4), 784–790 (2012). [doi:10.1134/S1054660X12040019].

[4] C. Yang, J. Bai, Y. Li, and A. Wang, "Understanding all-solid honeycomb photonic bandgap fibers," *Photonics Technology Letters, IEEE* **24**(11), 915–917 (2012). [doi:10.1109/LPT.2012.2190761].

[5] M. Poulain, M. Poulain, and J. Lucas, "Verres fluores au tetrafluorure de zirconium proprietes optiques d'un verre dope au Nd3+," *Materials Research Bulletin* **10**(4), 243–246 (1975). [doi:10.1016/0025-5408(75)90106-3].

[6] M. Saad, "Heavy metal fluoride glass fibers and their applications," in *Communications and Photonics Conference and Exhibition, 2011. ACP. Asia*, 1–16 (2011). [doi:10.1117/12.915295].

[7] L. G. V. Uitert, A. J. Bruce, W. H. Grodkiewicz, and D. Wood, "Minimum loss projections for oxide and halide glasses," *Materials Science Forum* **5-6**, 591–605 (1985). [doi:10.4028/www.scientific.net/MSF.5-6.591].

[8] G. Qin, X. Yan, C. Kito, M. Liao, C. Chaudhari, T. Suzuki, and Y. Ohishi, "Ultrabroadband supercontinuum generation from ultraviolet to 6.28 μm in a fluoride fiber," *Applied Physics Letters* **95**(16) (2009). [doi:10.1063/1.3254214].

[9] Z. Meng, J. Kamebayashi, M. Higashihata, Y. Nakata, T. Okada, Y. Kubota, N. Nishimura, and T. Teshima, "1.55-μm Ce,Er:ZBLAN fiber laser operation under 980-nm pumping: experiment and simulation," *Photonics Technology Letters, IEEE* **14**(5), 609–611 (2002). [doi:10.1109/68.998700].

[10] X. Zhu and N. Peyghambarian, "High-power ZBLAN glass fiber lasers: review and prospect," *Advances in OptoElectronics"* **2010**, 1–23 (2010). [doi:10.1155/2010/501956].

[11] G. Sobon, M. Klimczak, J. Sotor, K. Krzempek, D. Pysz, R. Stepien, T. Martynkien, K. M. Abramski, and R. Buczynski, "Infrared supercontinuum generation in soft-glass photonic crystal fibers pumped at 1560 nm," *Optical Materials Express* **4**(1), 7–15 (2014). [doi:10.1364/OME.4.000007].

[12] J. Sanghera, L. B. Shaw, and I. Aggarwal, "Chalcogenide glass-fiber-based mid-ir sources and applications," *IEEE Journal of Selected Topics in Quantum Electronics* **15**(1), 114–119 (2009). [doi:10.1109/JSTQE.2008.2010245].

[13] A. Zakery and S. R. Elliott, *Optical Nonlinearities in Chalcogenide Glasses and their Applications*, Springer Berlin - Heidelberg, Berlin, Germany (2007). [doi:10.1007/978-3-540-71068-4].

[14] P. Lucas, A. A. Wilhelm, M. Videa, C. Boussard-Plédel, and B. Bureau, "Chemical stability of chalcogenide infrared glass fibers," *Corrosion Science* **50**(7), 2047–2052 (2008). [doi:10.1016/j.corsci.2008.04.020].

[15] P. Toupin, L. Brilland, G. Renversez, and J. Troles, "All-solid all-chalcogenide microstructured optical fiber," *Optics Express* **21**(12), 14643–14648 (2013). [doi:10.1364/OE.21.014643].

[16] G. Tao, S. Shabahang, H. Ren, F. Khalilzadeh-Rezaie, R. E. Peale, Z. Yang, X. Wang, and A. F. Abouraddy, "Robust multimaterial tellurium-based chalcogenide glass fibers for mid-wave and long-wave infrared transmission," *Optics Letters* **39**(13), 4009–4012 (2014). [doi:10.1364/OL.39.004009].

[17] R. H. Stolen and J. E. Bjorkholm, "Parametric amplification and frequency conversion in optical fibers," *IEEE Journal of Quantum Electronics* **18**(7), 1062–1072 (1982). [doi:10.1109/JQE.1982.1071660].

[18] R. B. Dyott and J. R. Stern, "Group delay in glass-fibre waveguide," *Electronics Letters* **7**(3), 82–84 (1971). [doi:10.1049/el:19710055].

[19] Y. Hoo, W. Jin, J. Ju, H. Ho, and D. Wang, "Design of photonic crystal fibers with ultra-low, ultra-flattened chromatic dispersion," *Optics Communications* **242**(4–6), 327–332 (2004). [doi:10.1016/j.optcom.2004.08.030].

[20] V. F. Rodriguez-Esquerre, J. P. da Silva, D. S. Bezerra, I. E. Fonseca, and H. E. Hernandez-Figueroa, "Step index holey fiber for ultra wideband residual chromatic dispersion compensation," in *Microwave and Optoelectronics Conference (IMOC), 2009 SBMO/IEEE MTT-S International*, 557–559 (2009). [doi:10.1109/IMOC.2009.5427521].

[21] K. Hansen, "Dispersion flattened hybrid-core nonlinear photonic crystal fiber," *Optics Express* **11**(13), 1503–1509 (2003). [doi:10.1364/OE.11.001503].

[22] F. Begum, Y. Namihira, S. M. A. Razzak, S. Kaijage, N. H. Hai, T. Kinjo, K. Miyagi, and N. Zou, "Novel broadband dispersion compensating photonic crystal fibers: Applications in high-speed transmission systems," *Optics & Laser Technology* **41**(6), 679–686 (2009). [doi:10.1016/j.optlastec.2009.02.001].

[23] L. P. Shen, W.-P. Huang, G. X. Chen, and S. S. Jian, "Design and optimization of photonic crystal fibers for broad-band dispersion compensation," *Photonics Technology Letters, IEEE* **15**(4), 540–542 (2003). [10.1109/LPT.2003.809322].

[24] M. S. Habib, M. S. Habib, M. I. Hasanand, and S. M. A. Razzak, "Tailoring polarization maintaining broadband residual dispersion compensating octagonal photonic crystal fibers," *Optical Engineering* **52**(11), 116111–116111–8 (2013). [10.1117/1.OE.52.11.116111].

[25] M. A. Islam and M. S. Alam, "Design of a polarization-maintaining equiangular spiral photonic crystal fiber for residual dispersion compensation over E+S+C+L+U wavelength bands," *Photonics Technology Letters, IEEE* **24**(11), 930–932 (2012). [doi:10.1109/LPT.2012.2190981].

[26] H. Subbaraman, T. Ling, Y. Jiang, M. Y. Chen, P. Cao, and R. T. Chen, "Design of a broadband highly dispersive pure silica photonic crystal fiber," *Applied Optics* **46**(16), 3263–3268 (2007). [doi:10.1364/AO.46.003263].

[27] A. Huttunen and P. Törmä, "Optimization of dual-core and microstructure fiber geometries for dispersion compensation and large mode area," *Optics Express* **13**(2), 627–635 (2005). [doi:10.1364/OPEX.13.000627].

[28] J. Yuan, X. Sang, C. Yu, C. Jin, X. Shen, G. Zhou, S. Li, and L. Hou, "Large negative dispersion in dual-concentric-core photonic crystal fiber with hybrid cladding structure based on complete leaky mode coupling," *Optics Communications* **284**(24), 5847–5852 (2011). [doi:10.1016/j.optcom.2011.08.075].

[29] T. Matsui, K. Nakajima, and I. Sankawa, "Dispersion compensation over all the telecommunication bands with double-cladding photonic-crystal fiber," *Journal of Lightwave Technology* **25**(3), 757–762 (2007). [doi:10.1109/JLT.2006.889668].

[30] S. K. Varshney, K. Saitoh, N. Saitoh, Y. Tsuchida, M. Koshiba, and R. K. Sinha, "Strategies for realizing photonic crystal fiber bandpass filters," *Optics Express* **16**(13), 9459–9467 (2008). [doi:10.1364/OE.16.009459].

[31] T. M. Monro, W. Belardi, K. Furusawa, J. C. Baggett, N. G. R. Broderick, and D. J. Richardson, "Sensing with microstructured optical fibres," *Measurement Science and Technology* **12**(7), 854–858 (2001). [doi:10.1088/0957-0233/12/7/318].

[32] A. S. Webb, F. Poletti, D. J. Richardson, and J. K. Sahu, "Suspended-core holey fiber for evanescent-field sensing," *Optical Engineering* **46**(1), 010503–010503–3 (2007). [doi:10.1117/1.2430505].

[33] J. C. Knight, T. A. Birks, P. S. J. Russell, and D. M. Atkin, "All-silica single-mode optical fiber with photonic crystal cladding," *Optics Letters* **21**(19), 1547–1549 (1996). [doi:10.1364/OL.21.001547].

[34] L. Fu, B. K. Thomas, and L. Dong, "Efficient supercontinuum generations in silica suspended core fibers," *Optics Express* **16**(24), 19629–19642 (2008). [doi:10.1364/OE.16.019629].

[35] M. Klimczak, B. Siwicki, P. Skibinski, D. Pysz, R. Stepien, A. Szolno, J. Pniewski, C. Radzewicz, and R. Buczynski, "Mid-infrared supercontinuum generation in soft-glass suspended core photonic crystal fiber," *Optical and Quantum Electronics* **46**(4), 563–571 (2014). [doi:10.1007/s11082-013-9802-1].

[36] T. M. Monro, S. Warren-Smith, E. P. Schartner, A. François, S. Heng, H. Ebendorff-Heidepriem, and S. V. Afshar, "Sensing with suspended-core optical fibers," *Optical Fiber Technology* **16**(6), 343–356 (2010). [doi:10.1016/j.yofte.2010.09.010].

[37] A. Mazhorova, A. Markov, A. Ng, R. Chinnappan, O. Skorobogata, M. Zourob, and M. Skorobogatiy, "Label-free bacteria detection using evanescent mode of a suspended core terahertz fiber," *Optics Express* **20**(5), 5344–5355 (2012). [doi:10.1364/OE.20.005344].

[38] I. Dicaire, J.-C. Beugnot, and L. Thévenaz, "Suspended-core fibres as optical gas sensing cells: study and implementation," in *Proc. SPIE*, **7357**, 73570U–73570U–9 (2009). [doi:10.1117/12.820791].

[39] R. Kostecki, H. Ebendorff-Heidepriem, C. Davis, G. McAdam, S. C. Warren-Smith, and T. Monro, "Silica exposed-core microstructured optical fibers," *Optical Materials Express* **2**(11), 1538–1547 (2012). [doi:10.1364/OME.2.001538].

[40] Y. L. Hoo, W. Jin, C. Shi, H. L. Ho, D. N. Wang, and S. C. Ruan, "Design and modeling of a photonic crystal fiber gas sensor," *Applied Optics* **42**(18), 3509–3515 (2003). [doi:10.1364/AO.42.003509].

[41] F. M. Cox, R. Lwin, M. C. J. Large, and C. M. B. Cordeiro, "Opening up optical fibres," *Optics Express* **15**(19), 11843–11848 (2007). [doi:10.1364/OE.15.011843].

[42] S. C. Warren-Smith, H. Ebendorff-Heidepriem, T. C. Foo, R. Moore, C. Davis, and T. M. Monro, "Exposed-core microstructured optical fibers for real-time fluorescence sensing," *Optics Express* **17**(21), 18533–18542 (2009). [doi:10.1364/OE.17.018533].

[43] B. Ung and M. Skorobogatiy, "Chalcogenide microporous fibers for linear and nonlinear applications in the mid-infrared," *Optics Express* **18**(8), 8647–8659 (2010). [doi:10.1364/OE.18.008647].

[44] L. Dong, X. Peng, and J. Li, "Leakage channel optical fibers with large effective area," *Journal of the Optical Society of America B* **24**(8), 1689–1697 (2007). [doi:10.1364/JOSAB.24.001689].

[45] M. Fermann, A. Galvanauskas, G. Sucha, and D. Harter, "Fiber-lasers for ultrafast optics," *Journal of Applied Physics B* **65**(2), 259–275 (1997). [doi:10.1007/s003400050272].

[46] M.-J. Li, X. Chen, A. Liu, S. Gray, J. Wang, D. Walton, and L. Zenteno, "Limit of effective area for single-mode operation in step-index large mode area laser fibers," *Journal of Lightwave Technology* **27**(15), 3010–3016 (2009). [doi:10.1109/JLT.2009.2020682].

[47] A. Barh, S. Ghosh, R. Varshney, and B. P. Pal, "Ultra-large mode area microstructured core chalcogenide fiber design for mid-ir beam delivery," *Optics Communications* **311**, 129–133 (2013). [doi:10.1016/j.optcom.2013.08.047].

[48] A. Millo, L. Lobachinsky, and A. Katzir, "Single-mode index-guiding photonic crystal fibers for the middle infrared," *Photonics Technology Letters, IEEE* **20**(10), 869–871 (2008). [doi:10.1109/LPT.2008.921850].

[49] M.-Y. Chen, Y.-R. Li, J. Zhou, and Y.-K. Zhang, "Design of asymmetric large-mode area optical fiber with low-bending loss," *Journal of Lightwave Technology* **31**(3), 476–481 (2013). [doi:10.1109/JLT.2012.2230245].

[50] M. Napierala, T. Nasilowski, E. Berea-Pawlik, F. Berghmans, J. Wojcik, and H. Thienpont, "Extremely large-mode-area photonic crystal fibre with low bending loss," *Optics Express* **18**(15), 15408–15418 (2010). [doi:10.1364/OE.18.015408].

[51] M. A. Islam and M. S. Alam, "An extremely large mode area microstructured core leakage channel fiber with low bending loss," *Journal of Lightwave Technology* **32**(2), 250–256 (2014). [doi:10.1109/JLT.2013.2292876].

[52] K. Saitoh, S. Varshney, K. Sasaki, L. Rosa, M. Pal, M. Paul, D. Ghosh, S. Bhadra, and M. Koshiba, "Limitation on effective area of bent large-mode-area leakage channel fibers," *Journal of Lightwave Technology* **29**(17), 2609–2615 (2011). [doi:10.1109/JLT.2011.2161603].

[53] X. Feng, W. H. Loh, J. C. Flanagan, A. Camerlingo, S. Dasgupta, P. Petropoulos, P. Horak, K. E. Frampton, N. M. White, J. H. Price, H. N. Rutt, and D. J. Richardson, "Single-mode tellurite glass holey fiber with extremely large mode area for infrared nonlinear applications," *Optics Express* **16**(18), 13651–13656 (2008). [doi:10.1364/OE.16.013651].

[54] M. Lucki, "Negative chromatic dispersion in selected types of photonic crystal fibres obtained by bending," in *Transparent Optical Networks (ICTON), 2009 11th International Conference on*, 1–4 (2009). [doi:10.1109/ICTON.2009.5185081].

[55] M. A. Islam and M. S. Alam, "Bend-insensitive single-mode photonic crystal fiber with ultralarge effective area for dual applications," *Optical Engineering* **52**(5), 050501–050501–3 (2013). [doi:10.1117/1.OE.52.5.050501].

[56] G. S. Murugan, Ed., *Chalcogenide glasses for photonics device applications*, Research Signpost (2010).

[57] R. F. Souza, M. A. R. C. Alencar, J. M. Hickmann, R. Kobayashi, and L. R. P. Kassab, "Femtosecond nonlinear optical properties of tellurite glasses," *Applied Physics Letters* **89**(17) (2006). [doi:10.1063/1.2364467].

[58] T. Cardinal, K. A. Richardson, H. Shim, A. Schulte, R. Beatty, K. L. Foulgoc, C. Meneghini, J. F. Viens, and A. Villeneuve, "Non-linear optical properties of chalcogenide glasses in the system As-S-Se," *Journal of Non-Crystalline Solids* **256-257**, 353–360 (1999). [doi:10.1016/S0022-3093(99)00524-4].

[59] E. Yousef, M. Hotzel, and C. Rüssel, "Linear and non-linear refractive indices of tellurite glasses in the system TeO_2-WO_3-ZnF_2," *Journal of Non-Crystalline Solids* **342**(1–3), 82–88 (2004). [doi:10.1016/j.jnoncrysol.2004.07.003].

[60] J. M. Dudley, G. Genty, and S. Coen, "Supercontinuum generation in photonic crystal fiber," *Reviews of Modern Physics* **78**, 1135–1184 (2006). [doi:10.1103/RevModPhys.78.1135].

[61] J. B. Ashcom, R. R. Gattass, C. B. Schaffer, and E. Mazur, "Numerical aperture dependence of damage and supercontinuum generation from femtosecond laser pulses in bulk fused silica," *Journal of the Optical Society of America B* **23**(11), 2317–2322 (2006). [doi:10.1364/JOSAB.23.002317].

[62] Y. Yu, X. Gai, T. Wang, P. Ma, R. Wang, Z. Yang, D.-Y. Choi, S. Madden, and B. Luther-Davies, "Mid-infrared supercontinuum generation in chalcogenides," *Optical Materials Express* **3**(8), 1075–1086 (2013). [doi:10.1364/OME.3.001075].

[63] A. B. Seddon, "Chalcogenide glasses: a review of their preparation, properties and applications," *Journal of Non-Crystalline Solids* **184**, 44–50 (1995). [doi:10.1016/0022-3093(94)00686-5].

[64] H. Ebendorff-Heidepriem, K. Kuan, M. R. Oermann, K. Knight, and T. M. Monro, "Extruded tellurite glass and fibers with low OH content for mid-infrared applications," *Optical Materials Express* **2**(4), 432–442 (2012). [doi:10.1364/OME.2.000432].

[65] Q. Nguyen-The, M. Matsuura, and N. Kishi, "WDM-to-OTDM conversion using supercontinuum generation in a highly nonlinear fiber," *Photonics Technology Letters, IEEE* **26**(18), 1882–1885 (2014). [doi:10.1109/LPT.2014.2339932].

[66] G. Humbert, W. Wadsworth, S. Leon-Saval, J. Knight, T. Birks, P. S. J. Russell, M. Lederer, D. Kopf, K. Wiesauer, E. Breuer, and D. Stifter, "Supercontinuum generation system for optical coherence tomography based on tapered photonic crystal fibre," *Optics Express* **14**(4), 1596–1603 (2006). [doi:10.1364/OE.14.001596].

[67] G. McConnell, "Confocal laser scanning fluorescence microscopy with a visible continuum source," *Optics Express* **12**, 2844–2850 (2004). [doi:10.1364/OPEX.12.002844].

[68] H. Kano and H. Hamaguchi, "Characterization of a supercontinuum generated from a photonic crystal fiber and its application to coherent Raman spectroscopy," *Optics Letters* **28**(23), 2360–2362 (2003). [doi:10.1364/OL.28.002360].

[69] R. R. Alfano and S. L. Shapiro, "Emission in the region 4000 to 7000 å via four-photon coupling in glass," *Physical Review Letters* **24**(11), 584–587 (1970). [doi:10.1103/PhysRevLett.24.584].

[70] P. L. Baldeck and R. Alfano, "Intensity effects on the stimulated four photon spectra generated by picosecond pulses in optical fibers," *Journal of Lightwave Technology,* **5**, 1712–1715 (1987). [doi:10.1109/JLT.1987.1075465].

[71] J. K. Ranka, R. S. Windeler, and A. J. Stentz, "Visible continuum generation in air–silica microstructure optical fibers with anomalous dispersion at 800 nm," *Optics Letters* **25**(1), 25–27 (2000). [doi:10.1364/OL.25.000025].

[72] J. H. V. Price, T. M. Monro, K. Furusawa, W. Belardi, J. C. Baggett, S. Coyle, C. Netti, J. J. Baumberg, R. Paschotta, and D. J. Richardson, "UV generation in a pure-silica holey fiber," *Applied Physics B* **77**(2-3), 291–298 (2003). [doi:10.1007/s00340-003-1174-y].

[73] H.-W. Chen, A.-J. Jin, W.-Q. Yang, S.-P. Chen, J. Hou, and Q.-S. Lu, "Generation of a compact high-power high-efficiency normal-dispersion pumping supercontinuum in silica photonic crystal fiber pumped with a 1064-nm picosecond pulse," *Chinese Physics B* **22**(6), 064211 (2013). [doi:10.1088/1674-1056/22/6/064211].

[74] M. Durand, L. Khan, V. Jukna, E. McKee, M. Baudelet, A. Houard, M. Richardson, A. Mysyrowicz, and A. Couairon, "Influence of the anomalous dispersion on the supercontinuum generation by femtosecond laser filamentation," in *Conference on Lasers and Electro-Optics (CLEO), 2013*, 1–2 (2013).

[75] C. Larsen, S. T. Sørensen, D. Noordegraaf, K. P. Hansen, K. E. Mattsson, and O. Bang, "Zero-dispersion wavelength independent quasi-cw pumped supercontinuum generation," *Optics Communications* **290**, 170–174 (2013). [doi:10.1016/j.optcom.2012.10.030].

[76] C. Xia, M. Kumar, O. P. Kulkarni, M. N. Islam, F. L. Terry, M. J. Freeman, M. Poulain, and G. Mazé, "Mid-infrared supercontinuum generation to 4.5 μm in ZBLAN fluoride fibers by nanosecond diode pumping," *Optics Letters* **31**(17), 2553–2555 (2006). [doi:10.1364/OL.31.002553].

[77] P. Domachuk, N. A. Wolchover, M. Cronin-Golomb, A. Wang, A. K. George, C. M. B. Cordeiro, J. C. Knight, and F. G. Omenetto, "Over 4000 nm bandwidth of mid-IR supercontinuum generation in sub-centimeter segments of highly nonlinear tellurite PCFs," *Optics Express* **16**(10), 7161–7168 (2008). [doi:10.1364/OE.16.007161].

[78] E. Coscelli, F. Poli, J. Li, A. Cucinotta, and S. Selleri, "Chalcogenide suspended-core fibers for supercontinuum generation in the mid-infrared," in *Proc. SPIE*, **9347**, 93471P–93471P–9 (2015). [doi:10.1117/12.2077431].

[79] W. Yuan, "2-10 μm mid-infrared supercontinuum generation in As_2Se_3 photonic crystal fiber," *Laser Physics Letters* **10**(9), 1–6 (2013). [doi:10.1088/1612-2011/10/9/095107].

[80] A. Boucon, T. Sylvestre, K. P. Huy, J.-C. Beugnot, G. Mélin, H. Maillotte, and J. M. Dudley, "Supercontinuum generation by nanosecond dual-pumping near the two zero-dispersion wavelengths of a photonic crystal fiber," *Optics Communications* **284**(1), 467–470 (2011). [doi:10.1016/j.optcom.2010.09.035].

[81] C. R. Petersen, U. Møller, I. Kubat, B. Zhou, S. Dupont, J. Ramsay, T. Benson, S. Sujecki, N. Abdel-Moneim, Z. Tang, D. Furniss, A. Seddon, and O. Bang, "Mid-infrared supercontinuum covering the 1.4-13.3 μm molecular fingerprint region using ultra-high na chalcogenide step-index fibre," *Nature Photonics* **8**(11), 830–834 (2014). [doi:10.1038/nphoton.2014.213].

[82] R. Cherif, M. Zghal, I. Nikolov, and M. Danailov, "High energy femtosecond supercontinuum light generation in large mode area photonic crystal fiber," *Optics Communications* **283**(21), 4378 – 4382 (2010). [doi:10.1016/j.optcom.2010.06.070].

[83] J. Zhu and Z. Chen, "Validity of modal expansion method for the optical waveguide with PML," in *IEEE International Conference of Electron Devices and Solid-State Circuits (EDSSC)*, 1–4 (2010). [doi:10.1109/EDSSC.2010.5713672].

[84] T. P. White, B. T. Kuhlmey, R. C. McPhedran, D. Maystre, G. Renversez, C. M. de Sterke, and L. C. Botten, "Multipole method for microstructured optical fibers. I. formulation," *Journal of the Optical Society of America B* **19**(10), 2322–2330 (2002). [doi:10.1364/JOSAB.19.002322].

[85] A. Cucinotta, S. Selleri, L. Vincetti, and M. Zoboli, "Holey fiber analysis through the finite-element method," *Photonics Technology Letters, IEEE* **14**(11), 1530–1532 (2002). [doi:10.1109/LPT.2002.803375].

[86] Z. Zhu and T. Brown, "Full-vectorial finite-difference analysis of microstructured optical fibers," *Optics Express* **10**(17), 853–864 (2002). [doi:10.1364/OE.10.000853].

[87] K. Saitoh and M. Koshiba, "Numerical modeling of photonic crystal fibers," *Journal of Lightwave Technology* **23**(11), 3580–3590 (2005). [doi:10.1109/JLT.2005.855855].

[88] K. Yee, "Numerical solution of initial boundary value problems involving Maxwell's equations in isotropic media," *IEEE Transactions on Antennas and Propagation* **14**(3), 302–307 (1966). [doi:10.1109/TAP.1966.1138693].

[89] W. Yu and R. Mittra, "A conformal finite difference time domain technique for modeling curved dielectric surfaces," *Microwave and Wireless Components Letters, IEEE* **11**(1), 25–27 (2001). [doi:10.1109/7260.905957].

[90] K. Saitoh and M. Koshiba, "Empirical relations for simple design of photonic crystal fibers," *Optics Express* **13**(1), 267–274 (2005). [doi:10.1364/OPEX.13.000267].

[91] W. Sellmeier, "Zur erklärung der abnormen farbenfolge im spektrum einiger substanzen," *Annalen der Physik* **143**, 272–282 (1871). [doi:10.1002/andp.18712190612].

[92] A. L. Cauchy, *Mémoire sur la dispersion de la lumière*, J. G. Calve, Prague (1836).

[93] V. Brückner, *Elements of Optical Networking: Basics and practice of optical data communication*, Vieweg+Teubner Verlag, Springer, Wiesbaden, Germany (2011). [ISBN:978-3-8348-1302-2].

[94] Y. Bing, K. Oshono, Y. Kurosawa, T. Kumagai, and M. Tachikura, "Low-loss holey fiber," *Hitachi Cable Review* **24**, 1–4 (2005).

[95] B. T. Kuhlmey, R. C. McPhedran, and C. M. de Sterke, "Modal cutoff in microstructured optical fibers," *Optics Letters* **27**(19), 1684–1686 (2002). [doi:10.1364/OL.27.001684].

[96] R. T. Schermer and J. H. Cole, "Improved bend loss formula verified for optical fiber by simulation and experiment," *IEEE Journal of Quantum Electronics* **43**(10), 899–909 (2007). [doi:10.1109/JQE.2007.903364].

[97] M. J. Steel, T. P. White, C. M. de Sterke, R. C. McPhedran, and L. C. Botten, "Symmetry and degeneracy in microstructured optical fibers," *Optics Letters* **26**(8), 488–490 (2001). [doi:10.1364/OL.26.000488].

[98] Lumerical Solutions, Inc., Suite 300–535 Thurlow Street, Vancouver, BC V6E 3L2, Canada, *Lumerical Knowledge Base, Release 2015a* (2003-2014). http://docs.lumerical.com/en/index.html.

[99] J. Yu and K. Oh, "New in-line fiber band pass filters using high silica dispersive optical fibers," *Optics Communications* **204**(1–6), 111–118 (2002). [doi:10.1016/S0030-4018(02)01110-0].

[100] F. Poletti, V. Finazzi, T. M. Monro, N. G. R. Broderick, V. Tse, and D. J. Richardson, "Inverse design and fabrication tolerances of ultra-flattened dispersion holey fibers," *Optics Express* **13**(10), 3728–3736 (2005). [doi:10.1364/OPEX.13.003728].

[101] L. Gruner-Nielsen, M. Wandel, P. Kristensen, C. Jorgensen, L. V. Jorgensen, B. Edvold, B. Palsdottir, and D. Jakobsen, "Dispersion-compensating fibers," *Journal of Lightwave Technology* **23**(11), 3566–3579 (2005). [doi:10.1109/JLT.2005.855873].

[102] Y. Kodama and A. Hasegawa, "Nonlinear pulse propagation in a monomode dielectric guide," *IEEE Journal of Quantum Electronics* **23**(5), 510–524 (1987). [doi:10.1109/JQE.1987.1073392].

[103] J. M. Dudley and J. R. Taylor, *Supercontinuum Generation in Optical Fibers*, Cambridge University Press, Cambridge, United Kingdom (2010). [ISBN:9781139486187].

[104] G. P. Agrawal, *Nonlinear Fiber Optics (Fourth Edition)*, Academic Press, San Diego, fourth edition ed. (2006). [doi:10.1016/B978-012369516-1/50002-9].

[105] J. Hult, "A fourth-order runge-kutta in the interaction picture method for simulating supercontinuum generation in optical fibers," *Journal of Lightwave Technology* **25**(12), 3770–3775 (2007). [doi:10.1109/JLT.2007.909373].

[106] S. Coen, A. H. L. Chau, R. Leonhardt, J. D. Harvey, J. C. Knight, W. J. Wadsworth, and P. S. J. Russell, "Supercontinuum generation by stimulated Raman scattering and parametric four-wave mixing in photonic crystal fibers," *Journal of the Optical Society of America B* **19**(4), 753–764 (2002). [doi:10.1364/JOSAB.19.000753].

[107] I. G. Cormack, D. T. Reid, W. J. Wadsworth, J. C. Knight, and P. S. J.Russell, "Observation of soliton self-frequency shift in photonic crystal fibre," *Electronics Letters* **38**(4), 167–169 (2002). [doi:10.1049/el:20020128].

[108] N. Akhmediev and M. Karlsson, "Cherenkov radiation emitted by solitons in optical fibers," *Physical review A* **51**, 2602–2607 (1995). [doi:10.1103/PhysRevA.51.2602].

[109] G. Genty, M. Lehtonen, and H. Ludvigsen, "Effect of cross-phase modulation on supercontinuum generated in microstructured fibers with sub-30 fs pulses," *Optics Express* **12**(19), 4614–4624 (2004). [doi:10.1364/OPEX.12.004614].

[110] A. Martinez-Rios, I. Torres-Gomez, D. Monzon-Hernandez, O. Barbosa-Garcia, and V. Duran-Ramirez, "Reduction of splice loss between dissimilar fibers by tapering & fattening," *Revista Mexicana de Fisica* **56**, 80–84 (2010).

[111] W. S. Rodney, I. H. Malitson, and T. A. King, "Refractive index of arsenic trisulfide," *Journal of the Optical Society of America* **48**(9), 633–635 (1958). [doi:10.1364/JOSA.48.000633].

[112] M. Bass, C. DeCusatis, J. Enoch, V. Lakshminarayanan, G. Li, C. MacDonald, V. Mahajan, and E. V. Stryland, *Handbook of Optics, Third Edition Volume IV: Optical Properties of Materials, Nonlinear Optics, Quantum Optics*, McGraw Hill Professional, Penn Plaza, New York (2009). [ISBN:978-0-0716-2929-4].

[113] F. Gan, "Optical properties of fluoride glasses: a review," *Journal of Non-Crystalline Solids* **184**, 9–20 (1995). [doi:10.1016/0022-3093(94)00592-3].

[114] T. Cheng, Y. Kanou, D. Deng, X. Xue, M. Matsumoto, T. Misumi, T. Suzuki, and Y. Ohishi, "Fabrication and characterization of a hybrid four-hole $AsSe_2$-As_2S_5 microstructured optical fiber with a large refractive index difference," *Optics Express* **22**(11), 13322–13329 (2014). [doi:10.1364/OE.22.013322].

[115] T. Kohoutek, Z. Duan, H. Kawashima, T. Cheng, and T. Suzuki, "Tailoring chromatic dispersion in chalcogenide-tellurite microstructured optical fiber," *Optical Fiber Technology* **20**(4), 409–413 (2014). [doi:10.1016/j.yofte.2014.05.004].

[116] X. Feng, J. Shi, M. Segura, N. M. White, P. Kannan, L. Calvez, X. Zhang, L. Brilland, and W. H. Loh, "Towards water-free tellurite glass fiber for 2-5 μm nonlinear applications," *Fibers* **1**(3), 70 (2013). [doi:10.3390/fib1030070].

Publications of the Author

[A.1] R. Zeleny. *Photonic Crystal Fibers: Optimization for Telecommunication Purposes.* Doctoral Thesis Proposal, Faculty of Electrical Engineering, Prague, Czech Republic, 2013.

Impacted factor journal articles:

[A.2] R. Zeleny and M. Lucki. *Dispersion limits in the design of small-mode-area photonic crystal fibers.* Optical Engineering **53**(10), pp. 105103–105103-8, 2014. [Author's share: 50 %].

[A.3] R. Zeleny and M. Lucki. *Nearly zero dispersion-flattened photonic crystal fiber with fluorine-doped three-fold symmetry core.* Optical Engineering **52**(4), pp. 045003–045003-6, 2013. [Author's share: 50 %].

The paper has been cited in:

- A. Medjouri, L. M. Simohamed, O. Ziane, A. Boudrioua, Z. Becer. *Design of a circular photonic crystal fiber with flattened chromatic dispersion using a defected core and selectively reduced air holes: Application to supercontinuum generation at 1.55 μm*, Photonics and Nanostructures - Fundamentals and Applications **16**, pp. 43–50, 2015.
- A. Medjouri, L. M. Simohamed, O. Ziane, A. Boudrioua. *Investigation of high birefringence and chromatic dispersion management in photonic crystal fibre with square air holes*, Optik - International Journal for Light and Electron Optics **126**(20), pp. 2269–2274, 2015.

Conference articles excerpted by WoS:

[A.4] R. Zeleny and M. Lucki. *Design of As_2S_3-based chalcogenide photonic crystal fibre with large mode area and low bending loss for mid-infrared*, Transparent Optical Networks (ICTON), 2015 17th International Conference on, pp. 1–4, 2015. [Author's share: 50 %].

[A.5] M. Lucki, S. Kraus, R. Zeleny, J. Zehetner, D. Seyringer, J. Latal, and F. Perecar. *Investigation of optical thin films printed on the surface of facets of photonic crystal fibers*, Microstructured and Specialty Optical Fibres, Proc. SPIE 9507, Bellingham: SPIE, pp. 95070A–95070A-11, 2015. [Author's share: 14 %].

[A.6] R. Zeleny and M. Lucki. *Dispersion limits of the small mode area photonic crystal fibers designed as a broadband compensator*, Microstructured and Specialty Optical Fibres, Proc. SPIE 9125, Bellingham: SPIE, pp. 91280T–91280T-8, 2014. [Author's share: 50 %].

[A.7] M. Lucki and R. Zeleny. *Broadband submicron flattened dispersion compensating fiber with asymmetrical fluoride doped core.* Microstructured and Specialty Optical Fibres, Proc. of SPIE 8775, Bellingham: SPIE, pp. 87750M–87750M-8, 2013. [Author's share: 50 %].

[A.8] R. Zeleny and M. Lucki. *Broadband dispersion decreasing photonic crystal fiber for compression of optical pulses*, Microstructured and Specialty Optical Fibres, Proc. SPIE 8775, Bellingham: SPIE, pp. 87750Y–87750Y-8, 2013. [Author's share: 50 %].

The paper has been cited in:

- J. Latal, J. Vitasek, P. Koudelka, P. Siska, R. Poboril, L. Hajek, A. Vanderka, V. Vasinek. *Simulation of modulation formats for optical access network based on WDM-PON*, Transparent Optical Networks (ICTON), 2014 16th International Conference, pp. 1–7, 2014.

[A.9] M. Lucki and R. Zeleny. *Broadband dispersion compensating photonic crystal fiber*, Photonics, Devices, and Systems V, Proc. SPIE 8306, Bellingham: SPIE, pp. 83060Z–83060Z-6, 2011. [Author's share: 50 %].

Invited paper:

[A.10] R. Zeleny, M. Lucki. *An improved non-linear nearly-zero dispersion flattened photonic crystal fiber with the threefold symmetry core*, Microstructured and Specialty Optical Fibres, Proc. SPIE 8426, Bellingham: SPIE, pp. 84260R–84260R-8, 2012. [Author's share: 50 %].

Other conference articles:

[A.11] R. Zeleny and M. Lucki, *Design of a Narrowband Photonic Filter Based on the Leaky Outer Defect Mode*, 16th Mechatronika 2014, Brno: Brno University of Technology, pp. 428–432, 2014. [Author's share: 50 %].

[A.12] R. Zeleny and M. Lucki. *Novel Large Effective Mode Area Photonic Crystal Fiber with Zero Dispersion at 1550 nm*, Research in Telecommunication Technologies Conference Proceedings and Workshop, Žilina: University of Žilina, pp. 185–188, 2012. [Author's share: 50 %].

[A.13] R. Zeleny. *Broadband Dispersion Compensating Index Guiding Photonic Crystal Fiber*, POSTER 2012 - 16th International Student Conference on Electrical Engineering, Prague: Czech Technical University in Prague, 2012.

[A.14] R. Zeleny, K. Botah, and M. Lucki. *A Nearly-Zero Ultra-Flattened Dispersion Photonic Crystal Fiber with Low Confinement Loss for Broadband Transmission Systems*, 23rd Conference and Exhibition on Optical Communications 2011 - Scientific Section Proceedings, Prague: Action M, pp. 45–47, 2011. [Author's share: 33 %].

Appendix A

Materials

In this appendix, refractive indices are specified not only for the materials used in the doctoral thesis, but also for other materials that are broadly used during a PCF fabrication process, such as silica, fluoride, tellurite and chalcogenide glasses.

A.1 Refractive Indices and Material Dispersions

The material refractive indices are specified by Sellmeier approximating formula, Eq. (A.1).

$$n^2(\lambda) = 1 + \sum_j \frac{B_j \cdot \lambda^2}{\lambda^2 - C_j}. \tag{A.1}$$

The material dispersions are calculated as presented in Sec. 3.1.1.1 in Eq. (3.7) substituting n_{eff} by n.

A.1.1 Silica Materials

Refractive indices of selected silica materials are summarized in Tab. A.1 and A.2. The coefficients for silica, silica doped by germanium dioxide, phosphorus pentoxide, boron trioxide, and fluorine are given from Refs. 112, 93, and 99, respectively. The spectral range, to which they relate, is from 400 to 1700 nm. The refractive index wavelength dependence for high-index and low-index doped silica is depicted in Fig. A.1 and A.3, respectively. The material dispersion wavelength dependence is shown in Fig. A.2 and A.4

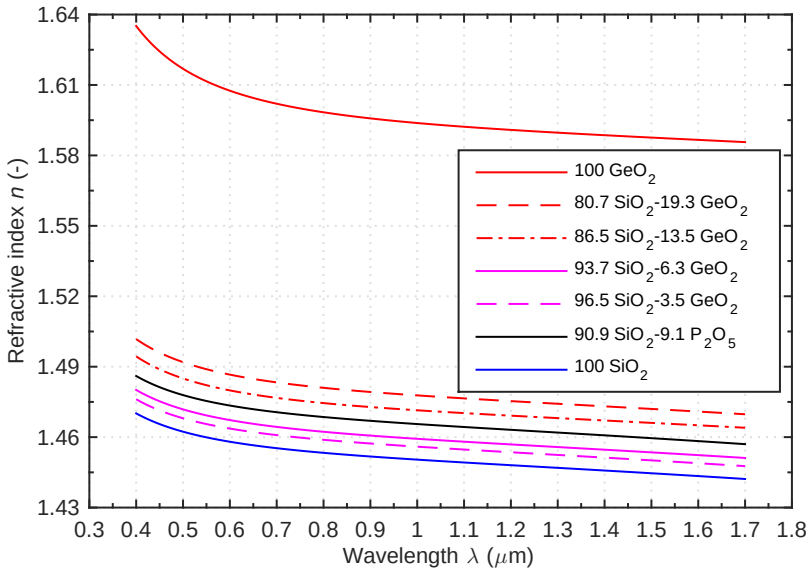

Figure A.1: Refractive index wavelength dependence of selected silica materials doped by GeO_2 and P_2O_5.

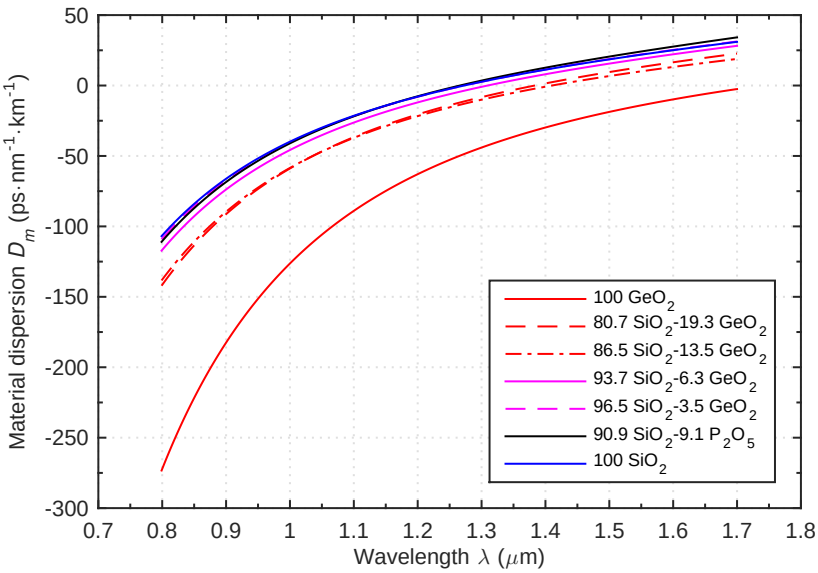

Figure A.2: Material dispersion upon wavelength for selected silica materials doped by GeO_2 and P_2O_5.

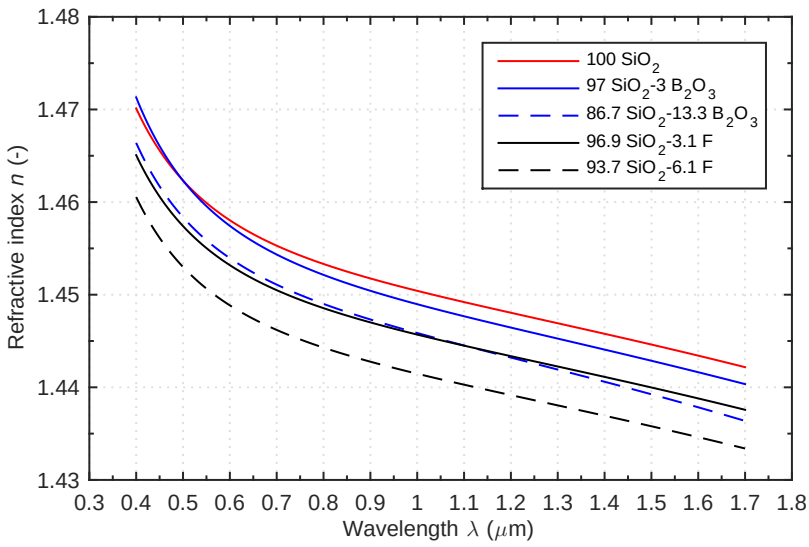

Figure A.3: Refractive index wavelength dependence of selected silica materials doped by B_2O_3 and F.

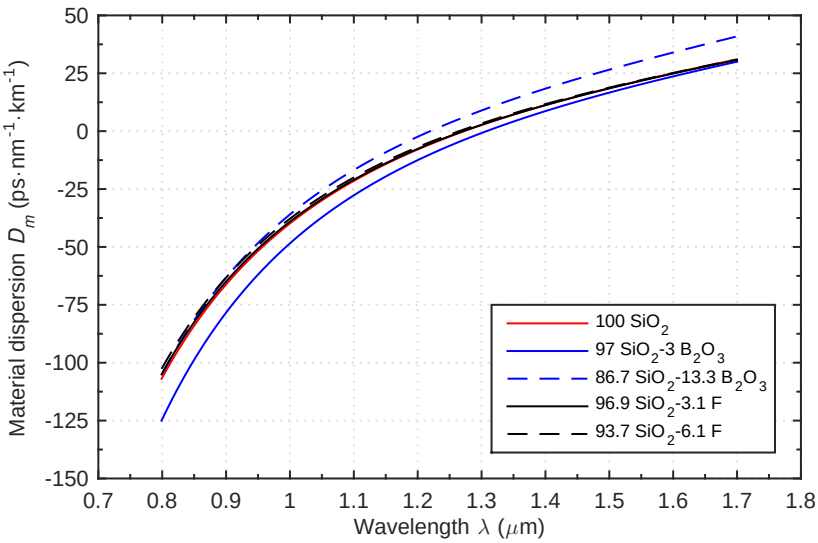

Figure A.4: Material dispersion upon wavelength for selected silica materials doped by B_2O_3 and F.

Table A.1: Sellmeier coefficients of selected silica materials doped by GeO_2 and P_2O_5.

Chemical composition (Mol.%)	B_1 (-)	B_2 (-)	B_3 (-)
100 GeO_2 [112]	0.8068664	0.0689726	0.7181585
80.7 SiO_2–19.3 GeO_2 [93]	0.7347008	0.4461191	0.8081698
86.5 SiO_2–13.5 GeO_2 [93]	0.7345440	0.4271083	0.8210340
93.7 SiO_2–6.3 GeO_2 [93]	0.7083925	0.4203993	0.8663412
96.5 SiO_2–3.5 GeO_2 [93]	0.7042038	0.4160032	0.9074049
90.9 SiO_2–9.1 P_2O_5 [93]	0.6957900	0.4524970	0.7125130
100 SiO_2 [93]	0.6961663	0.4079426	0.8974994
Mol.%	C_1 (μm^2)	C_2 (μm^2)	C_3 (μm^2)
100 GeO_2 [112]	0.00475722	0.02370556	140.23132981
80.7 SiO_2–19.3 GeO_2 [93]	0.00584734	0.01552718	97.93483382
86.5 SiO_2–13.5 GeO_2 [93]	0.00756498	0.01253323	109.96752117
93.7 SiO_2–6.3 GeO_2 [93]	0.00729046	0.01050295	97.93427963
96.5 SiO_2–3.5 GeO_2 [93]	0.00264623	0.01668231	97.93390358
90.9 SiO_2–9.1 P_2O_5 [93]	0.00379062	0.01438104	74.93743340
100 SiO_2 [93]	0.00467915	0.01351206	97.93400254

Table A.2: Sellmeier coefficients of selected silica materials doped by B_2O_3 and F.

Chemical composition (Mol.%)	B_1 (-)	B_2 (-)	B_3 (-)
97 SiO_2–3 B_2O_3 [99]	0.6935408	0.4052977	0.9111432
86.7 SiO_2–13.3 B_2O_3 [99]	0.6906180	0.4019960	0.8988170
96.9 SiO_2–3.1 F [99]	0.6932500	0.3972000	0.8600800
93.9 SiO_2–6.1 F [99]	0.6774400	0.4010100	0.8719300
Mol.%	C_1 (μm^2)	C_2 (μm^2)	C_3 (μm^2)
97 SiO_2–3 B_2O_3 [99]	0.0051412	0.0157853	97.9338700
86.7 SiO_2–13.3 B_2O_3 [99]	0.0058473	0.0155272	82.7910731
96.9 SiO_2–3.1 F [99]	0.0045212	0.0137218	95.5721312
93.9 SiO_2–6.1 F [99]	0.0037638	0.0144721	97.1466497

A.1.2 Heavy Fluoride Materials

ZBLAN glass (53 $ZrF_4 - 20\ BaF_2 - 4\ LaF_3 - 3\ AlF_3 - 20\ NaF$) is one of the most promising fluoride materials that is transparent from about 0.25 to 6.9 μm. Its refractive index can be specified by the Sellmeier formula with the coefficients as in Ref. 113. Another fluorides AYR (40 AlF_3 – 15 YF_3 – 10 MgF_2 – 20 CaF_2 – 10 SrF_2 – 5 BaF_2) and IZBS (40 $InF_3 - 20\ ZnF_2 - 20\ BaF_2 - 20\ SrF_2$) are given from this reference, too. The refractive index and material dispersion wavelength dependence is for the fluorides materials shown in Fig. A.5 and A.6, respectively The Sellmeier coefficients are summarized in Tab. A.3.

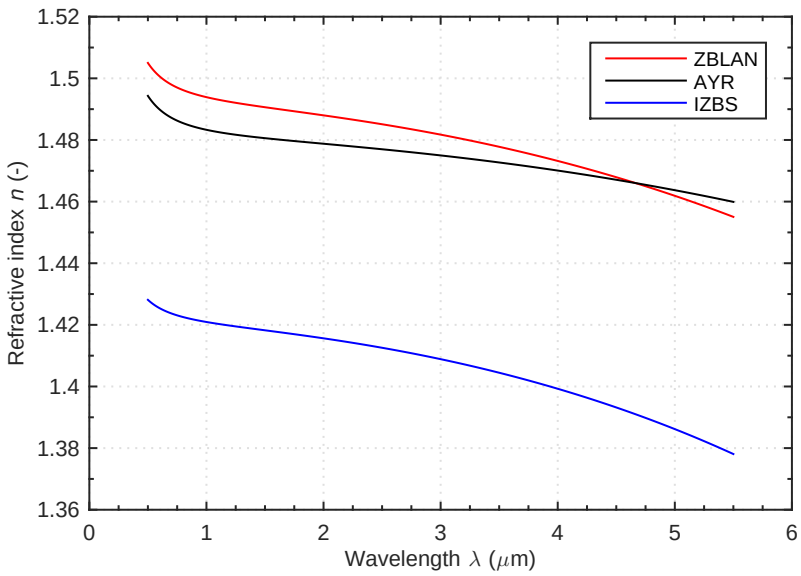

Figure A.5: Refractive index wavelength dependence of selected fluoride materials.

Table A.3: Sellmeier coefficients of selected fluorides materials.

Glass	B_1 (-)	B_2 (-)
ZBLAN [113]	1.22514	1.52898
IZBS [113]	1.19200	1.20869
AYR [113]	1.01675	1.04228
Glass	C_1 (μm^2)	C_2 (μm^2)
ZLBAN [113]	0.0080442961	457.21130625
IZBS [113]	0.0084015556	629.67370489
AYR [113]	0.0056851600	297.79369489

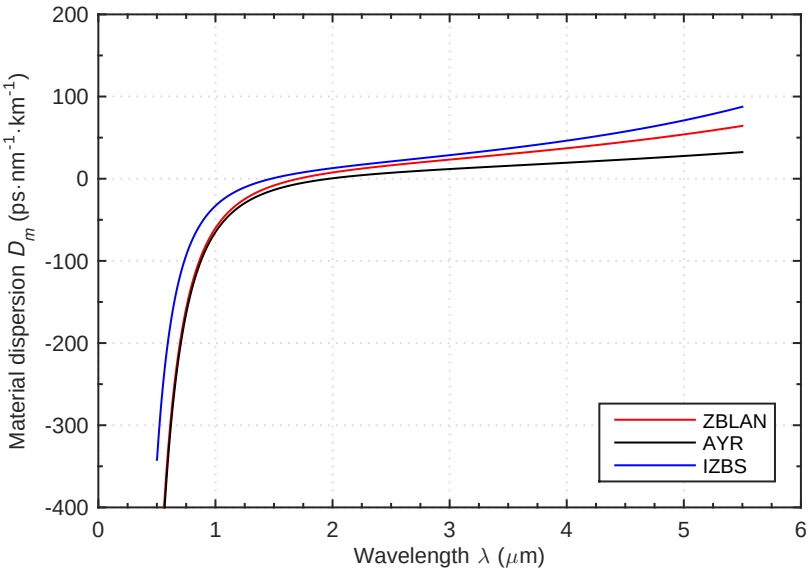

Figure A.6: Material dispersion upon wavelength for selected fluoride materials.

A.1.3 Tellurite and Chalcogenide Materials

The material properties such as linear and nonlinear refractive index of As_2S_3 chalcogenide glass used as the fiber background in Sec. 4.4 have been taken from Ref. 111. The glass is transparent from 0.57 to 11.8 μm.

Refractive indices of other chalcogenide glasses as As_2Se_3 transparent within 2 and 14 μm and As_2S_5 within 0.5 and 9.9 μm are given in the works Ref. [43] and [114], respectively. Tellurite glasses as 78 $TeO_2 - 5$ ZnO-12 Li_2O-5 Bi_2O_3 (TZLB), transparent from 0.4 to 6 μm and 60 $TeO_2 - 20$PbO-20 $PbCl_2$ (TLX) with the coefficients valid from 0.3 to 5 μm are specified in the works Ref. 115 and 116, respectively.

The refractive index wavelength dependence for tellurite and chalcogenide glasses is shown in Fig. A.7. The material dispersion wavelength dependence for the glasses is shown in Fig. A.8. The Sellmeier coefficients are summarized in Table A.4

Table A.4: Sellmeier coefficients of selected tellurite and chalcogenide materials.

Glass	B_1 (-)	B_2 (-)	B_3 (-)	B_4 (-)	B_5 (-)
As_2S_3 [111]	1.89838	1.92230	0.87651	0.11887	0.95699
As_2Se_3 [43]	4.99487	0.12072	1.71237	-	-
As_2S_5 [114]	2.13610	0.06930	1.76370	-	-
TLX [116]	1.21200	2.15700	0.18910	-	-
TZLB [115]	1.67189	1.34862	0.62180	-	-
Glass	C_1 (μm^2)	C_2 (μm^2)	C_3 (μm^2)	C_4 (μm^2)	C_5 (μm^2)
As_2S_3 [111]	0.022500	0.06250	0.12250	0.20250	750.00000
As_2Se_3 [43]	0.058390	361.00000	$2.1783 \cdot 10^{-7}$	-	-
As_2S_5 [114]	0.095400	225.00010	97.93428	-	-
TLX [116]	0.060680	0.0007068	45.19000	-	-
TZLB [115]	0.000467	0.0574608	46.72543	-	-

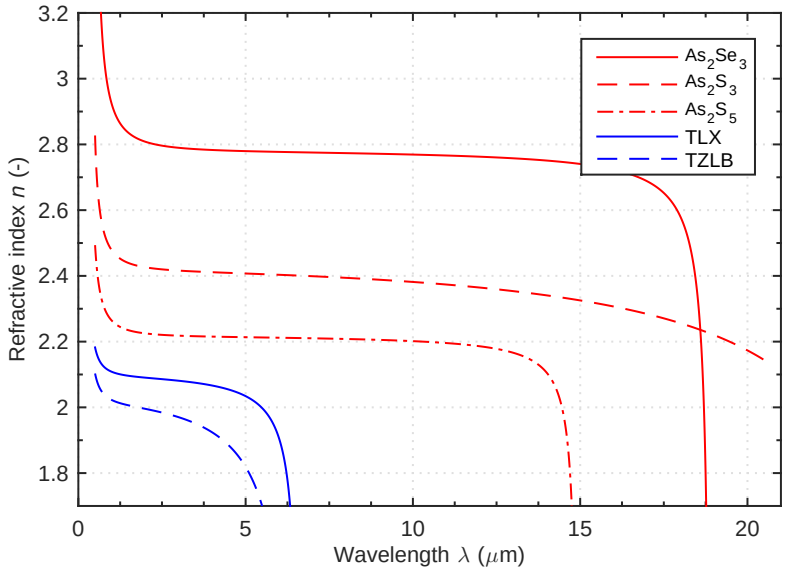

Figure A.7: Refractive index wavelength dependence of selected tellurite and chalcogenide materials.

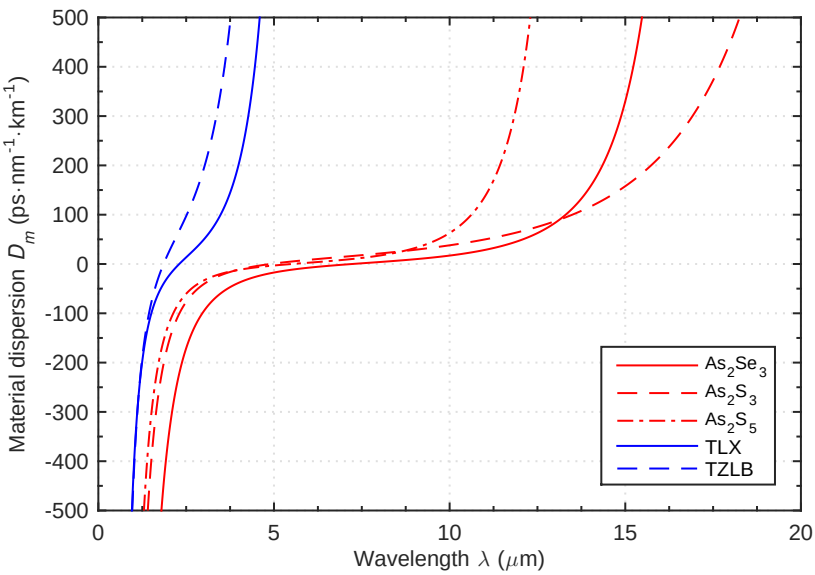

Figure A.8: Material dispersion upon wavelength for selected tellurite and chalcogenide materials.

Appendix B

Simulation Setup and Convergence testing

In the appendix, the most important convergence tests applied on the designed structures are shown. These include convergence test of size of the mesh cell (mesh size) dx and convergence test of number of perfectly match layers M_{PML}. It has been found that the influence of other simulation parameters is not so significant in terms of the accuracy on the calculated results. Since the inaccuracy is larger at the shorter wavelengths, most of the convergence tests are executed for the shortest wavelength of the investigated spectra. The fundamental modes are tested.

Effective refractive index is an investigated parameter for convergence tests. If the chromatic dispersion is the main studied parameter in a design (near zero dispersion and dispersion compensating fiber), the real part of n_{eff} is used for testing the mesh size and the imaginary part for testing the number of PMLs. For designs of optical filters and large mode area fibers, the imaginary part of n_{eff} is used for testing both the mesh size and the number of PLMs. Since the PMLs are used mainly to calculate confinement loss, the convergence test of the number of PMLs is not necessary if only the chromatic dispersion is an investigated parameter.

For clarity, number of the mesh cells M_x in x direction is used as the investigated parameter instead of size of the mesh cell dx. The number of the mesh cells differs in x and y direction, but the size of the cell is equal or nearly similar $dx \simeq dy$. PML distances from the edge of a PCF structure specify the dimensions of a simulation region. In this doctoral thesis, these distances are set to be same in x and y direction.

Convergence testing is described in Sec. (3.2).

B.1 Near Zero Dispersion Fiber - Convergence Test

The near zero dispersion fiber presented in Sec. 4.1 is simulated inside the computing domain of 15.3x13.71 μm with 28 PMLs. The region is divided by uniform mesh having size of the mesh cell $dx = dy = 0.034$ μm. This value is proportional to the number of the mesh cells in x direction $M_x = 450$. The distance between the edge of the investigated structure and the computational region is 1.325 μm for both, x and y direction. Convergence tests are plotted in Fig. B.1. In Fig. B.1(b), the convergence test has larger inaccuracy than other convergence tests presented in the appendix. It is therefore, the mode of the near zero fiber is well confined in the core and only few amount of the optical field extends outside to the PMLs resulting in the larger relative error.

However, the calculated loss difference between this (28 PMLs) and the next (32 PMLs) setting is negligible, less than $2.5 \cdot 10^{-16}$ dB·m at 1.7 μm. This wavelength is the longest within the investigated spectral range and the loss are maximal there. High accuracy is more important for calculating the chromatic dispersion especially if its value is desired to be close to zero. The result difference of this (450 mesh cells) and the next (500 mesh cells) simulation setup does not exceed the value of 0.018 ps·nm^{-1}·km^{-1} at the wavelength of 1.55 μm.

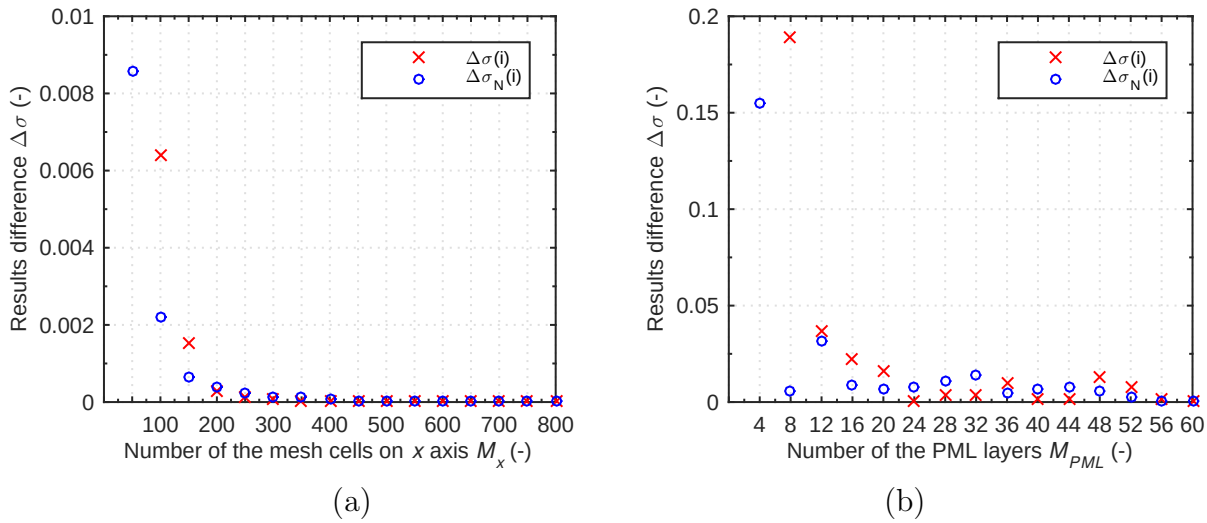

Figure B.1: Convergence testing the number of the mesh cells on x axis (a) and the number of the PML layers (b). The near zero dispersion fiber is considered.

B.2 Large Negative Dispersion Fiber - Convergence Test

The reasonably accurate results can be obtained for the large negative dispersion DC-PCF presented in Sec. 4.2 by the simulation model with the size of the computational region 20x17.3 μm bounded by 12 PMLs and having the uniform mesh size $dx = 0.05$ μm in x and y direction. The PML distance from the edge of the PCF structure is nearly similar in x and y direction and its value is $\simeq 1.35$ μm. The convergence test of the mesh size and convergence test of the number of the PLMs, are shown in Fig. B.2.

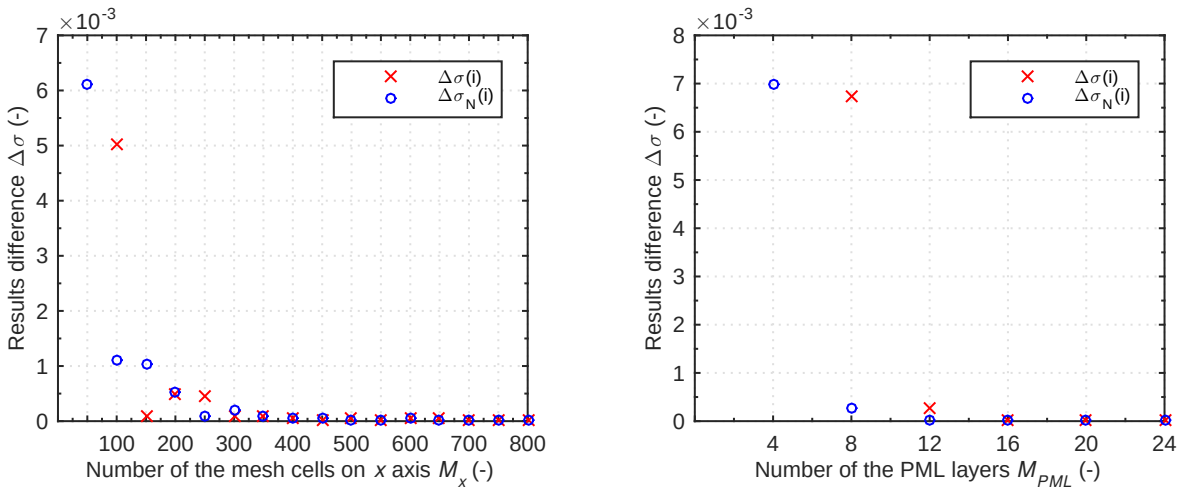

(a) (b)

Figure B.2: Convergence testing the number of the mesh cells on x axis (a) and the number of the PML layers (b). The large negative dispersion DC-PCF is considered.

An updated simulation model according to the DC-PCF structure modified in Sec. 4.2 has the size of the computation cell 16x13.84 μm in x and y direction, respectively, and the mesh size $dx = dy = 0.04$ μm. Number of PML layers M_{PML} is kept same. Convergence tests are shown in Fig. B.3.

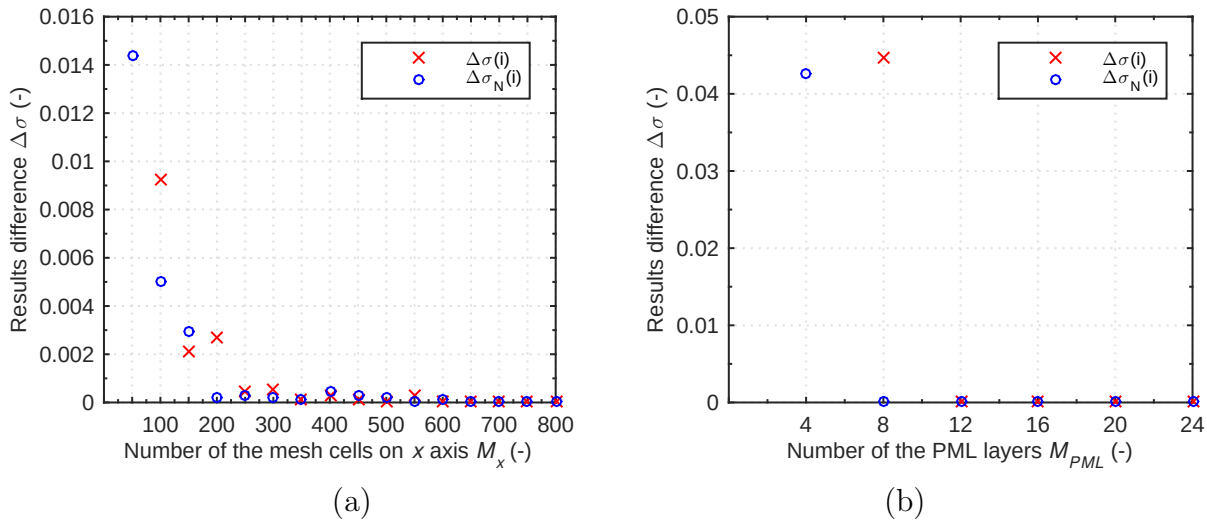

Figure B.3: Convergence testing the number of the mesh cells on x axis (a) and the number of the PML layers (b). The modified large negative dispersion DC-PCF is considered.

B.3 Narrowband Optical Fiber Filter - Convergence Test

For the narrowband optical fiber filter designed in Sec. 4.3 is the simulation region with the size of 21x18.664 μm dived by the uniform mesh with cell size $dx = dy = 0.035$ μm. The region boundaries consists of 20 PMLs. The result difference between this ($M_x = 600$) and the next mesh ($M_x = 650$) setup is less than 0.5 dB·m^{-1} at the wavelength of 1.55 μm, where the coupling of the modes occurs. The confinement loss of the designed fiber filter is at this wavelength about 18 dB·cm^{-1} that is much higher than the result difference. Moreover, the contribution of the PML setting to the overall inaccuracy is much lower than that of the mesh setting. Convergence testings are shown in Fig. B.4.

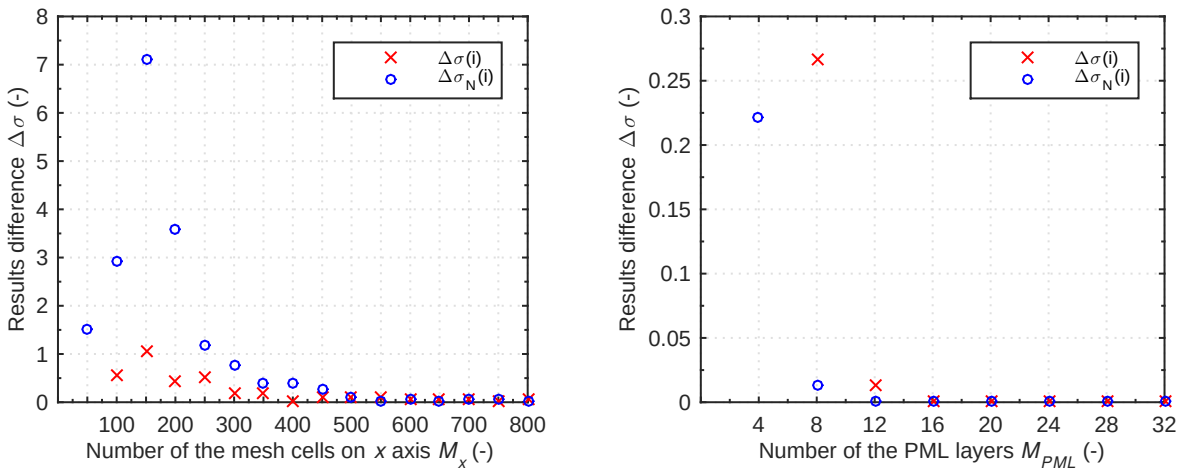

(a) (b)

Figure B.4: Convergence testing the number of the mesh cells on x axis (a) and the number of the PML layers (b). The narrowband optical fiber filter is considered.

B.4 Large Mode Area Fiber - Convergence Test

The structure of the large mode are fiber described in Sec. 4.4 is numerically investigated inside the computing region of size 240x208.923 μm in x and y direction, respectively. Number of the mesh cells over the region in x direction is $M_x = 800$ that is equivalent to $dx = dy = 0.3$ μm. The confinement loss calculated by this setting differs from the setting with $M_x = 850$ by about 0.015 dB·m^{-1}. Number of PMLs $M_{PML} = 16$ was verified by convergence testing shown in Fig. B.5(b). Comparing Fig. B.5(a) and B.5(b), the result difference for the PML setting is much lower than those of the mesh cell number. The number of the PMLs has a low impact on the overall accuracy.

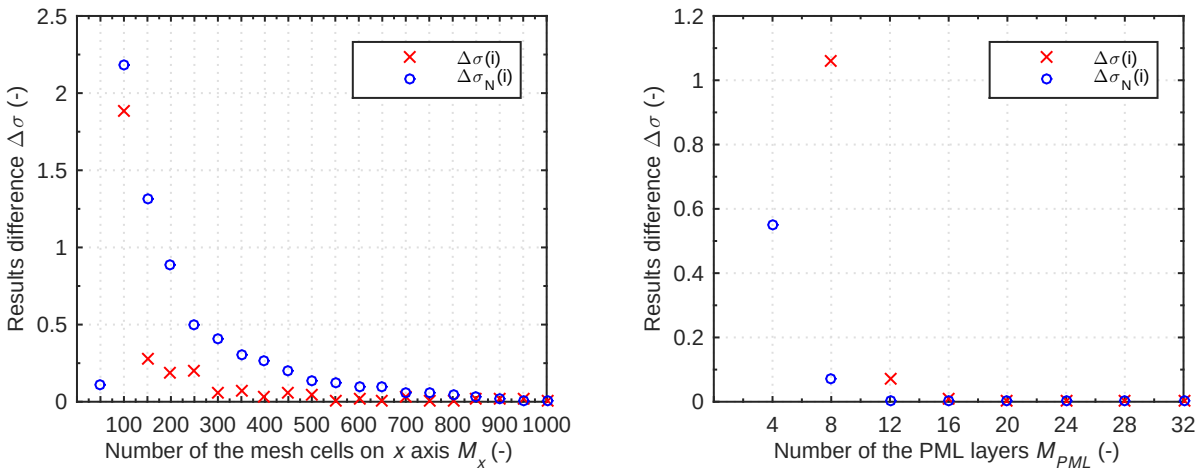

(a) (b)

Figure B.5: Convergence testing the number of the mesh cells on x axis (a) and the number of the PML layers (b). The large mode area fiber is considered.